HOKKAIDO UNIVERSITY

Title	Co-seismic and co-diking crustal deformation along subaerial rift zones detected by satellite synthetic aperture radar : East Africa, Iceland, and Southwestern Japan
Author(s)	姫松, 裕志
Degree Grantor	北海道大学
Degree Name	博士(理学)
Dissertation Number	甲第13574号
Issue Date	2019-03-25
DOI	https://doi.org/10.14943/doctoral.k13574
Doc URL	https://hdl.handle.net/2115/76432
Type	doctoral thesis
File Information	Yuji_Himematsu.pdf

Hokkaido University Collection of Scholarly and Academic Papers : HUSCAP

Co-seismic and co-diking crustal deformation along subaerial rift zones detected by satellite synthetic aperture radar: East Africa, Iceland, and Southwestern Japan

(衛星 SAR によるリフト帯における地震時・ダイク貫入時の地殻変動観測：
東アフリカ，アイスランド，西南日本)

Yuji Himematsu

Submitted for the degree of Doctor of Philosophy

Department of Natural History Sciences,

Graduate School of Science,

Hokkaido University

March 2019



Contents

要旨 **v**

Abstract **vii**

Acknowledgement **ix**

List of Figures **xi**

List of Table **xiv**

Chapter 1. Introduction **2**

1.1 Geodetic measurement for detecting Earth's surface movement ····· 2

1.2 Objective of this thesis ····· 6

1.3 Thesis roadmap ····· 8

Chapter 2. Monitoring crustal deformation using synthetic aperture radar images **14**

2.1 Synthetic Aperture Radar (SAR) ····· 14

2.2 Monitoring surface movement using SAR images ····· 18

2.2.1 Interferometric SAR (InSAR) ····· 18

2.2.2 Pixel tracking ····· 27

2.2.3 Time-series analysis ····· 30

Chapter 3. Aseismic strike-slip along graben subsidence associated with the 2007 Natron dike intrusion episode, Tanzania **34**

3.1 Introduction ····· 34

3.2 Methods and results ····· 37

3.3 Elastic source model ····· 42

3.4 Discussion ····· 46

Chapter 4. Along-rift horizontal displacement on graben subsidence during the 2005-2010 Afar dike intrusion episode detected by PALSAR-1 data 48

4.1 Introduction ····· 48

4.2 SAR data and processing method ····· 53

4.3 Fault source model ····· 56

4.4 Discussion ····· 60

4.4.1 Aseismic slip consistent with rate-and-state friction law ····· 60

4.4.2 Any relevance to strike-slip earthquakes along divergent plate boundaries? ····· 61

4.4.3 Block-like motion of graben floor as a response to horizontal flow of plume material? ····· 61

Chapter 5. Icecap and crustal deformation associated with the 2014-2015 Bárðarbunga dike intrusion episode inferred from SAR pixel tracking 66

5.1 Introduction ····· 66

5.2 SAR data and processing method ····· 70

5.2.1 Processing method and SAR dataset ····· 70

5.2.2 Observation result during pre- and co-diking period ····· 74

5.2.3 Estimation of subglacial ground deformation ····· 80

5.2.4 Temporal changes of icecap surface change ····· 83

5.3 Elastic modeling ····· 86

5.3.1 Model setting and geometry ····· 86

5.3.2 Distribution of dike opening and fault slip ····· 88

5.4 Discussion ····· 96

5.5 Post-emplacement deformation of Holuhraun lava field ····· 100

Chapter 6. Dynamic slip partitioning associated with the 2016 Kumamoto earthquake sequence, SW Japan 112

6.1 Introduction ····· 112

6.2 Methods and results ····· 114

6.3 Fault source model ····· 119

6.4 Discussion ····· 124

6.5 Post-seismic deformation revealed by PALSAR-2 data ····· 127

Chapter 7. Thesis findings and conclusions **132**

Bibliography **141**

Appendix A. SAR Dataset in Chapter 5 **153**

要旨

プレート境界ではひずみが集中しやすいため，地震活動や火山噴火が活発であり，プレート境界における地殻変動は地震や火山噴火の発生メカニズムを解明するために重要な研究対象である．なかでもプレート拡大境界はリフト帯と呼ばれ，新たな地殻の形成や大陸分断の過程を観測できる地域として注目を集めている．しかし中央海嶺に代表されるようにリフト帯の多くは海底に位置しており，陸上では全体の 2%以下しか観測できない．新たな地殻の形成や大陸分断の過程を観測できるリフト帯における地殻変動データの蓄積は，リフト帯における地球物理学的現象の解明にとって重要である．本論文では合成開口レーダ (Synthetic Aperture Radar: SAR) が観測した画像データに干渉 SAR (InSAR) と pixel tracking 法を適用することにより，リフト帯における地殻変動を観測した．全地球測位システム (Global Navigation Satellite System: GNSS) を用いた地殻変動観測とは異なり，衛星搭載型 SAR による画像撮像は観測機器を設置する必要はなく，一定間隔で陸域を全球的に撮像できる．また地殻変動のみならず氷河の流動や都市域の地盤沈下といったあらゆる地表変動を数 m の高い空間分解能で，面的に地表変動の描像を明らかにできる点も大きな特徴である．本論文ではリフト帯で発生した 4 件のイベントに対して適切な解析手法を適用し，これまで報告されていた観測データを質・量ともに凌駕する地殻変動データを用いて，観測結果を再現するモデルを提案し，それらの物理的解釈を提案する．本論文ではリフト帯で発生した 3 件のダイク貫入イベントと 1 件の地震イベントに注目した: 1) 2007 年 Natron 湖ダイク貫入イベント (タンザニア), 2) 2005-2010 年 Afar 盆地ダイク貫入イベント (エチオピア), 3) 2014-2015Bárðarbunga 火山ダイク貫入イベント (アイスランド), 4) 2016 年熊本地震 (西南日本).

東アフリカ地溝帯で発生した 2 件のダイク貫入イベント (2007 年 Natron 湖ダイク貫入イベント，2005-2010 年 Afar 盆地ダイク貫入イベント) では PALSAR-1 データに InSAR とピクセルオフセット法を適用することにより，ダイク貫入に伴う地殻変動の描像を明らかにした．これらの観測結果はグラーベンの沈降領域において拡大軸と平行する方位に水平変位が生じていたことを明らかにした．両イベント時におけるメカニズム解はいずれも横ずれ成分をほぼ含まない正断層型を示しており，これらの走向は拡大軸の方位とおおむね一致していた．このグラーベンの沈降領域における水平変位の再現には正断層ずれに加えて横ずれ成分も必要であることを数値計算によるモデルが示した．したがってグラーベンの沈降領域における水平変位は非地震的に生じたことが示唆された．地質構造の発達やマントル対流と地殻との相互作用によって生じた可能性が考えられる．

アイスランド中東部に位置する Bárðarbunga 火山で発生したダイク貫入イベントは 2014 年 8 月に始まり，ダイク貫入に伴って発生した割れ目噴火は 2015 年 2 月まで続いた．先行研究による InSAR 解析データは氷帽上で非干渉領域となっており，イベントに伴

う氷帽下地殻変動の描像を明らかにできていなかった．震源分布から推定された本イベントのダイクの貫入経路の約 80%は氷帽下に位置しており, 地殻変動データが十分に取得されたとは言い難い．また GNSS による観測も氷帽上では定常的な観測を行っていなかったため，ダイク貫入に伴う地殻変動の全容を把握することは困難であった．本論文では氷河の流動速度検出に採用される Pixel-tracking 法を COSMO-SkyMed と RADARSAT-2 データに適用することにより，ダイク貫入に伴う氷帽表面における変動の検出を試み，これらのデータを用いて氷帽下の地殻変動を推定した．Pixel tracking 法を適用した結果は非雪氷域のみならず，氷帽上においてダイク貫入のおよそ北半分の経路上で顕著な変動を示すシグナルを示した．また適切に重みをかけたイベント前のシグナルをイベント時のシグナルから差し引くことで氷帽下地殻変動の描像を推定した．補正したデータを使用して鉛直開口・断層運動を再現するモデルを推定したところ，非雪氷域のみの地殻変動データを用いてモデルを推定した場合と比較して疑似的な開口・すべり分布を示すことなく，より小さい不確定性をもったモデルを推定することができた．

2016 年熊本地震は南北の引張応力場にある九州地方の別府島原地溝帯で発生した．九州地方は中部九州の直下には地震波低速度領域が卓越しており continental rift であるとする説がある一方，別府島原地溝帯が南西から延びる沖縄トラフの東端と東から延びる中央構造線の西端に位置しており，南海トラフの前弧スリバーが南西進していることから pull apart basin であるという説もある．熊本地震に関して気象庁が示した本震のメカニズム解は南北方向に引張軸を持つ右横ずれ型地震であると同時に，顕著な非ダブルカップル成分も示した．国土地理院による InSAR 解析の速報は地表断層付近において非干渉領域となっており，地殻変動の描像を明らかにできていなかった．本章では PALSAR-2 データに pixel tracking 法を適用することにより，強健な地殻変動シグナルを検出して詳細な地殻変動の描像を明らかにした．それらのデータに基づいて断層モデルを提案して，非ダブルカップル成分との関連性を議論した．本震のメカニズム解は横ずれ成分が卓越していたものの，PALSAR-2 データによる pixel tracking の結果は右横ずれの水平変位に加えて 2m 以上の沈降を明らかにした．この地殻変動の複雑性はメカニズム解に含まれる非ダブルカップル成分に反映されている可能性が高く，観測された地殻変動の描像と推定した断層モデルのすべり分布は地震時における slip partitioning の形成を示唆している．また PALSAR-2 データによる干渉画像の重ね合わせにより明らかになった地震後地殻変動についても報告する．

Abstract

Crustal deformation along the plate boundaries is one of the important research interests for elucidating their mechanisms because earthquake activities and volcanic eruptions usually concentrate along plate boundaries due to high strain rates. Along the divergent plate boundaries which usually call rift zone, we can observe the processes of continental rifting evolution, such as generating new crust and splitting continental crust. Most of the divergent plate boundaries, however, are located beneath the sea, and the onshore rift zones are only less than 2 % of all the rift zones on the Earth.

The accumulation of crustal deformation data along the subaerial rift zones improves our understanding of the rift systems and the geophysical phenomena. The aim of this thesis is to reveal detailed crustal deformation along the subaerial rift zones by processing satellite SAR data, one of the space-based geodetic methods. SAR data can detect surface movement with high spatial resolution without installing on-site observation instruments, like GNSS receivers. This thesis focuses on three dike intrusion episodes and one earthquake event along the subaerial rift zones: 1) the 2007 Natron dike intrusion episode, Tanzania, 2) the 2005-2010 Afar dike intrusion episode, Ethiopia, 3) the 2014-2015 Bárðarbunga dike intrusion episode, Iceland, 4) the 2016 Kumamoto earthquake sequence, Japan.

By applying InSAR and pixel tracking approaches to PALSAR-1 data the horizontal displacements parallel to the rift axis on the graben subsidence were detected during the 2007 Natron and the 2005-2010 Afar dike intrusion episodes which occurred along the East African Rift. The focal mechanisms during each episode indicate normal faulting with few strike-slip components, these strikes nearly coincide with the rift axis direction. Our inversion model confirmed that the optimal elastic models need not only normal faulting but also strike-slip components to reproduce the horizontal displacement on the graben subsidence. Thus the along-rift horizontal displacements on the graben floor were implied to occur by aseismic processes.

The 2014-2015 Bardarbunga dike intrusion episode occurred along the subaerial divergent plate boundary between the Northern American and the Eurasian plates. The overall description of crustal deformation associated with the dike intrusion remains poorly revealed because 80% of dike path located beneath the Vatnajökull icecap which is the largest ice in Europe. Although the conventional InSAR method needs to avoid decorrelation problems for detecting signal above ices and/or glaciers, previous InSAR data could not reveal any signal at the icecap due to the decorrelation problems. In this thesis, we applied pixel tracking approach, which is suitable for detecting the velocity of glacier flow, to satellite SAR data to reveal icecap surface movement associated with the

subglacial dike intrusion. Because the co-diking signals contain the signal of both steady-state of icecap flow and crustal deformation, we corrected the icecap flow signal by subtracting the scaled pre-diking signal from the co-diking signal assuming that the pre-diking signals show only the steady-state of icecap flow signal. The ice-corrected signal implies the description of subglacial crustal deformation. We confirmed that the ice-corrected signal contributed to improve the dike opening/faulting model.

The 2016 Kumamoto earthquake sequence is the series of earthquake, including Mw 7.0 of mainshock, along the Beppu-Shimabara graben system in Kyushu, Japan. One of the characteristics of the event is that the sequence contains two foreshocks greater than Mw6.0 28 hours before the mainshock and four aftershocks greater than 5.5 one week after the mainshock. The focal mechanism of mainshock from the Japan Meteorological Agency shows not only the dominant of strike-slip components with N-S extensional axis but also ineligible non-double couple component. The newsletter from Geospatial Information Authority of Japan has reported that InSAR results indicate data lacking near the surface ruptures due to the decorrelation problems. In this thesis, we applied the cross-correlation-based pixel tracking approach to PALSAR-2 data to avoid the decorrelation problems. Although the focal mechanism of the mainshock dominates strike-slip component, our pixel tracking data indicates not only right-lateral displacement with NE-SW striking but also over 2 m of subsidence at the northern half of displacement field. The complexity of crustal deformation associated with the earthquake sequence can be explained by the non-double couple component in the focal mechanism of mainshock and the slip-partitioning.

Acknowledgement

This dissertation concludes five years of my graduate study at the Department of Natural History Sciences, Hokkaido University. I have received uncountable warm supports from many people and organizations for my graduate school life. First, I would like to show my hearty gratitude to my supervisor Professor Masato Furuya who encouraged and patiently advised me. He also gave me many opportunities to attend academic meetings and workshops for presentations of my research and discussions with many researchers. Professor Kosuke Heki and Professor Youichiro Takada provided inestimable possibilities of Geodesy through their interesting research. I'm always looking up to their positive attitudes with passions for exploring advance of geodetic approaches. I appreciate professors and researchers in the solid seminar for their constructive comments and discussions. Their comments always improve my knowledge and ambiguities in my presentations. Students in the seminar always encouraged me when I was struggling to advance my research. Also, I would like to express my gratitude to Professor Freysteinn Sigmundsson for accepting my proposal and approving my work in Iceland. He always warmly welcomed me to discuss and gave me interesting feedbacks for advancing our research. Discussion with researchers and students in the Institute of Earth Science, the University of Iceland, also contributed to promoting our research. The working in Iceland has been an irreplaceable experience in my life. I wish to thank the financial support from Japan Society for the Promotion of Science (JSPS) during my doctoral course. The Research Fellowship for Young Scientist maintained my living without part-time jobs, and the Overseas Challenge Program for Young Researchers supported my living in Iceland from November 2017 to March 2018. The Geodetic Society of Japan supported my travel grants for attending AGU meetings in US. Last but not least, I would like to thank all of the people who helped and supported me in the course of my graduate school life.

PALSAR-1 level 1.0 and PALSAR-2 level 1.1 data in this thesis are sharing among the PALSAR Interferometry Consortium to Study out Evolving Land surface (PIXEL), and provided by Japan Aerospace Exploration Agency (JAXA) under a cooperative research contract with the Earthquake Research Institute, University of Tokyo. The ownership of PALSAR-1 data belongs to both JAXA and the Ministry of Economy, Trade and Industry (METI). That of PALSAR-2 belongs to JAXA. COSMO-SkyMed, TerraSAR-X, RADARSAT-2 data in Chapter 5 are sharing among the FUTUREVOLC consortium (European Community's Seventh Framework Programme Grant No. 308377). COSMO-SkyMed and TerraSAR-X data in Chapter 5 are owned by the Italian Space Agency (ASI), the German Space Agency (DLR), both through the Icelandic Volcanoes Supersite project, supported by the Committee on Earth Observing Satellites (CEOS). RADARSAT-2 data were provided by the Canadian Space Agency and MDA Corporation. Sentinel-1A data in Chapter 5 is provided by the European Space Agency (ESA) at Copernicus Open Data Hub

(https://scihub.copernicus.eu/).

Focal mechanisms and hypocenters in Chapter 3, 4 are provided by the Global Centroid Moment Tensor Project database. These information of earthquake in Japan in Chapter 6 are provided by Japan Meteorological Agency (JMA). Some of figures are generated by commercial software MATLAB and the public domain Generic Mapping Tools (GMT).

List of Figures

Figure 1-1. World map with tectonic lines and seismicity, and enlarged maps of study areas in this thesis. ····· 5

Figure 2-1. An example of the range split-band spectrum method for PALSAR-2 dataset. ···· 21
Figure 2-2. Azimuth offset and MAI data which are derived from same PALSAR-2 dataset in Figure 2-1. ····· 22

Figure 3-1. Study area in Chapter 3. ····· 31
Figure 3-2. Subsampled PALSAR-1 InSAR data which show co-diking displacement associated with the 2007 Natron dike intrusion episode. ····· 33
Figure 3-3. Observation and calculation of azimuth offset for ascending orbit. ····· 34
Figure 3-4. Surface projection and 3D description of our optimal elastic model. ····· 35
Figure 3-5. Co-diking 3D displacement inferred from PALSAT-1 InSAR and pixel-tracking data. ····· 37
Figure 3-6. Inferred our optimal faulting and opening distributions. ····· 39
Figure 3-7. Coulomb stress changes due to dike opening for each receiver fault. ····· 40

Figure 4-1. Study area in Chapter 4. ····· 49
Figure 4-2. Temporal evolution of PALSAR -1 pixel-tracking data from 2007 to 2010 associated with the dike intrusion sequence in Afar. ····· 52
Figure 4-3. Cumulative PALSAR-1 pixel-tracking and MAI data from 21 May 2007 to 5 August 2010. ····· 54
Figure 4-4. Temporal evolution of cumulative azimuth offset and its cross-sections. ····· 56
Figure 4-5. Our optimal elastic model for the PALSAR-1 pixel-tracking data. ····· 58
Figure 4-6. Standard deviations of faulting and opening distributions. ····· 59
Figure 4-7. Coulomb stress changes due to dike opening in our model for each receiver fault. ····· 60
Figure 4-8. Cross section of topographic height and cumulative azimuth offset from 12 June 2007 to 5 August 2010 along the profile C-C' in Figure 4-2. ····· 62

Figure 5-1. Study area in Chapter 5. ····· 67
Figure 5-2. Pre- and co-diking Cosmo-SkyMed (CSK) pixel tracking results and ice-corrected signals. ····· 73

Figure 5-3. Pre-diking and co-diking 3D displacements inferred from CSK data. ····· 75
Figure 5-4. Stacked TerraSAR-X (TSX) pixel-tracking and co-diking 3D displacement inferred from CSK and TSX dataset. ····· 76
Figure 5-5. Enlarged 3D displacement inferred from CSK and TSX dataset and cross-section across and along the graben subsidence. ····· 78
Figure 5-6. RADARSAT-2 (RS2) pixel tracking results during pre- and co-rifting period and ice-corrected signal. ····· 81
Figure 5-7. Cross sections of descending Cosmo-SkyMed (CSK) range offset during the co-diking signal (grey dots) and ice-corrected signal (blue dots). ····· 82
Figure 5-8. Profiles of RADARSAT-2 (RS2) range and azimuth offset in Track 81 during the co-diking signal (grey dots) and ice-corrected signal (red dots). ····· 83
Figure 5-9. Time-series of vertical component of line-of-sight (LOS) change on the icecap from June 2014 to January 2017. ····· 85
Figure 5-10. Our optimal elastic model and the model geometry. ····· 91
Figure 5-11. Comparison of observations, calculations derived from our model, and residuals. 92
Figure 5-12. Dike opening and normal faulting distributions inferred from the observations which are masked above the icecap and its standard deviations. ····· 94
Figure 5-13. A PALSAR-2 interferogram across the Bárðarbunga caldera. ····· 98
Figure 5-14. CSK pixel-tracking data observed from ascending track across the Bárðarbunga caldera. ····· 99
Figure 5-15. CSK pixel-tracking data observed from descending track across the Bárðarbunga caldera. ····· 99
Figure 5-16. Lava field subsidence derived from stacked PALSAR-2 InSAR and pixel tracking. ····· 104
Figure 5-17. Range offset between 24 November 2014 and 2 February 2015. ····· 105

Figure 6-1. Study area in Chapter 6. ····· 109
Figure 6-2. PALSAR-2 pixel-tracking data which shows co-seismic displacement. ····· 112
Figure 6-3. Cumulative 3D displacement inferred from our pixel-tracking data of tracks 23 and 130. ····· 113
Figure 6-4. Comparison of cumulative 3D displacements inferred from three combination of PALSAR-2 pixel-tracking data. ····· 114
Figure 6-5. Schematic perspective of fault geometry of our inferred model viewing from NNE. ····· 116
Figure 6-6. Comparison with observation of pixel-tracking data, calculation derived from our slip distribution and their residual. ····· 118

Figure 6-7. Slip distributions on each fault segment viewing from WNW.·····119
Figure 6-8. Slip 1-sigma uncertainties for each segment calculated by 200-times iteration of inversion with random noise.·····120
Figure 6-9. Focal mechanisms of the mainshock derived from JMA catalog, and that derived from the inferred slip distribution. ·····123
Figure 6-10. PALSAR-2 footprints for detecting post-seismic crustal deformation. ·····127
Figure 6-11. Stacked PALSAR-2 InSAR following the mainshock. ·····129
Figure 6-12. Cumulative post-seismic quasi-displacements inferred from the stacked PALSAR-2 InSAR.·····130

List of Table

Table 3-1. ALOS-1/PALSAR-1 dataset in Chapter 3. ····· 32

Table 4-1. Timing and volume of intruded magma during the 2005-2010 Afar dike intrusion sequence. ····· 50
Table 4-2. PALSAR-1 dataset in this Chapter 4. ····· 51

Table 5-1. Satellite SAR dataset in Chapter 5 and scale factors for correction of icecap signal. ····· 72
Table 5-2. Dataset for inferring elastic model. ····· 95
Table 5-3. PALSAR-2 dataset for detecting the post-emplacement deformation. ····· 103

Table 6-1. PALSAR-2 dataset in Chapter 6. ····· 111
Table 6-2. Parameters of our fault model. ····· 117
Table 6-3. Total moment release derived from the inferred fault model (GM) and JMA catalog (SM). ····· 121
Table 6-4. PALSAR-2 dataset for the post-seismic deformation. ····· 125

Chapter 1

Introduction

Chapter 1. Introduction

1.1 Geodetic measurement for detecting Earth's surface movement

Geodesy is study for measuring Earth's shape, rotation, and orientation and these spatiotemporal variations. The study also has been contributing to observing crustal deformation associated with earthquakes, volcanic activities, and other geophysical phenomena. Since late 1900's, satellite geodetic techniques allow us to improve measurement accuracy and spatiotemporal resolution for monitoring surface movement on the Earth. Unlike leveling survey by taking much more time and with needing human's power for measuring, the satellite geodetic techniques can observe ground movement with high precision continuously or regularly. For example, long-term continuous observations for volcanoes contribute to understanding the mechanisms of volcanic eruptions because precursors, such as inflations of magma chamber due to charging magma, usually initiate from few hours to several years before the eruption.

Space-based geodetic techniques are utilized for detecting various scale of surface movement above the Earth such as plate motion, and crustal deformation associated with earthquakes. Detecting plate motions allow us to understand the process of dynamic plate tectonic and to sustain the geospatial reference. Although observations of geomagnetic reversal at seafloors and similarity of coastline between two continents can be one of the evidences of plate tectonics, one of the space-based geodetic techniques, very long baseline interferometry (VLBI), has detected variations of spatial baseline between two sites, suggesting one of the direct evidences for plate tectonics. Regarding crustal deformation, measuring ground displacement due to earthquakes and volcanic activities contributes to our understandings the mechanism of each physical process. In the case of modeling the observed ground deformation due to earthquakes, we usually employ an analytical solution of ground

deformation associated with rectangular dislocations in uniform elastic half-space proposed by Okada (1985, 1992). The solution has been mostly utilized for inferring a fault source model to compute distributions of slip (and tensile opening) by solving inversion problems (e.g., Jonsson et al., 2002; Wright et al., 2003). For crustal deformation due to volcanic activities, analytical solutions for approximating ground deformation have reported by using a point source (e.g., Mogi, 1958), an ellipsoidal source (e.g., Yang et al., 1988), a tensile dislocation (e.g., Okada, 1985) and a penny-shaped source (e.g., Fialko, 2001). We sometimes use multiple sources to fit the observation data because ground displacements due to volcanic activities cannot be explained by using a simple source completely (e.g., Fialko and Simons, 2000). These analytical solutions can also infer the volume of magma intrusion/extrusion, and the volume change due to inflation/deflation of magma chamber.

Various satellite geodetic techniques have contributed to accumulation of observation of Earth's surface movement, for example, Very Long Baseline Interferometry, Global Navigation Satellite System. Very Long Baseline Interferometry (VLBI) can observe relative plate motions between two observation sites (e.g., Christodoulidis et al., 1985). VLBI can position the location of observation sites with the accuracy of a few millimeters (Schuh and Behrend, 2012). VLBI can infer the distance between each telescope by measuring the arrival time difference of signals from the Quasi-Stellar object, an object emitting electromagnetic waves. VLBI has detected baseline shortening of 7-9 cm/yr between the Kashima station and Kawai station, suggesting that the Pacific plate is drifting to eastward (e.g., Heki et al., 1987). VLBI is not only for observing relative plate motion but also the fluctuation of Earth's rotation axis (precession, and nutation), and location of extragalactic objects in inertial space. VLBI can determine the Earth Orientation Parameters (EOPs) by observing the Earth's rotation axis movement.

Global Navigation Satellite System (GNSS) is the most famous geodetic observation system for positioning. One of the most famous GNSS satellite constellation, Global Positioning System (GPS) operating by US army, is consists of 24 satellites orbiting above 20,000 km from the Earth and receivers. Nowadays, some countries launched GNSS satellites to improve the measurement accuracy for their regions, such as Beidou in China, Galileo in EU, and QZSS in Japan. Improving measurement accuracy by increasing GNSS satellites is expected to realize developments of automatic transportation system, such as an automatic car driving. In Japan, Geospatial Information Authority of Japan (GSI) installs and maintains a dense GNSS network across Japan with 1300 observation sites, called GNSS Earth Observation Network system (GEONET). GEONET, for example, contributed to revealing wide-region of co-seismic crustal deformation moving toward trench due to the 2011 Tohoku-oki earthquake (e.g., Nishimura et al., 2011). GNSS observation data sometimes involves artifacts induced by delay of microwave arrival time and ionospheric disturbance, however ionospheric artifacts can be corrected because GNSS measurement employs dual frequency of L-band microwave. The correction of ionospheric artifacts can describe the distribution of total electron content (TEC). Calais and Minster (1995) have reported that the first detection of travelling ionospheric disturbance (TID) due to propagating acoustic wave excited by surface uplifts due to the 1997 Northridge earthquake, California. A GNSS measurement have detected positive TEC anomaly less than 1 hour before the mega earthquakes (e.g., Heki, 2011). Although a temporal resolution of ionosonde observation is 15 minutes, the ionosonde observation and a geomagnetic declination also simultaneously varied as well as the GNSS observation (e.g., Heki and Enomot, 2013).

VLBI and GNSS networks utilized to not only measure not only crustal deformation and relative plate motion but also maintain the International Terrestrial Reference Frame (ITRF) for precise positioning. ITRF has been renewing regularly with using the accumulated past dataset, at present,

ITRF 2014 is the newest (Altamimi et al., 2016). The dataset of Satellite Laser Ranging (SLR) and Doppler Orbitography and Radio-positioning Integrated by Satellite (DORIS) are also employed for the maintenance of ITRF.

For measuring crustal deformation using VLBI or GNSS technique (or other geodetic methods, such as leveling survey), we need to install the instruments at the observation sites before the events. Installing measurement instrument also requires much costs. If you would like to observe crustal deformation automatically for a whole, you need to prepare power generators, like solar photovoltaic generations, for observations, and must perform instrument maintenance and pick up data which is recording on loggers regularly. Measuring crustal deformation associated with volcanic activities take risks of involving dangerous, such as sudden eruptions during installing. As mentioned above, observing crustal deformations on the field generally must prepare money, time, and human-power for collecting data. In contrast, synthetic aperture radar (SAR) can observe crustal deformations without installing observation instruments at study area where you would like to observe. Although optical images cannot identify surface condition during nights and cloudy, SAR images can always reveal surface characteristics as back-scatter intensity because SAR sensors employ microwave. Although you usually need to pay money or submit your proposal of research for obtaining SAR data, you can get SAR data observed by Sentinel-1, which is operating European Space Agency (ESA) from 2014, for free via ESA website after you registered, at writing this thesis. SAR sensors onboarding satellites can acquire data regularly because satellites orbit around Earth at an interval of the designated period. COSMO-SkyMed, which is operated by Italian Space Agency and is a constellation of SAR satellite, performs one day of temporal resolution at shortest, even a sole satellite acquires data at an interval of 12 days, in case of Sentinel-1 satellite. Data accumulation enables us to reveal long-term small displacements as well as GNSS measurements, although GNSS measurement performs higher

temporal resolution. Of course, it is not necessary to install any instruments for observations, such as GNSS receivers. Spatial resolutions of SAR observation perform a few meters at a minimum, although it depends on image acquisition modes and scale factors of spatial filters for mitigating noises. Therefore, employing SAR data for observations can avoid various issues such as financial, human resources, and risks for dangerous. Introduction of SAR principle and analysis methods are described in Chapter 2.

1.2 Objective of this thesis

This thesis focuses on crustal deformations associated with dike intrusions and earthquake episodes along subaerial rift zone. Generally, most of rift zone are under an extensional stress regime, which are usually driven by upwelling mantle plume, negative buoyancy, and tectonic stress. Due to upwelling materials of upper mantle, we can observe processes of splitting continental crust and new crust formation along continental rifts, like the East African rift and Iceland. Subducting slab induces negative buoyancy of crust, and contributes to forming back-arc basin, like Ryukyu, and Mariana trough. Pull apart basin can be formed at a junction of rift and lateral fault termination, like Kyushu island in SW Japan and the Dead Sea basin. As mentioned above, formations of rift zone are induced by various geophysical factors. However, most of the rift zone is located at seafloor, we can observe only 2% of all rift zone on land. Subaerial rift zones thus are important research interest for elucidating processes of splitting crust or rift evolutions.

Even if convergence plate boundaries are located far from the metropolitan area, mega-earthquakes usually generate strong shaking and sometimes tsunami if subduction zones are beneath the sea. Strong shaking generated by an earthquake occurred at a deeper brittle part propagates toward wide range, and usually destroys buildings and induces secondary disasters. Tsunami is also destructive water wave induced by mega-earthquakes, and usually wipe out physical objects on land. That is why various

observations are installing at offshore along subduction zones, such as trench around Japan, Cascade in US, and Chile. In contrast, scales of earthquakes along rift zones are moderate, unlike subduction zones which occur greater than magnitude 8 of earthquakes. Because the thickness of brittle part is relatively small, large scale earthquakes cannot physically occur along rift zones as mega-earthquake along convergence plate boundaries. Also range of destruction is relatively limited because earthquakes along rift zones are shallower part of crust. Although a priority of research interest thus may not be so high in terms of disaster prevention and human society, the accumulation of observation data is expected to contribute to the improvement of our understanding of plate tectonics, and dynamics of the crust and mantle. Using satellite SAR data, we can observe crustal deformation along subaerial rift zones without accessing there even if the rift zones are locating far from where we are working at.

Although moderate-scaled earthquakes occurred along rift zones, the scale of crustal deformation is sometimes beyond one meter for the scale of earthquake. In case of that, the earthquake may have a relationship with magma within the crust. Storing in a magma source or ejected magma from a chamber are transported from the source along weak lineaments. Because the weak lineaments are formed directing to the rift axis, the strike of lateral magma propagation would also consistent with the rift axis. We usually say the propagated magma as a dike, and an episode sequence related to dike intrusions would be a dike intrusion episode. Dike intrusions are supposed to be a preliminary stage of rift evolution, and induce meter-scale crustal deformation which can be described formations of graben structure.

One of the objectives of this dissertation is to find appropriate SAR analysis methods for revealing crustal deformations with few data lacking due to dike intrusion an earthquake episodes

along rift zones. Generally, identifying crustal deformation with large displacement gradient in interferograms, such as displacement near surface ruptures, is one of the challenging topics because dense fringes sometimes cause phase unwrapping error, although InSAR can detect surface movements with high measurement accuracy. Crustal deformations with large displacement gradients which usually appear near fault are expected to involve important information of deformation source, indicating that there would be key point for the implication on our understanding of the mechanism. Xu et al. (2016) investigated a synthetic inversion test how the lacking data of input data near deformation source contributes to retrieve the original deformation map. The synthetic test result also confirmed that the re-inferred slip distribution indicates both slip deficits at the shallowest part of fault segment and artificial overestimated slip at the slightly deeper part of segment when the input data were masked wider region of data across the center of deformation field. Therefore reducing missing data is expected to contribute not only providing information of displacement fields but also inferring elastic models precisely.

1.3 Thesis roadmap

This thesis consists of four main topics. Study area are shown in Figure 1-1. All topics are focusing on crustal deformations due to dike intrusions and earthquakes along rifts observed by satellite SAR data.

The thesis roadmap is as follow:

Chapter 2 introduces the principal of SAR observation and SAR processing approaches to monitor surface movement across SAR images.

Chapter 3 focuses on the crustal deformation associated with the 2007 Natron dike intrusion episode in Tanzania. A 3D displacement inferred from PALSAR-1 InSAR and pixel-tracking data showed non-negligible southward displacement at the graben subsidence, although the direction of the

rift axis around Lake Natron is NNE-SSW. Our optimal elastic model required the strike-slip components to reproduce the along-rift displacements at the graben subsidence. Because focal mechanisms during the episode indicated few strike-slip components, the strike-slips along the graben-bounding faults occurred aseismically.

Chapter4 focuses on the crustal deformation associated with the 2005-2010 dike intrusion sequence in Afar, Ethiopia. PALSAR-1 pixel-tracking data derived from only ascending track during 2007-2010 detected signal of horizontal displacement at the northern half of graben subsidence. The

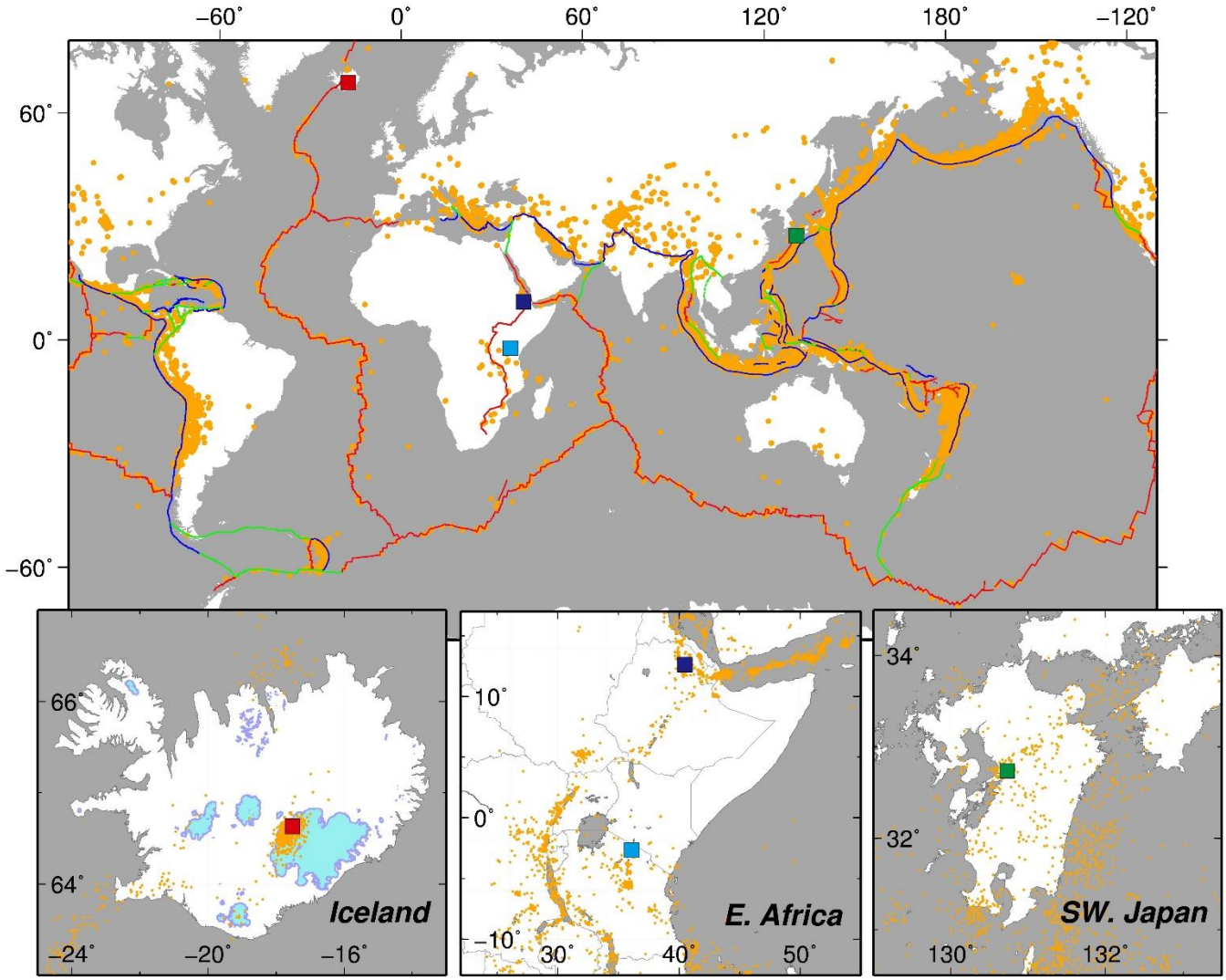


Figure 1-1. World map with tectonic lines and seismicity, and enlarged maps of study areas in this thesis. Red, blue and green lines indicate divergent, convergent, and transform plate boundaries from Peter (2003) and Coffin et al., (1998). Orange bots are the seismicity of M>3 during January-August 2018. Red, dark blue, light blue and green rectangles are the location of Bárðarbunga volcano, Afar basin and Lake Natron, and Kumamoto city, respectively.

horizontal displacement signal implied to reveal the along-rift horizontal displacement at the graben subsidence as well as the 2007 Natron dike intrusion episode. Our optimal elastic model in this case also need strike-slip components to reproduce the signal of horizontal displacement at the graben subsidence.

Chapter 5 focuses on the crustal deformation associated with the 2014 dike intrusion episode

at the Bárðarbunga volcanic system, Iceland. Most of the dike propagation path are located beneath the icecap. Although previous InSAR data have revealed crustal deformation at only the ice-free region, our Cosmo-SkyMed and RADARSAT-2 pixel-tracking data detected a line-shaped subsidence signal above the icecap, implying subglacial graben formation due to the subglacial dike intrusion. Using these pixel-tracking data, the subglacial crustal deformation was inferred by subtracting the scaled pre-diking signal from the pre-diking signal assuming that the pre-diking signals contain only the signal of the steady-state of icecap flow. This chapter also describes an experiment whether the inferred subglacial crustal deformation contribute to improve the dike opening/faulting elastic model.

Chapter 6 focuses on the crustal deformation associated with the 2016 Kumamoto earthquake sequence in Japan. The episode contains two foreshocks and a following mainshock (Mw 7.0) 28 hours after the first foreshock. The epicentral region locates along the Beppu-Shimabara graben system, which is an extension stress regime across the central Kyushu island. Japan Meteorological Agency (JMA) reported that focal mechanisms during the episode dominates strike-slip components with ENE-WSW striking, however PALSAR-2 pixel-tracking data revealed significant subsidence of 2 m. This chapter proposes the fault source model inferred from the geodetic data, and discusses the relationship between the non-double couple components in the focal mechanisms of the mainshock and significant subsidence.

Chapter 7 provides the findings from my works and conclusion of this thesis.

Chapter 2

Monitoring Crustal Deformation Using Synthetic Aperture Radar Image

Chapter 2. Monitoring crustal deformation using synthetic aperture radar images

2.1 Synthetic Aperture Radar (SAR)

Synthetic Aperture Radar (SAR) is one of the active sensors to observe information of back-scatter intensity and phase of the emitted microwave from scatterer on the ground. SAR sensors are usually equipped on airplane or satellites, we do not have to install observation implements for acquiring data, like GNSS measurement. SAR data is described by the complex number, that is, a pixel contains the real and imaginary part. Real part shows the distribution of backscatter intensity, indicating detail of ground characteristics. White color indicates strong back-scatter intensity, such as, the rough ground condition such as architectures, while black color indicates low back-scatter intensity, such as, the smooth ground condition such as airport runways and water surface. For example, change of back-scatter intensity between a SAR image acquisition interval contributes to detecting the flooded region due to heavy rain/storm and tsunami. SAR images usually contain some geometric image modulations due to illuminating microwave with some incident angles, that is, shadowing, layover and foreshortening. Because of the geometric modulation, mountains in SAR images looks skewing toward a near-range direction. On the other hand, an imaginary part of SAR data indicates phase data of microwave. Although these look like random noise, the phase data is utilized to detect surface movements across the image (see Chapter 2.3.1). Another information of microwave, polarization directions, also contributes to identifying characteristics of the ground condition. An RGB composition image can also be characterized artificial buildings, cultivations, and forests by coloring to each polarization images.

Japan Aerospace Exploration Agency (JAXA) have launched three SAR satellites at the

present of writing this thesis, and these satellites have contributed to observed not only crustal deformation but also damage overview due to devastating disasters in Japan. First Japanese SAR satellite, Japanese Earth Resources Satellite-1 (JERS-1, Japanese nickname of Fuyo-1), was operating from 1992 to 1998, and contributed to observe the crustal deformation due to the 1995 Kobe earthquake in Japan (e.g., Ozawa et al., 1997). Second Japanese SAR satellite, Phased Array type L-band Synthetic Aperture Radar (PALSAR, Japanese nickname of Daichi), was operating from 2004 to 2011, and contributed to observe the crustal deformation associated with the 2008 Sichuan earthquake in China and the 2008 Iwate-Miyagi inland earthquake in Japan (Kobayashi et al., 2009; Takada et al., 2009). At the time of writing this thesis, the latest Japanese SAR satellite, PALSAR-2, is under operation from 2014. These Japanese SAR satellites employ L-band microwave (1.25 GHz, wavelength of 23.6 cm) to acquire the images. Another Japanese small X-band SAR satellite, Advanced Satellite with New system Architecture for Observation 2 (ASNARO-2), is also launched and operating by NEC corporation collaborating with the Ministry of Education, Culture, Sports, Science and Technology (MEXT).

SAR data is employed to monitor not only ground characteristics but also glaciers where it is hard to access, deforestation in the tropical rainforest, unidentified ship floating on the sea and so on. For example, JICA-JAXA Forest Early Warning System in the Tropics (JJ-FAST) monitors tropic rainforest using ALOS-2/PALSAR-2, which is one of the satellite SAR sensors operating Japan Aerospace Experience Agency (JAXA). The system provides the information of on-going illegal deforestation to the governments in the 77 countries in the tropics using SAR data (http://www.eorc.jaxa.jp/jjfast/).

SAR sensors that are used usually employ three-types of microwave frequency to acquire

images: X-band, C-band, and L-band. Shorter wavelength microwave, X-band, is adopted by COSMO-SkyMed and TerraSAR-X satellite which are operating by Italian Space Agency (ASI) German Aerospace Center (DLR), respectively. The DLR SAR satellite COSMO-SkyMed consists of a satellite constellation with four satellites. The first commercial SAR satellite TerraSAR-X produced high-spatial resolution of digital elevation model (DEM) across the world observing with Tandem-X satellite data. European SAR satellites operated by European Space Agency, such as ERS-1/2, ENVISAT/ASAR and Sentinel-1A/B, have utilized C-band microwave for image acquisitions. Japanese SAR satellites, such as PALSAR-1/2 sensors, employ L-band microwave as mentioned above. Differences of radar wavelength vary sensitivities of back-scatter intensity from the ground. Shorter wavelength microwaves reflect at leaves on trees, while longer wavelength microwaves reach the ground even dense leave and branch of trees are planted. The difference of radar wavelength causes variation of characteristics of backscatter intensity at vegetation and non-vegetation regions. Therefore the decorrelation problems are induced by the variation of vegetation on the ground when we measure ground movements using the interferometric SAR approach as mentioned below. Rignot et al. (2001) also reported that difference of radar wavelength varies the penetration depth into ices and/or glaciers. Variation of microwave penetration depth can reveal physical properties of ices, such as characterizing wet or dry ice.

One of the superior points of observation is that SAR sensors can acquire images with few lacking data under even the condition of the night or cloudy. Because passive sensors, like optical satellites, requires sunlight to acquire images, we cannot find ground features using the images during the time when it is covered with cloud. It is also not suitable for image acquisition in the winter polar region due to the polar night. On the other hands, the SAR sensor both radiates microwave toward the ground and receives it which reflected from the scatterer repeatedly. SAR images can reveal not only

the ground surface but also caldera surface even if volcanic gases with dust and tephra are been pluming. SAR data therefore can be acquired without being influenced by the weather or day/night.

SAR data looks monochrome images with high spatial resolution. For example, a data acquisition mode with super high spatial resolution can identify even aircraft model on airport runway. To realize the high spatial resolution of SAR images, various techniques can be applied. Pulse compression is one of the image processing techniques to improve the spatial resolution for range direction R_r. R_r strongly depends on the bandwidth B_w. Shortening pulse width is one of the strategies for improving R_r, however the shortening pulse width needs much electricity in order not to degrade signal-to-noise ratio. Productivity of electricity on satellites and airplanes is limited. Instead of the shortening pulse width, we usually employ the pulse compression technique to improve R_r. Modulating microwave frequency realizes to gain the short pulse width with maintaining signal-to-noise ratio through the matched filter. The improved spatial resolution can be described as follow:

$$R_r = \frac{c}{2B_w \sin\varphi} \tag{2.1}$$

c represents the light speed in vacuum, φ the incidence angle of illuminating microwave.

For the azimuth direction, synthetic aperture technique enables us to improve the spatial resolution for azimuth direction R_a comparing with real aperture radar images. In order to identify two-point scatterers located along azimuth direction, a distance between two scatterer must be longer than beam width, which the beam pattern can be described by using the sinc function. The beam width defined by the 3 dB width $W_{3\,dB}$ can be expressed as

$$W_{3\,dB} = \frac{\lambda R}{D} \tag{2.2}$$

where λ is wavelength microwave, R is distance for slant range direction. D is length of antenna. If

we apply the parameters of ALOS-2/PALSAR-2 to the equation, the spatial resolution for azimuth direction would be ~15 km (λ = 0.236 m, R = 628 km, D = 10 m). Of course, the spatial resolution is not suitable for observing details of surface characteristics. In order to improve the spatial resolution of images, we must consider the doppler shift of phase. Because the consideration assumes to synthesize long antenna along the azimuth direction, the improved spatial resolution can be re-described as a half of antenna length L.

$$R_a = \frac{L}{2} \tag{2.3}$$

Theoretically, the shorter the antenna length is, the finer the spatial resolution is. The shorter antenna length, however, causes low signal-to-noise ratio because of small microwave gain.

SAR sensors are utilized not only for observing the earth surface but also for exploration of Venus covered with thick carbon dioxide clouds. A SAR sensor which was equipped on the Magellan observed the Venus surface by taking advantage of the property passing through the clouds. We can usually use SAR images observed from satellites and aircrafts, however SAR images are also acquired on ground instruments (Ground-based SAR; GB-SAR) (e.g., Tarchi et al., 1999). The GB-SAR makes it possible to measure with not only high spatial resolutions but also high temporal resolutions for a specific observation target, such as volcanoes and landslides (e.g., Antonello et al., 2004; Intrieri et al., 2013).

2.2 Monitoring surface movement using SAR images

2.2.1 Interferometric SAR (InSAR)

Nowadays, SAR is one of the strong tools to detect surface movement associated with not only earthquakes or volcanic activities but also glacier flow or landslide. Most famous SAR processing method for detecting surface movement is interferometric SAR (InSAR). InSAR can detect surface

movement with the accuracy of a few centimeters using the phase data within SAR images. InSAR data is sensitive to the displacement projected to line-of-sight (LOS) direction, which is the direction between satellite and ground. LOS lengthening indicates subsidence or horizontal movement away from satellite, while LOS shortening indicates uplift or horizontal movement toward satellite.

Actually, an initial interferogram involves not only information of surface movement but also that of topographic height, observation geometries and other noises. To identify surface movement, we must correct fringes which is derived from topographic height and orbital baseline, and we had better reduce noises due to atmospheric delay, ionospheric disturbance and systematic noise and so on. Topographic fringes were subtracted by simulated fringes which is estimated by using digital elevation model (DEM), for example, 3-arcsec Shuttle Radar Topography Mission (SRTM) data (Farr et al., 2007). Conversely, we can generate DEM maps using SAR data in short temporal baselines with assuming of no surface deformation between the image acquisition interval. Orbital fringes derived from satellite observation geometries can be removed by precise orbital information provided by each space agency. The larger the baseline between first and second observation positions, the denser the orbital fringes are. Theoretically we cannot correct dense orbital fringes whose wavelength is beyond the spatial resolution per a pixel, called as critical baseline.

Initial phase difference is wrapped between $-\pi$ to $+\pi$, which means that the value is shown as modulo 2π. Thus we must unwrap the wrapped phase in two dimension to identify cumulative phase difference from a reference point using some algorithms, for example, the minimum cost flow or the brunch-cut algorithm (Phase unwrapping). It is, however, hard to connect spatial fringes where large movement occur. If the wavelength of displacement fringes is larger than pixel spacing of SAR images, we cannot identify the absolute phase difference.

Fringes in interferograms show surface movements along a line-of-sight direction. The interval of interferogram fringes coincides with a half of the radar wavelength for image acquisitions, indicating that one cycle of fringe generated by L-band microwave indicates 11.8 cm of surface movement along a line-of sight direction. Even if we would like to measure ground deformations due to a same event, fringes in interferograms become dense if we employ SAR data acquired by shorter wavelength microwave. Therefore interferograms generated by shorter wavelength microwave is hard to identify surface movements with high displacement gradients. Dense fringes sometimes cause phase unwrapping error if gradients of surface movements per a pixel are beyond one cycle of radar wavelength. The limit of detectable displacement gradient can be described as

$$d = \frac{\lambda}{2D} \tag{2.4}$$

where *d* is the limit of detectable displacement gradient, λ is the radar wavelength, and *D* is the spatial resolution of SAR images (Massonnet & Feigl, 1998).

One of the issues in InSAR data is the artificial phase anomaly because of fluctuation of total electron content (TEC) in the ionosphere and water vapor content in the troposphere. These factors of artificial phase error are derived from the variation of refractive index in the medium. The variation of refractive index changes the propagation speed of the microwave, although the propagation speed of electromagnetic wave passing through the vacuum is consistent with the speed of light. Theoretical propagation speed of microwave is described as

$$v = \frac{c}{n} \tag{2.5}$$

where c is the speed of light in vacuum (299,792,458 [m/s]), n the refractive index, and v the speed of microwave. Because the phase artificial lead to misinterpreting the actual signal in the

InSAR data, it is had better to correct the anomalies.

Strong artifacts due to a variation of electron content in the ionosphere, where the range is 50-200 km altitude, usually contaminate InSAR data. Because traveling ionospheric disturbance (TID) is driven by gravity wave, the ionospheric artifacts appear wider region across InSAR data, for example azimuth streak (Meyer et al., 2006). The effect of electron fluctuation in the ionosphere depends on the microwave frequency because the ionosphere is dispersive medium. On the other hands, the effect of surface movement, topography and tropospheric noise are appeared in non-dispersive phase difference in InSAR data.

First order-term of ionospheric delay Δr_{iono} can be described as

$$\Delta \boldsymbol{r_{iono}} = \frac{\boldsymbol{K}}{\boldsymbol{f_0^2}} \Delta \boldsymbol{TEC} \qquad (\mathbf{2.6})$$

where K = 40.31 [m^3/s^2] is a constant, f_0 is the carrier center frequency of SAR data acquisition, ΔTEC is relative TEC along the line-of-sight between two SAR images. L-band images (wavelength: 23.6 cm) therefore is 16-times sensitive to C-band images (wavelength: 5.6 cm). In other words, L-band images is superior to observe ionospheric phenomena (Maeda et al., 2016). InSAR measurements can provide us dynamics of ionospheric phenomena with high-spatial resolution. For example, Maeda et al. (2016) reported first imaging of small-scale horizontal structure of midlatitude sporadic E (Es) patches using ALOS/PALSAR images. Although GNSS total electron content (TEC) measurement revealed only frontal structure of Es patches (Maeda & Heki, 2014), InSAR phase difference showed small-scale disc-shaped patches within the frontal structure.

One of the most robust approach for correcting ionospheric artifacts in interferograms is a range split-spectrum method (Brcic et al., 2010; Furuya et al., 2017; Gomba et al., 2016; Rosen et al.,

2010), although several approaches are proposed so far. The original idea is the same as GNSS-TEC observation, which is that GNSS observations can be corrected by using two carrier microwave frequency (e.g., Tsugawa et al., 2004). Like GNSS-TEC observation, the split-spectrum method can distinguish between dispersive and non-dispersive component by using low- and high-frequency SAR images. Especially the method is suitable for correcting ionospheric noise in InSAR data observed by recent SAR sensors (e.g., PALSAR-2) because these sensors employ wide bandwidths for improving image spatial resolution for range direction. An example of the method is described in Gomba et al, (2016) The measurement accuracy of sub-band interferograms becomes worse than that of original interferograms due to loss of a part of bandwidth. To reduce the effect of ionospheric artifacts correctly, short perpendicular baselines between two SAR images are required.

Figure 2-1 shows an example of the application of range split spectrum method for PALSAR-2 data covering the mid-west Kyushu island, Japan. Although the data was expected to contain the post-seismic deformation signal associated with the 2016 Kumamoto earthquake sequence, patches and/or streaks of phase difference are appeared in the interferogram. The co-seismic deformation due to the episode and its understandings are reported in Chapter 6. To understand the InSAR data in detail, the range split spectrum method was applied to the PALSAR-2 data. Applying the range split spectrum method to the sub-band images, the dispersive and non-dispersive components can be distinguished shown in Figures 2-1c and 2-1d. The dispersive component shows wedge-shaped phase streaks across the data (Figure 2-1d). The azimuth offset and MAI data also reveal strong streaks which was induced by the ionospheric disturbance (Figure 2-2). Therefore the wedge-shaped phase anomaly in the dispersive component are induced by the disturbance of TEC in the ionosphere. On the other hands, the non-dispersive component reveals ~1 phase cycle (~10 cm) of positive E-W aligned phase anomaly patches (Figure 2-1c), although a few phase fluctuations are appeared at the area far

from the epicentral region. The phase anomaly patches can suggest the surface movement as the post-seismic deformation (ex. localized subsidence at urban area due to liquefactions), however an interferogram which is derived from the images on 10 May 2016 and 19 July 2016 shows a few centimeters of positive LOS changes near the epicentral area. At the time of data acquisition on 21 June 2016 (15:18 UTM), high rainfall intensity was observed across the central Kyushu island according to the map of rainfall distribution on 15:10 and 15:20 21 June 2016 (UTM) (Figures 2-1e and 2-1f). The intensity of radar echo for identifying the precipitation per hour indicates E-W aligned patches of strong rainfall, whose locations are slightly westward for the locations of phase anomaly patches in the interferograms. The reason is that the locations of high precipitable water vapor are projected along LOS direction as reported in Kinoshita et al. (2013). Thus the patches of phase anomaly indicate the tropospheric artifact due to strong rain clouds, not the actual crustal deformation.

Refractivity change due to variation of water vapor content in the troposphere also generates artifact phase difference in interferograms (tropospheric artifacts). According to the equation (2.5), the speed of microwave passing through high humidity, such as cloud patch, becomes small because the refractive index for the troposphere is greater than 1. Therefore the phase of microwave delays if the microwave travels through the moist region. Theoretical tropospheric artifact is 10 cm of line-of-sight changes for the 20% of humidity variation (Howard A. Zebker et al., 1997). Several methods for correcting tropospheric artifacts by using numerical weather model, for example, the Weather Research and Forecasting (WRF) model (e.g., Skamarock et al., 2008), and GNSS measurement (e.g., Li et al., 2012) are proposed. After we generate the synthetic phase artifacts using the numerical weather model, the tropospheric artifacts due to the precipitable water vapor can be well-reduced. GNSS measurement can detect the surface movement with the accuracy of sub-centimeters, while the water vapor content also contaminates the measurement accuracy. Phase anomaly due to atmospheric

delay is reduced by using zenith wet delay which is derived from a modeled mapping function. The spatial resolution of precipitable water vapor distribution in the weather model and GNSS measurement are worse than that of InSAR phase difference, while the temporal resolution of InSAR is worse than that of weather model and GNSS measurement. To correct the tropospheric error using the weather model and GNSS measurement, the oversampling, interpolations and data assimilation for refining the spatial resolution need to be applied (e.g., Kinoshita et al., 2013).

Although InSAR is one of the robust techniques for monitoring surface movement using SAR data, some factors usually contaminate processing results. Zebker and Villesenor (1992) described three main factors of decorrelation noise: thermal, temporal, and spatial decorrelations. Thermal decorrelations are induced by an irregular thermal excitation of free electron on sensors. Because the thermal noise can be expressed by the signal-to-noise ratio (SNR), decorrelation problems would be caused at a region with low SNR. Temporal decorrelations are caused by changing of scattering characteristics from a target point between an interval of two image acquisitions, for example, snow covering, volcanic ash covering, flooding, drastic ground deformation. Zebker and Villasenor (1992) investigated variations of decreasing correlation as time passes at regions of a non-vegetated region, forest and lava flow in Oregon. Spatial decorrelations are depended on observation geometries and volumetric scattering. The variation of observation geometry is lead to the difference of incidence angle, and that of Doppler centroid frequency. The volumetric scattering is dependent on radar penetration depths, wavelengths of microwave and scattering objects.

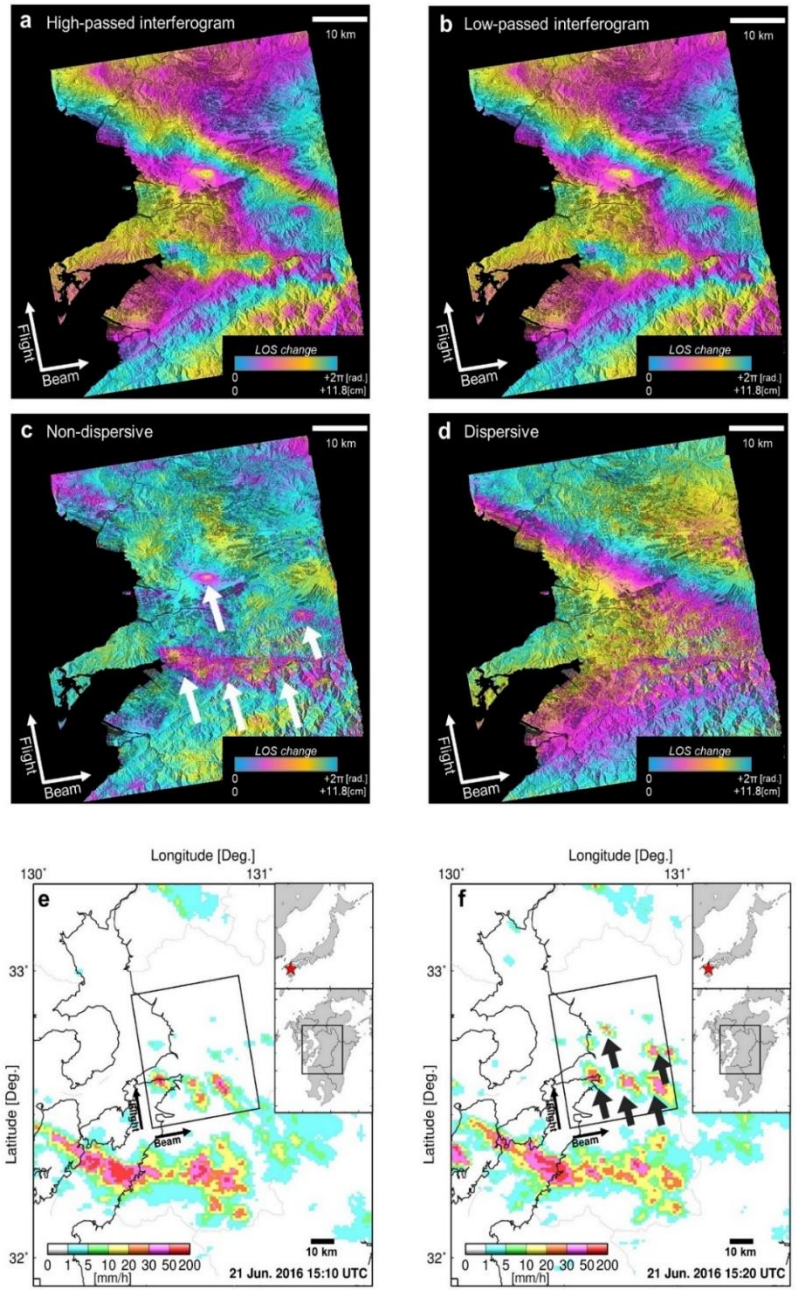


Figure 2-1. An example of the range split-band spectrum method for PALSAR-2 dataset. The original bandwidth is 79.4 MHz. Perpendicular baseline between two SAR images is -112.21 m. Master image was acquired on 10 May 2016, slave image was acquired on 21 June 2016, 15:18 UTC. The reduced bandwidth is 26.4 MHz which is nearly one-third of the original bandwidth. a) High-passed sub-band interferogram, b) Low-passed sub-band interferogram, c) Non-dispersive component, d) Dispersive component. One color cycle in Fig. Xa-d indicates 11.8 cm of line-of-sight displacement. e) Precipitation intensity observed by synthetic radar on 21 June 2016, 15:10 UTC, and f) 15:20 UTC. Red star in Fig. Xe-f indicate the location of study area.

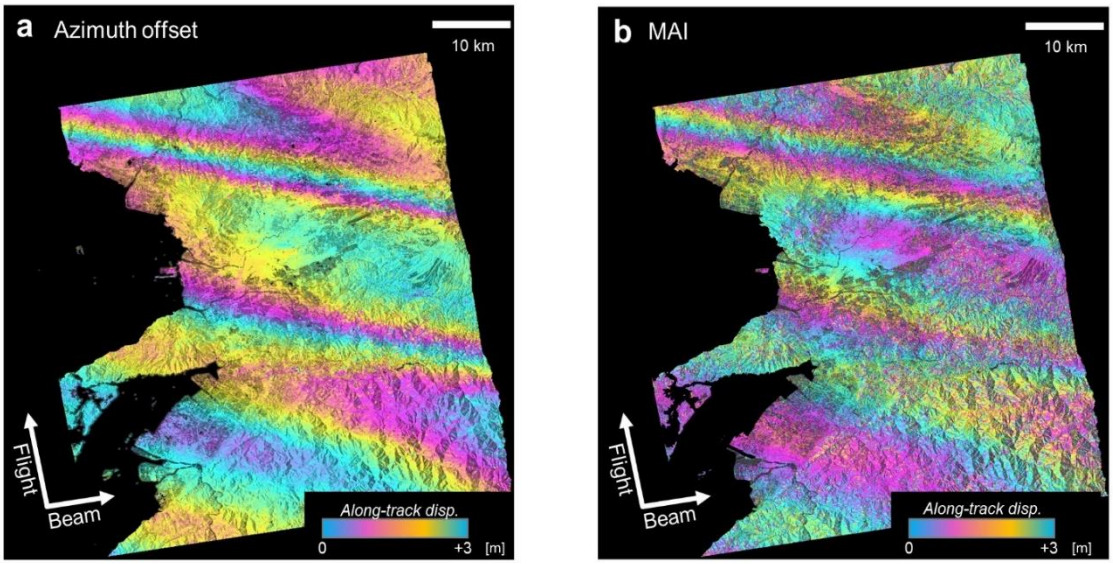


Figure 2-2. Azimuth offset and MAI data which are derived from same PALSAR-2 dataset in Figure 2-1. a) Azimuth offset, and b) MAI data. Azimuth offset and MAI data are sensitive to horizontal displacement along the satellite flight direction. Note that one color cycle in azimuth offset and MAI represents 3 m of horizontal displacement along the satellite flight direction.

We usually evaluate quantitative degrees of decorrelation as coherence. The coherence can be defined by as

$$\gamma = \frac{|< c_1 c_2^* >|}{\sqrt{< c_1 c_1^* >< c_2 c_2^* >}} \tag{2.7}$$

where γ is coherence, which can be ranging from zero to one. Decorrelation problems induce a decreasing value of γ. c_1 and c_2 are average signal values of two SAR image at a pixel, and superscript * means the complex conjugate (Zebker & Villasenor, 1992; Zebker et al., 1996).

Multiple Aperture Interferometry (MAI) is also one of the phase-based SAR processing technique to detect surface movement (Bechor & Zebker, 2006). Because the technique allows us to reveal horizontal displacement along the satellite flight direction, the MAI data makes it easy to

understand the geometry of surface movement. MAI data can be derived by combining forward-looking interferograms from backward-interferograms. These forward-looking and backward-looking SLCs are generated by splitting the Doppler spectrum for azimuth direction, indicating that the filtering bandwidth for azimuth direction. The MAI data allow us to map the relative TEC distribution with high-spatial resolution by integrating phase difference in the azimuth direction (Jung et al., 2013). In this processing, both topographic and orbital fringes between forward- and backward-looking interferograms can be reduced.

The phase difference in MAI φ_{MAI} can be described as

$$\varphi_{MAI} = -\frac{4\pi}{l} nx \tag{2.8}$$

where l is effective antenna length, n is normalized squint x is horizontal displacement along the satellite flight direction. Bechor and Zebker et al. (2006) reported that the measurement accuracy of MAI data depends on the coherence; for example, ~8 cm at the coherence of 0.6. For PALSAR-2 sensor, l = 10 m and we usually employ normalized squint n = 0.5.

2.2.2 Pixel tracking

Other SAR processing method is pixel tracking approach to detect surface displacement. This approach identifies pixel trackings between two coregistered images by linear function using the normalized cross-correlation function (e.g., Michel et al., 1999). Generally, image coregistration is employed affine transformation, which can describe rotation, projection, reflection, shearing and scaling. Affine transformation can coregister outline of images, however local offset on images still remain. While the local offset had been considered as residue, even these offsets can match with sub-pixel accuracy using normalized cross-correlation functions (Li & Goldstein, 1990). The pixel tracking approach measures that residue after linear image coregistration. Therefore, measurement accuracy of

the pixel tracking method strongly depends on accuracy of image coregistration. Accuracy of image coregistration is generally evaluated by coefficient of cross correlation (De Zan, 2014). Other papers considered measurement accuracy of the pixel tracking method as root-mean-square (RMS) around stable (no deformation) region (Kobayashi et al., 2009), RMS between GNSS measurement and pixel tracking results (Fialko et al., 2001; Sandwell et al., 2008) or standard deviations (Strozzi et al., 2002). Low image SNR, large temporal baseline and changing surface condition between two images would cause poor accuracy of image matching. Although advanced techniques of image coregistraion have been improving based on orbital information and DEM (Sansosti et al., 2006) or point scatterers (Serafino, 2006), the normalized cross correlation can identify offset with measurement accuracy of 1/10-1/20 pixels (Strozzi et al., 2002). In other words, higher spatial resolution can identify smaller displacement. Recently, Casu and Manconi (2016) have reported the time-series of pixel tracking data for detection of long-lasting crustal deformations following the Afar dike intrusion in 2005. The pixel tracking approach can be applied to not only SAR images but also optical images for identifying surface movements, for example, Hollingsworth et al. (2012) revealed meter-scale crustal deformations due to the 1975-1984 Krafla rifting episode in NE Iceland by applied the pixel tracking approach to SPOT5 optical images and aerial photos(Fahnestock et al., 2016).

The pixel tracking method has mainly two advantages comparing with interferograms. First, the method can identify surface movement with high displacement gradient. Because the cross-correlation identifies offsets on SAR images itself, we can avoid unwrapping error at the high displacement gradient. Therefore the approach can also detect the location of surface rupture due to large earthquake at shallow depth. Theoretically, decorrelation problem could be caused if displacement gradient is larger than a half of radar wavelength per pixel (Baran et al., 2005). For example, threshold of displacement gradient of PALSAR-2 interferograms observed by SM3 mode is

27.4 mm/m. The other advantage is that the method can reveal two displacement components: one is sensitive to the line-of-sight direction (range offset), and the other is sensitive to the along-track direction (azimuth offset). In order to retrieve three-dimensional displacement using interferograms, we must process any three datasets from ascending track, descending track, right-looking or left-looking observation. If we applied the pixel tracking method to the dataset observed from both ascending and descending track, independent four displacement components are revealed. Using these four displacement components, we can retrieve three-dimensional displacement by solving over-determined least square problem. First three-dimensional displacement using the pixel tracking method have reported by Tobita et al. (2001).

On the other hand, the pixel tracking approach contains two disadvantages. One is that the spatial resolution of pixel tracking is worse than that of interferograms. The approach requires arbitrary window size to identify a peak of cross correlation where the location of peak is recognized as residue. Thus, the window size is consistent with the spatial resolution of pixel tracking. Generally, window size is set from 32 to 256 pixels. The smaller windows size can identify local displacement features, but the uncertainty would be large. In contrast, the larger window size can reveal reliable pixel trackings, but the spatial resolution is worse. The other disadvantage is low measurement accuracy. Interferograms can identify a few centimeters displacement, however the pixel tracking approach can detect ground deformations with 1/10-1/20 pixels of measurement accuracy.

Another characteristic is that azimuth offset is easier to be contaminated by ionospheric artifacts (Gray et al., 2000; Meyer, 2011). Although there are some factors of ionospheric noise, the strongest factor is that the ionospheric disturbances at E and/or F layers cause ray-bending of microwave. Multiple aperture interferograms (MAI) are also easier to be contaminated by same reason

(Bechor & Zebker, 2006; Jung et al., 2009).

2.2.3 Time-series analysis

Another SAR processing approach is time-series analysis, which are not mainly adopted in this thesis. Time-series analysis for SAR data is suitable for detecting long-lasting small displacement, for example, subsidence at urban area, volcanic deformation due to magma source inflation/deflation. Signal of actual small deformation and atmospheric/ionospheric artificial errors cannot be distinguished within an interferogram, because these signal amplitudes are nearly same. Time-series analysis approaches need to process many SAR data over same region for identifying slow and small movement, however randomly-appearing artificial errors are cancelled out. These approaches can detect displacement rate of sub-centimeters per year if the processing condition is good. Generally, increasing number of image and small spatiotemporal baseline make it possible to improve the measurement accuracy. Another advantage comparing conventional InSAR is avoiding temporal decorrelation problem. Although longer interval of SAR data acquisition induces temporal decorrelation, the time-series analysis can reveal long-term continuous deformation. To apply the time-series analysis, Stanford Method for Permanent Scatterers (StaMPS) software is one of the famous non-commercial software for processing time-series analysis (Hooper et al., 2004).

Most famous analysis methods are conventional stacking, Permanent Scatterer InSAR (PS-InSAR), and Small-Baseline Subset (SBAS). Conventional stacking approach estimates average deformation rates by dividing cumulative displacement by each data acquisition interval (e.g., Zebker et al., 1997). Atmospheric artificial errors are eliminated by averaging multi interferograms. Although conventional stacking is superior to detect signals with constant displacement rate, it is inferior to detect signals with seasonal trend and/or fluctuation. Others two approaches can identify displacement

rates with variations.

PS-InSAR approach can detect LOS displacement at permanent scatterer (PS) points, where phase coherence is stable during the acquisition period (Ferretti et al., 2000, 2001). Artificial objects, for example buildings in metropolitan areas, tend to be PS points which are stable of characteristics of backscatter intensity, while vegetated region where temporal backscatter intensity varies is hard to be PS points. The pixels containing stable coherence points can avoid temporal and spatial decorrelation problems. PS points are selected by using criterion of phase coherence or SAR intensity dispersion (Ferretti et al., 2000, 2001). Hooper et al. (2004) reported that vertical deformation from 1992 to 2000 was detected at Long Valley Caldera in California by applying PS-InSAR approach to ERS-1/2 dataset. The temporal variation of the vertical deformation is almost consistent with their electric distance meter (EDM), leveling, and GPS measurements. The paper also suggested that PS-InSAR is superior to avoid temporal decorrelation by comparing conventional InSAR and PS-InSAR data.

SBAS infers the displacement rate by analyzing SAR dataset with small spatiotemporal baselines (e.g., Berardino et al., 2002; Schmidt & Bürgmann, 2003). Interferograms with small spatiotemporal baseline also allows us to minimize decorrelation noise even if there is no scatterer in pixel. Pixels are selected better points based on spatial coherence maps. That's why SBAS utilizes several master images, while PS-InSAR select single master image to reveal time-series of displacement. PS-InSAR selects single After extracting time-series of deformation signal, filtering the inferred time-series results in both time and space domain decompose tropospheric artificial errors from the average displacement rate. Schmidt and Bürgmann (2003) have reported vertical movement due to seasonal variations of groundwater level at the Santa Clara Valley, California, by applying SBAS approach to ERS-1/2 dataset.

Chapter 3

Aseismic Strike-slip on Graben Subsidence Associated with the 2007 Natron Dike Intrusion Episode, Tanzania

The contents of this chapter have been published in *Tectonophysics*

Himematsu, Y., M. Furuya (2015) Aseismic strike-slip associated with the 2007 dike intrusion episode in Tanzania, *Tectonophysics*, 656:52-60, DOI 10.1186/s40623-016-0545-7

Chapter 3. Aseismic strike-slip along graben subsidence associated with the 2007 Natron dike intrusion episode, Tanzania

3.1 Introduction

The East African Rift (EAR) valley is a divergent plate boundary between Nubian plate and Somalian plate that extends the length of ~5000 km-long from Ethiopia to Mozambique (e.g., Ebinger, 1989; McKenzie et al., 1970). The EAR contains numerous normal faults and Quaternary active volcanoes along the rift (e.g., Hamling et al., 2009; Paquet et al., 2007). Also, moderate-sized earthquakes frequently occur along the plate boundary (e.g., Chorowicz, 2005). Northern Tanzania is located in the middle of the EAR, and the relative opening rate is 2–4 mm/yr along the E–W direction according to the GPS measurement (Saria et al., 2014; Stamps et al., 2008). The 2007 swarm near the Lake Natron started on July 12 (e.g., Calais et al., 2008). The largest earthquake with moment magnitude (Mw) 5.9 occurred on July 17, and the swarm activity continued until the middle of September 2007 (Figure 1). The campaign-based local seismic network revealed the details of spatial–temporal distribution of epicenters, indicating a migration of earthquake swarm from a deeper depth to the SW toward a shallower depth in the NE (Albaric et al., 2010). Albaric et al. (2010) and Global CMT catalogue (http://www.globalcmt.org) reported that eight earthquakes with magnitude larger than 5 occurred during the event, all of which indicated ENE–WSW striking normal fault at depths shallower than 20 km. A swarm of more 1400 earthquakes was recorded for 180 days by a campaign seismic network since June 1 (Albaric et al., 2010). Earthquake swarms are often accompanied with magma intrusion (e.g., Aoki, 1999). Mt. Oldoinyo Lengai located about 20 km to the SW from the swarm, is one of the most active volcanoes along the EAR. In 2007, an effusive eruption started one month prior to the swarm activity for the first time in 24 years. The eruptive activity of Mt. Oldoinyo Lengai abruptly switched to episodic explosive eruptions when the swarm activity was decaying in

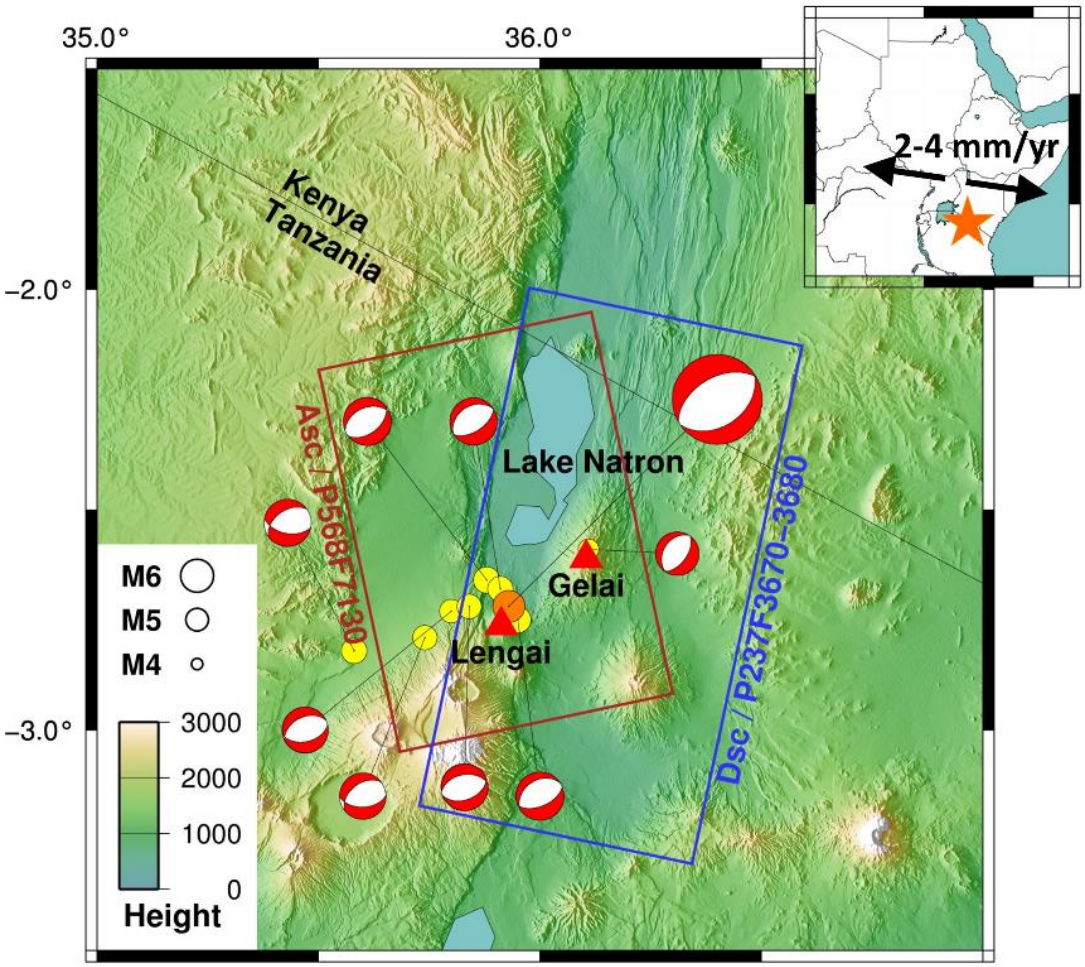


Figure 3-1. Study area in Chapter 3. Yellow and orange circles indicate the locations of epicenter of greater than M5 earthquakes and that of a mainshock during the 2007 event, respectively. Beachballs show each focal mechanism. A wide map of the study area is shown at the upper-right of the figure. Colored rectangulars indicate footprints of the PALSAR data we used in this chapter. Star represents the location of study area. Black arrows show the far-field displacement direction derived from the GPS measurement (Saria et al., 2014; Stamps et al., 2008).

September and continued until April 2008. Several previous studies have already reported the crustal deformation signals associated with the swarm by using satellite synthetic aperture radar (SAR) data (Baer et al., 2008; Biggs et al., 2009; Calais et al., 2008). Calais et al. (2008) pointed out the presence of aseismic slow slip besides the dike intrusion and examined the details of the dike intrusion processes using the high temporal resolution SAR data. Baer et al. (2008) examined the Coulomb stress changes

associated with the event to study the interaction of each fault source. Biggs et al. (2009) studied the relationship between the length of dike and the size of magma chamber compared with those in Afar and Iceland events. In regard to the relationship between the Oldoinyo Lengai eruption and the swarm, Baer et al. (2008) considered that the passage of the seismic-wave through the magma chamber could dynamically trigger the eruption, whereas Biggs et al. (2009) reported that there was no relationship between the eruption and the swarm due to the ground deformation spanning 2001–2004 implies no significant pressure changes in the magma chamber. Thus, the interrelation between the eruption and the event is still uncertain. The objectives of this paper are to report the three-dimensional (3D) displacement fields that have never been reported by the previous studies and to show our source modeling results. This was made possible by a couple of reasons. Firstly, in contrast to the previous studies, we used L-band ALOS/PALSAR images acquired from both ascending and descending tracks. The L-band SAR is more advantageous in terms of the easiness of phase unwrapping even the areas with large phase gradient. Secondly, we apply both InSAR and offset-tracking methods that can reveal the full 3D displacements. Based on the inferred fault slip model, we also discuss the implications for the regional stress field and their possible role for the generation of fault segmentation along the rift axes. Moreover, we point out the possibility of the aseismic slip as the driver of earthquake swarm.

Table 3-1. ALOS-1/PALSAR-1 dataset in this chapter

Pair No.	Date (dd.mm.yyyy)	Orbit	Path	Frame
1	07.07.2007-07.10.2007	Asc.	568	7130
2	05.06.2007-13.06.2007	Dsc.	236	3670-3680

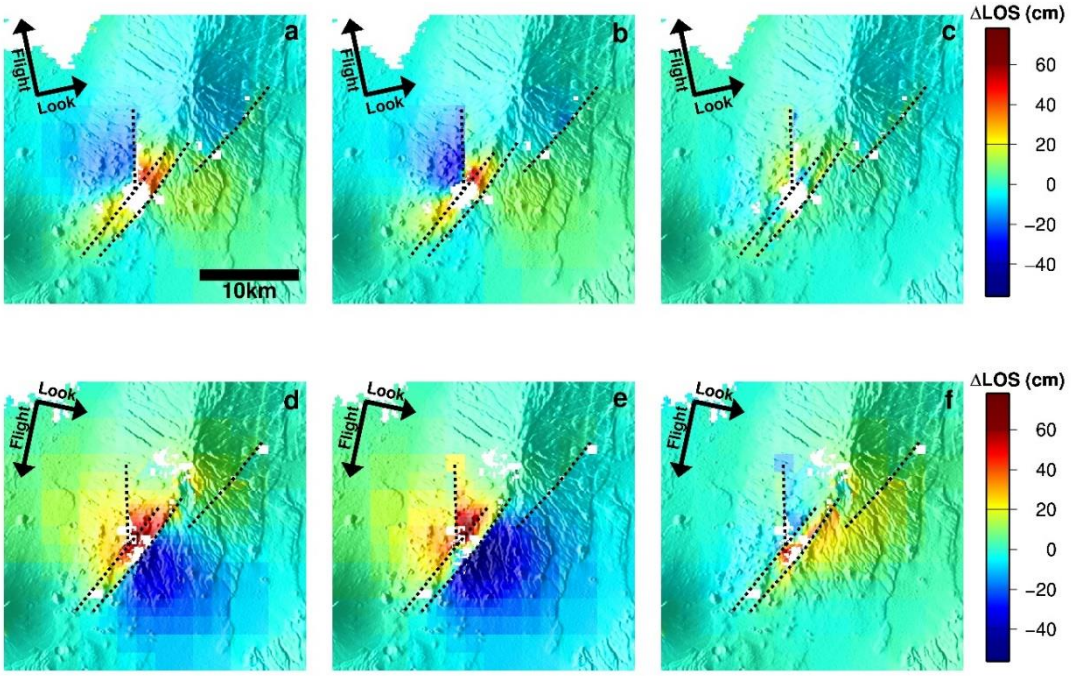


Figure 3-2. Subsampled PALSAR-1 InSAR data which show co-diking displacement associated with the 2007 Natron dike intrusion episode. a-c) Unwrapped PALSAR interferograms observed from ascending track. a) Subsampled observation, b) calculation, and c) misfit residual. d-f) Unwrapped PALSAR interferograms observed from descending track. a) Subsampled observation, b) calculation, and c) misfit residual. Black dot lines traced the top locations of fault segment in our elastic model (see Figures 3-4 and 3-6). Positive signals represent displacement along the line-of-sight away from the satellite.

3.2 Methods and results

Satellite-based SAR is helpful to obtain ground surface deformation signals with unprecedented spatial resolution over wide areas (e.g., Hanssen et al., 2001; Massonnet & Feigl, 1998). We detected the deformation signals associated with the 2007 event using both ascending and descending ALOS/PALSAR (L-band, 23.6 cm wavelength) images (Table 1), providing us with the range changes along the radar line of sight (LOS) from two independent directions. We also applied the offset-tracking method to derive the displacements projected along the satellite flight direction. We could

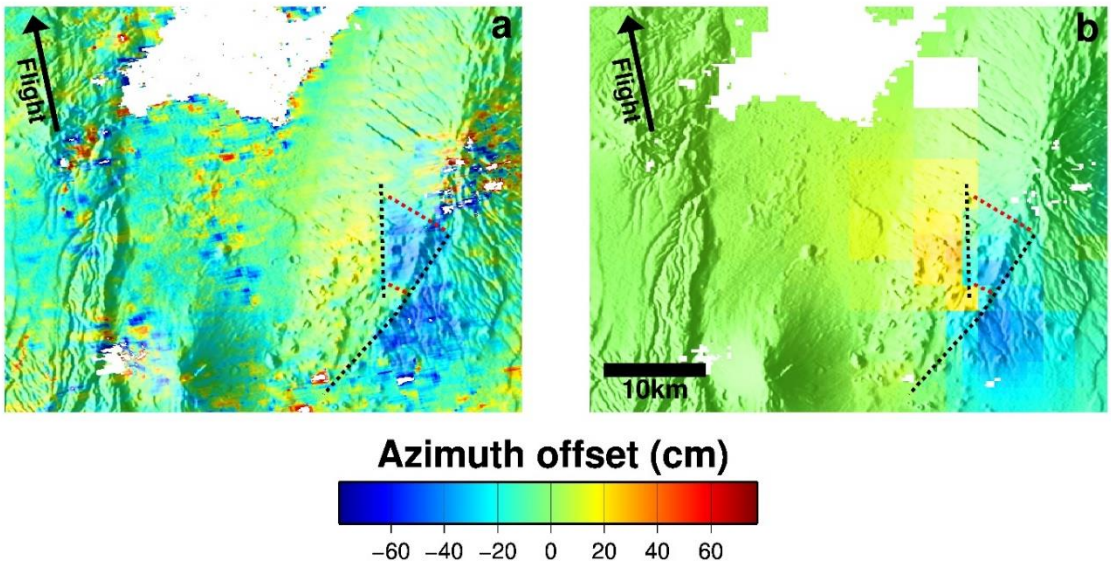


Figure 3-3. Observation and calculation of azimuth offset for ascending orbit. a) Observed azimuth offset derived from PALSAR ascending track (Pair No. 1 in Table 1). b) Simulated azimuth offset derived from the inferred opening/slip distributions in our optimal model (see Figure 3-6). Black dashed lines represent the top of the two facing faults. The two phase discontinuities along the direction orthogonal to the fault strike are indicated by red dots lines. Upper-right arrows show the direction of the satellite flight direction.

thus derive the 3D displacements associated with the entire episode. The off-nadir angles are 34.3° for both tracks. The ascending data set (7 July 2007 to 7 October 2007) and the descending data set (5 June 2007 to 13 June 2010) cover the entire swarm period (Figure 1). While the temporal coverage of the descending InSAR image is much longer than that of the ascending InSAR image, because no descending images were acquired between July 2007 and June 2010, and the descending InSAR could include post-seismic deformation signals. However, we confirmed insignificant deformation signals after October 2007 from the ascending post-seismic interferogram (7 October 2007 to 15 July 2010) that revealed very little deformation (Fig. S2). To remove the topographic fringes in InSAR data, we used the 3 arc-second (90 m) Shuttle Radar Topography Mission (SRTM) digital elevation model (DEM) (Farr et al., 2007). SAR data were processed by GAMMA software (Wegmüller & Werner,

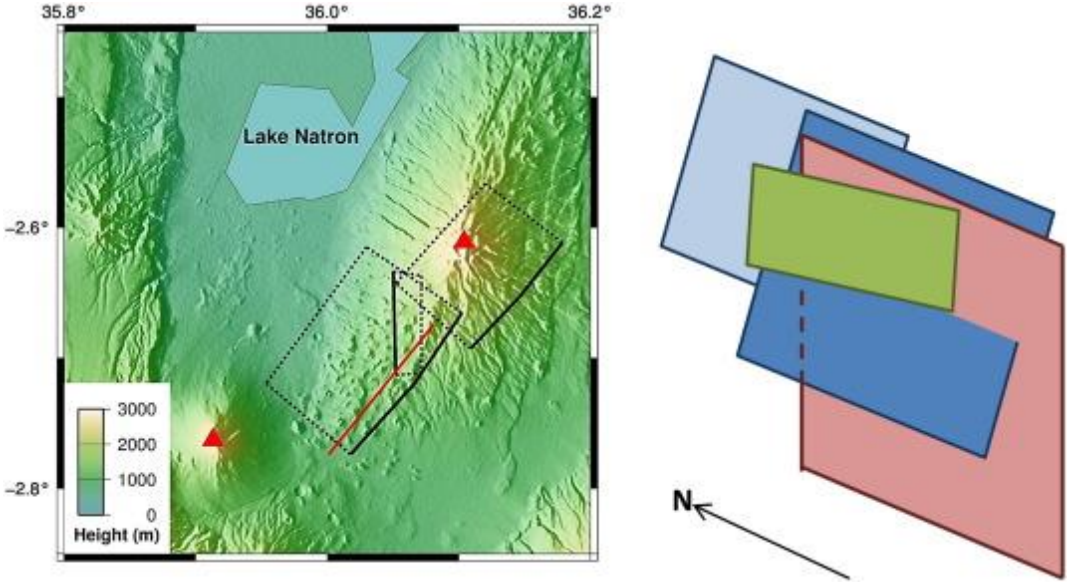


Figure 3-4. Surface projection and 3D description of our optimal elastic model. (Left) Solid lines mark the top edge of the faults, and the dashed lines indicate the side and bottom edges of the faults. Red indicates the location of the dike segment. (Right) Blue segments indicate east-dipping faults, green segment is east-dipping fault, and red segment is dike. The inferred slip distributions are shown in Figure 3-6.

1997). Although we corrected for the orbital and topographic fringes with the use of precision orbit data by JAXA and SRTM DEM, respectively, there still remain long-wavelength phase trends and topography-correlated fringes. The effects of long-wavelength trend and topographic-correlated atmospheric delay in the interferograms were removed, by fitting low-order polynomials and DEM, respectively. For phase unwrapping, we used the branch-cut algorithm z(Goldstein et al., 1988). While the unwrapping error would appear at different locations in the ascending and descending data, we confirmed that the phase discontinuities were observed at the same locations, suggesting that they are real deformation signals. The observed InSAR data for both ascending and descending tracks are shown in Fig. 2a and d. They are resampled with the quad-tree algorithm to effectively reduce the number of data points from ~25,000 to ~4000 (Jonsson et al., 2002). The two interferograms indicate two clear phase discontinuities around the center of the graben that strike NE–SW (36.10E, 2.66S–

36.01E, 2.77S) and NNW–SSE (36.05E, 2.63S–36.05E, 2.71S). We also identify another phase discontinuity to the NE that is particularly clear in Fig. 2a. The area between the two discontinuities indicates an increase in the radar line of sight (LOS) in both ascending (Figure 2a) and descending data (Figure 2d), suggesting that the area has subsided. In contrast, outside this region the signal in the ascending and descending data is opposite, suggesting E–W motion (Figures 2a and 2d). We can thus roughly interpret that the LOS-increasing area was subsiding, and that the outer eastern and western areas were moving to the east and west, respectively. The interferograms indicate that the subsidence area covers 3–4 km width and 13–15 km length. The maximum positive range changes are 46 and 63 cm in ascending and descending data, respectively. Overall, the spatial pattern of the deformation signals looks like a graben structure, which has been reported at other rifting episodes such as the 2009 western Arabia, the 2007 Dallol, and the 1998 Réunion island (Baer & Hamiel, 2010; Fukushima et al., 2010; Nobile et al., 2012). As shown below, however, the azimuth offset data exhibit some unexpected signals. Azimuth offset data derived from the ascending path similarly indicates two discontinuities (Figure 3a) that are compatible with the expanding areas with E–W motion in the interferograms (Figures 2a and 2d). The most remarkable point is that the subsiding zone indicates ~40 cm negative offset, which indicates that the area has moved opposite to the satellite flight direction. Namely, the central subsiding region was not only subsiding but also moving horizontally, because the azimuth offsets have no sensitivities to the vertical displacements. Although the azimuth offset derived from the descending pair is much noisier due to the lower-coherence, the data set also exhibits small horizontal displacements that are nearly in parallel with the satellite flight direction (Fig. S1). The azimuth offset data from both ascending and descending tracks thus unambiguously indicate horizontal displacements of a subsiding graben structure. Biggs et al. (2009) showed a result from multiple aperture InSAR (MAI) measurement (Bechor & Zebker, 2006), which are quite consistent with Fig. 3a in terms of both the signal amplitude and the deforming area. Nevertheless, they dismissed

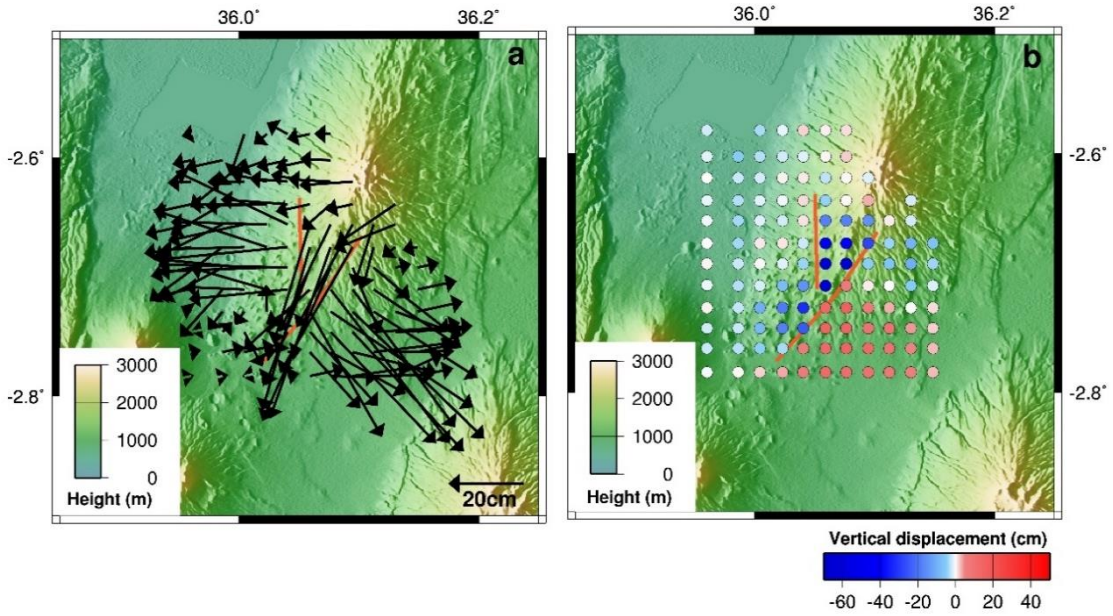


Figure 3-5. 3D displacement inferred from PALSAR-1 interferograms and pixel tracking data. (a) Horizontal displacement, and (b) vertical displacement. Orange solid lines indicate the top locations of the fault segments in out model.

the MAI observation in their analyses, probably because there were no other independent data that could support the signal. We calculated 3D displacements from the ascending and descending interferograms and the azimuth offset (Figure 5a) (Fialko et al., 2001). The orange lines in Figure 4 show the locations for the top edges of our fault source models shown below. The interval of the observation point is 2 × 2 km. The lack of the points around the summit of Mt. Gelai is because the azimuth offsets are noisier than the InSAR data and thus such area are masked. The horizontal displacements in Fig. 5a indicate that the western and the eastern half of the areas moved up to ~35 cm toward W–WSW and ~51 cm toward E–NE, respectively. The subsidence zone moved toward SSW direction with a maximum horizontal displacement of ~48 cm. The vertical displacements are shown in Figure 5b, which indicates that the eastern half was uplifting, and the center area was subsiding by ~62 cm. In contrast, the western half was uplifting by only a few centimeters.

3.3 Elastic source model

Static ground displacements associated with earthquakes and/or dike intrusion episodes are often interpreted by using analytical solutions due to planar rectangular dislocation elements in elastic half-space (Okada, 1985). In this study, we estimate non-planar fault planes based on the analytical solutions due to triangular dislocation elements because the observations reveal complex deformation signals. The triangular dislocation elements are advantageous because it can represent non-planar fault planes without making unrealistic overlaps or gaps (Furuya & Yasuda, 2011; Maerten et al., 2005). To calculate the ground deformation due to the triangular dislocation elements, we use the MATLAB script that is made available by Meade (2007). To generate the mesh coordinates for the non-planar planes, we used Gmsh software (Geuzaine & Remacle, 2009). Almost all the focal mechanisms of the earthquakes during the event show normal faulting. We set a west-dipping and an east-dipping fault whose top edges can match the locations off the phase discontinuities in the interferograms (Figures 4 and 6); the other parameters for the fault geometry, the bottom location and depth, were estimated by trial-and-errors (e.g., Furuya & Yasuda, 2011). We set another west-dipping fault at the eastern flank of Mt. Gelai (Figure 6e–f), because the two interferograms indicate a phase discontinuity at the same location. The deformation pattern is consistent with a dike intrusion and can be modeled as a tensile opening dislocation source. We set a vertical tensile dislocation source as the dike segment, whose horizontal location is the center of the subsidence zone. Without dike opening, we could have only reproduced the subsidence zone with smaller E–W extension displacement. The final position of the dike segment was set where the RMS misfit was minimum. We thus estimated three faults and one dike segment to explain the crustal deformation (Figure 5). Our model is similar to the geometry of Baer et al. (2008), regarding an east-dipping fault, two west-dipping faults and a dike segment. After setting the location and geometry of the fault sources and dike, we performed a linear least squares inversion to derive the spatially variable slip and opening on the fault and dike, inverting jointly the

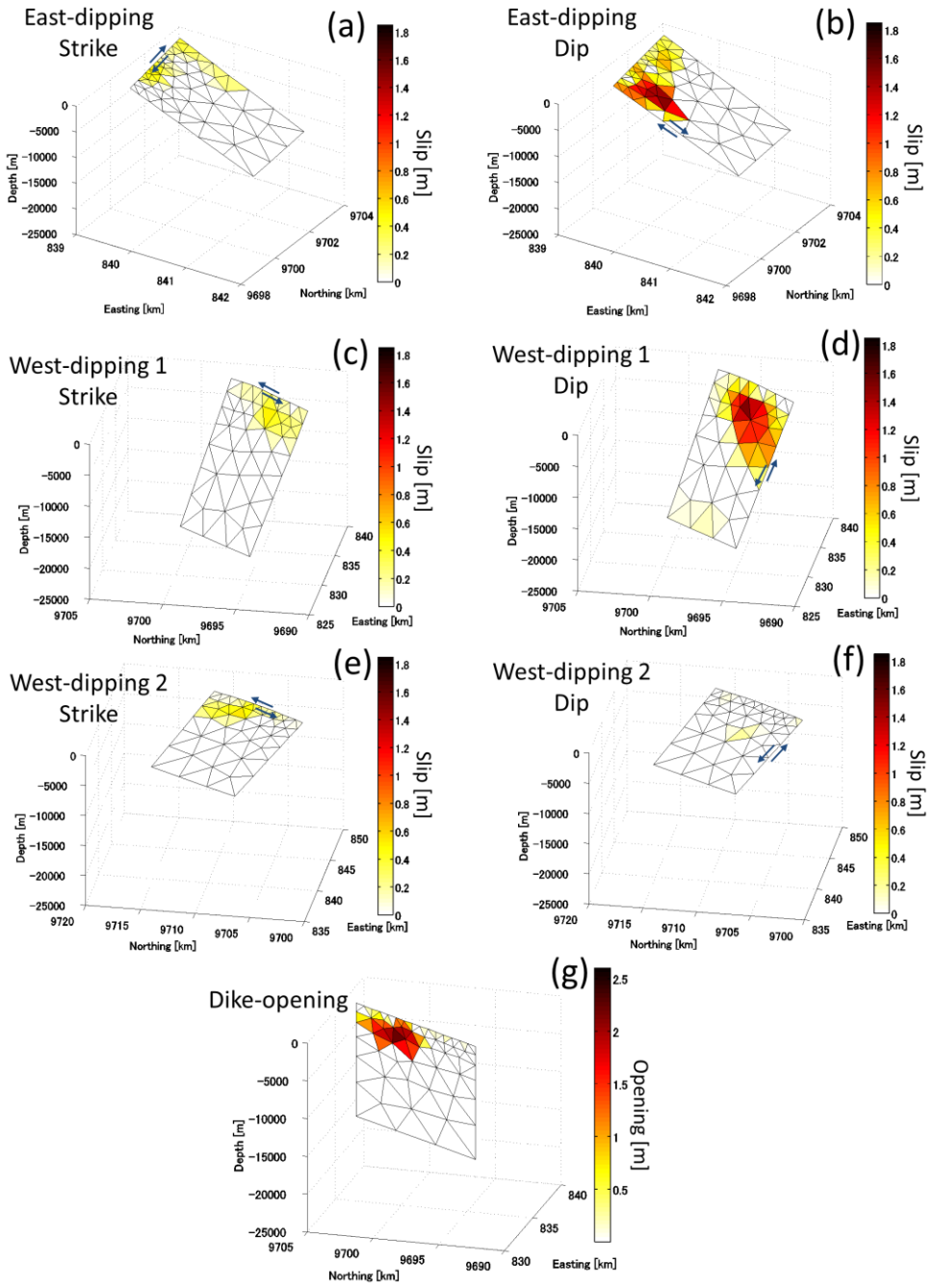


Figure 3-6. The inferred dike opening and slip distributions. Distribution of (a) Strike-slip and (b) normal faulting along the east dipping fault. Distribution of (c) Strike-slip and (d) normal faulting along the west-dipping fault 1. Distribution of (e) Strike-slip and (f) normal faulting along the west-dipping fault 2. (g) Opening distribution along the dike. All figures are plotted in the UTM coordinate (Zone 36).

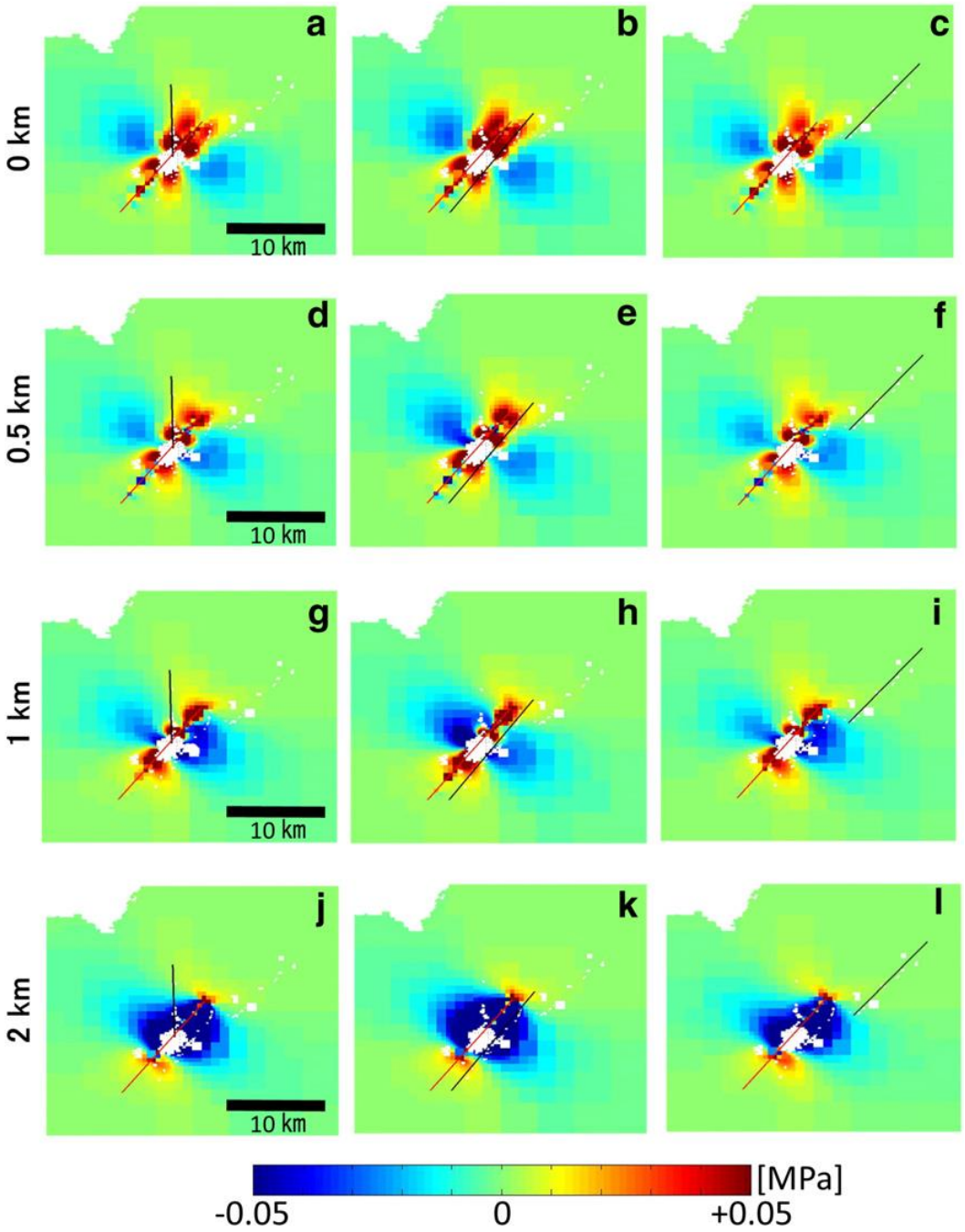


Figure 3-7. Coulomb stress changes for each receiver fault (black lines) due to the dike opening as the source fault (red line). The top edges of the receiver faults are shown as black lines (left column: east-dipping fault, center: west-dipping fault, right: shallow west-dipping fault). Stress changes indicate positive (unclamping) the near surface, and the most negative (clamping) at the depth of maximum dike opening around 2–3 km.

ascending and descending interferograms. Here we do not invert for the azimuth offset data, and instead we check the consistency a posteriori as argued below. In solving the least squares problem, we applied a "non-negativity" constraint. Namely, in order to derive physically plausible slip distributions, we prescribed that the east-dipping and west-dipping faults are allowed to slip right-laterally and left-laterally, respectively, and that the dip slip on each segment has only normal slip component. The dike segment is allowed to have only pure opening. Moreover, we apply a smoothing constraint on the slip distribution by using an umbrella operator that is equivalent to the Laplacian operator for the rectangular dislocation elements (Maerten et al., 2005). The moment release from the fault lip distribution can be calculated, assuming Poisson ratio of 0.25 and shear modulus of 30 GPa. The optimum fault slip and dike opening distribution on each segment are shown in Fig. 6. Each fault slip distribution has maximum amplitude around the depth of ~5 km with their amplitudes up to 60 cm in the strike–slip and 160 cm in the dip slip. As expected from the Global CMT solutions that indicate predominantly normal faulting, the normal slip is much larger than the strike–slip (Figures 6b and 6d). However, the inferred strike–slip component is unexpectedly larger than that inferred by seismology (Figure 6a and 6c). The calculated geodetic moment for the dip slip component is 3.3×10^{18} Nm, and that for the strike–slip component is 8.1×10^{17} Nm. Thus, the contribution of the strike–slip is 19.9%, and the equivalent moment magnitude for the dip slip and strike–slip is Mw 6.28 and 5.87, respectively. Because the cumulative seismic moment is 2.2×10^{18} Nm according to the Global CMT, it turns out that about 56% of the geodetic moment were released aseismically. The moment for the strike–slip must be responsible for the southward movement of the subsidence zone. The dike segment exhibits up to 220 cm opening at the depth of 2–4 km (Figure 6g), and the volume of intrusion is 0.036 km^3. While we may include a Mogi-type deflation source to account for the source of the intruded dike, we cannot identify any circular signals in the observed InSAR data that allows us to constrain such a source. Although we do not discard the presence of a deflation source, we consider

that the depth of the Mogi source, if any, would be deeper than 3 km, because otherwise there would arise circular fringes; we then assumed that the Mogi source has the same volume changes as those of intruded dike. Moreover, even if we include the deflation source at the center of the largest displacement field, the E–W trending sharp offset at northern and southern edge of the negative signal will never be generated.

Based on the inferred fault slip and dike opening distribution, we computed the ground deformation (Figures 2b and 2e) and misfit residual (Figure 2c and 2f). RMS residual values in our model are 3.0 cm in the ascending and 6.3 cm in the descending data. Although there still remain some residuals in the eastern half of the descending data, the calculated deformation well reproduces the observations, and the misfit residuals cannot be distinguished from measurement errors that would be empirically less than 5 cm for a single interferogram. Also, we calculated the displacements for the azimuth offset, which also reproduces the characteristic offsets in the subsidence zone (Figure 3). Without the strike–slip component, we could not reproduce the large azimuth offset signals in the subsidence zone. Thus we conclude that the strike–slip is necessary to explain the observation results, and it occurred aseismically because almost all the Global CMT solution exhibits the normal-dip slip.

3.4 Discussion

To our knowledge, not only the previous studies of the 2007 Lake Natron event, but also many studies of dike intrusion events in rift settings elsewhere assume normal slip and dike opening in their fault source modeling (e.g., Baer & Hamiel, 2010; I. J. Hamling et al., 2014; Nobile et al., 2012; Wright et al., 2006). Focal mechanisms of earthquakes during the 2007 event indeed indicate few strike–slip components. In contrast, the fault source model we estimated in this study includes significant strike

components, without which we cannot reproduce the InSAR and azimuth offset observations. Considering the few strike–slip in the focal mechanisms, it turns out that aseismic strike components are required to explain the ground deformation associated with the 2007 Natron event. Why then did the aseismic strike–slip occur at the area that is supposed to extend in the E–W direction? Why did the subsiding area move toward the south that is orthogonal to the rift axis? In order to examine if the stress changes due to the dike intrusion promoted the fault slips, we computed the Coulomb stress changes (ΔCFF), based on our inferred fault models (e.g., King et al., 1994; Toda & Stein, 2002). In the calculations of the ΔCFF, we use a shear modulus of 30 GPa and a friction coefficient of 0.4. Figure 7 illustrates the distribution of the ΔCFF by the dike opening for each receiver fault at depths from the surface to 6 km. We observe positive values of ~0.05 MPa at shallower depths, suggesting unclamping, mainly distributed along the dike axis (Figures 7a–f). In the meantime, at the depths of 2–4 km at which we inferred the peak values of dike opening, the negative ΔCFF (clamping) are widely distributed (Figures 7j–r). Our inferred fault models indicate significant slip distributions mostly at shallower depths, and thus are mechanically consistent with the ΔCFF. In the above ΔCFF modeling, however, we do not consider the background tectonic stress fields. The two west-dipping faults are forming en-echelon structure, and the strike components are much larger than the normal slip at the shallower depth of the west-dipping fault to the northeastern end. There are many normal fault systems in the EAR, which are forming relay zones and segmented structures (Ebinger, 1989; Moustafa, 2002; Tesfaye et al., 2008). Relay zone is a geological structure formed by multiple overlapping, en-echelon fault segments and develops under a transtensive stress field instead of pure extension (Crider & Pollard, 1998). The background stress field around the Lake Natron has been estimated from the focal mechanisms of past earthquakes (Delvaux & Barth, 2010; the World Stress Map available online at http://www.world-stress-map.org). Those studies indicate a pure extension stress regime toward NNW–SSE around the Lake Natron. The NNW–SSE axis is consistent with the orthogonal direction

of the main shock strike direction during the 2007 event. Moreover, Delvaux and Barth (2010) and the World Stress Map indicate ENE–WSW pure extensive stress field in the Lake Manyara region, which is located 50 km to the south from the 2007 Natron rifting event area. The stress field estimated from seismological studies, however, indicates seismotectonic stresses, and the stress field can change at the other depths than the depth of the employed hypocenters. It is likely that the existence of a microplate or magma intrusion can build up a three-dimensionally complicated stress field. As shown in the slip distribution in Figure 6, the strike–slip is dominating at the shallower depth, suggesting the transcurrent stress regime. Meanwhile, it is well-known that the shallowest zone of the crust exhibits a velocity-strengthening tendency in the friction parameters of the rate-and-state dependent friction law, meaning the absence of seismic slip and the presence of aseismic slip (Scholz & Contreras, 1998). In other words, it should be noted that we cannot infer a true stress regime at the shallowest depths from seismological studies, no matter what type of stress fields are dominant. Thus we may claim that this study is the first to have confirmed the transtensive stress regime at shallower depth around the Lake Natron by the detection of the aseismic strike–slip based on the InSAR data. Although Wright et al. (2006) suggested that dike intrusion is essential to form the along-axis segmentation, and we do not dispute its importance, our detection of significant strike–slip at shallow depth is a direct evidence for the presence of transtensive stress that is necessary to generate the along-axis segmentation like relay zone (transfer zone). We consider that the dike intrusion could contribute to generate the three-dimensionally complex stress distributions. Since our dike opening model sets a kinematic displacement boundary condition instead of stress boundary condition, we should note that the stress axis around the study area does not have to coincide with the dike opening direction. The relay ramp is known to form between antithetic normal faults like graben structure (Amer et al., 2012; Tesfaye et al., 2008). As the relay ramp develops, a fracture can be built up along the direction orthogonal to the fault strike direction, generating new normal faults as transfer faults (Commins et al., 2005; Xu et al.,

2011). Such fractures are also observed at the Northern Lake Rukwa (Chorowicz, 2005). While we do not include it in the source model of this study, we can identify such discontinuities in the azimuth offset observation as indicated by the red dashed line (Figure 3). We consider that those discontinuities would also be the evidence for the horizontal motion of the subsiding region. The observed aseismic slip may also have an important implication for generation of earthquake swarm (Lohman & McGuire, 2007; Takada & Furuya, 2010; Wicks et al., 2011). Earthquake swarm is often attributed to fluid or magma intrusion, and it is apparent that such an intrusion occurred during our studied period. However, besides the dike intrusion process, aseismic slip has been proposed as another possible driver of swarm episode. We may regard the detected aseismic strike–slip as another evidence for the proposed swarm mechanism.

Chapter 4

Along-Rift Horizontal Displacement on Graben Subsidence during the 2005-2010 Afar Dike Intrusion Episode Detected by PALSAR-1 Data

The contents in this chapter are preparing to submit to the *Journal of African Earth Sciences*

Himematsu, Y., M. Furuya, Rift-parallel block-like motion on the graben floor during the 2005-2010 dike intrusion episode, *in preparation*.

Chapter 4. Along-rift horizontal displacement on graben subsidence during the 2005-2010 Afar dike intrusion episode detected by PALSAR-1 data

4.1 Introduction

Afar is a triple junction of the subaerial divergent plate boundaries between Arabian, Somalian and Nubian plate (Figure 4-1) (McKenzie et al., 1970). While the geodetic observations indicate the largest steady spreading along the East African Rift (Kreemer et al., 2003; Stamps et al., 2008), dike intrusion episodes intermittently occur along the continental rift zones, accompanying significant ground displacement (Wright et al., 2006; Calais et al., 2008). The 2005-2010 Afar rifting episode was one of the long-lasting dike intrusion episodes, which took place along the Manda-Hararo Dabbahu magmatic segment that is located Nubian-Arabian plate boundary (Figure 4-1). Previous studies have indicated the three dimensional (3D) displacements due to the September 2005 event from satellite synthetic aperture radar (SAR) and optical images (e.g., Wright et al., 2006; Grandin et al., 2009, 2010; Hamling et al., 2009). Spatial pattern of the derived crustal deformation showed an archetypical graben structure; the uplifted graben shoulders were extending from NE to SW, and the narrow graben floor subsided by up to 3 m. Those displacement data were helpful to understand the kinematics of the dike intrusion (Wright et al., 2006; Grandin et al., 2009, 2010b; Hamling et al., 2009). Ground displacements of the subsequent events after June 2006 (Events 2-14) were also derived by interferometric SAR (InSAR) data. However, we should keep in mind that the displacement data over the graben floor were lacking due to the phase decorrelation problem of the C-band ENVISAT data (Hamling et al., 2009; Hamling et al., 2014); we follow Hamling et al. (2009) and Wright et al. (2012) for the numbering of the sequential events, and the September 2005 event is Event 1.

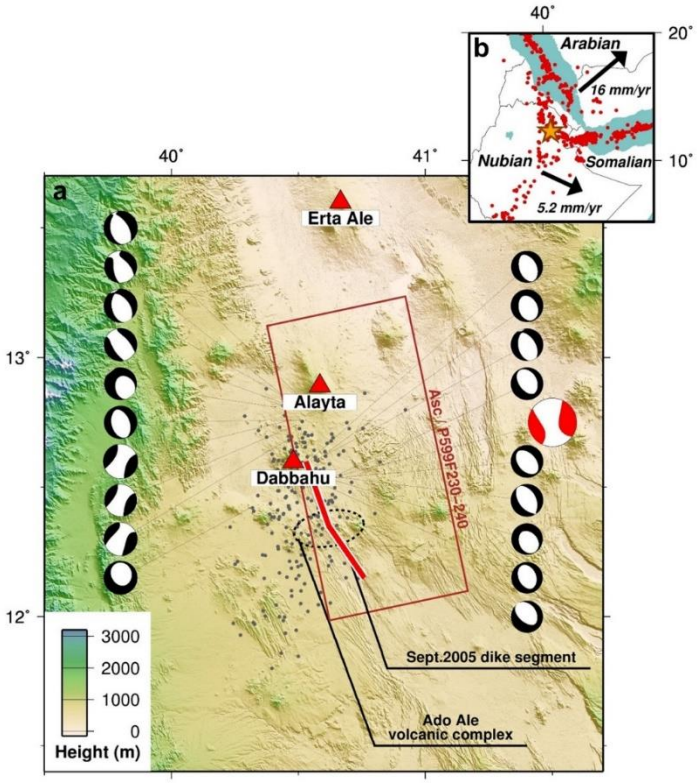


Figure 4-1. Study area in this chapter. a) Enlarged map, Grey dots are the location of epicenters during 2005-2010. Beachballs are focal mechanisms of each earthquake that are greater than M 4.9. Red one is focal mechanism of the mainshock during the episode (M 5.5, 24 September 2005). Red triangles indicate the location of active volcanoes around the study area. Red rectangular shows the PALSAR-1 footprint we processed in this chapter. The satellite flight direction is from SSE to NNW direction. The observation conducted right-looking geometry. b) Location map around the Afar basin. Red dots are the location of epicenters during 1960-2010. Star indicates the study area in this chapter. Black arrows represent direction of relative plate motion in a Nubian-fixed reference frame. The information of earthquake is derived from USGS catalog.

Some previous studies have presented 3D displacement fields associated with the rifting events since 2006 (Grandin et al., 2010; Hamling et al., 2014; Pagli et al., 2014). However, they were derived by interpolating the displacement data outside the graben floor into the data-missing graben floor. In other words, it is still uncertain if graben was simply subsiding without any horizontal

displacements. Meanwhile, Himematsu and Furuya (2015) reported significant rift-parallel block-like horizontal motion at the subsiding graben floor in the 2007 Natron rifting event by analyzing L-band PALSAR (Phased-Array type L-band Synthetic Aperture Radar) images acquired from the ALOS (Advanced Land Observation Satellite). Those displacements were explained by strike-slips on the two graben-bounding faults, which, to our knowledge, have never been reported in any previous rifting events. Very few strike components in seismological data and a gap of seismic and geodetic moment release suggested that these strike-slips were aseismic. No similar rift-parallel horizontal displacements were, however, reported in the 2005-2010 Afar rifting event, and it remains uncertain how frequent and universal such rift-parallel movements are. Here we reexamine the crustal

Table 4-1. Timing and volume of intruded magma during the 2005-2010 Afar dike intrusion sequence.

Event #	Date	Volume of magma intrusion [km^3]
1	September 2005	2.5
2	June 2006	0.12
3	July 2006	0.042
4	September 2006	0.088
5	December 2006	0.058
6	January 2007	0.037
7	August 2007	0.048
8	November 2007	0.15
9	March 2008	0.088
10	July 2008	0.066
11	October 2008	0.17
12	February 2009	0.077
13	June 2009	0.046
14	May 2010	0.08?

Date and volume of intruded magma in each event are acquired from Hamling at al. (2009) and Wright et al. (2012). The magma intruded volume during May 2010 event is not presented accurately.

deformation data acquired from PALSAR data to see if the rift-parallel movements were accompanied with the 2005-2010 Afar rifting events; the details on the PALSAR images are shown in Table 4-1.

Moreover, regarding the Afar dike intrusion episodes, no observation results based on PALSAR images have been reported so far. The advantage of L-band PALSAR over shorter wavelength data is its higher coherence even if the temporal separations are long, which allows us to monitor long-lasting displacements. To reduce phase decorrelation problem, we applied an intensity-based pixel tracking technique (Strozzi et al., 2002), which could provide us with robust data rather than InSAR.

Table 4-2. PALSAR-1 dataset in this chapter.

Data #	Acquisition date (dd.mm.yyyy)	B_perp [m]
1	12.06.2007	0
2	12.12.2007	778.2
3	29.04.2008	1420.8
4	14.09.2008	-498.3
5	15.12.2008	-387.8
6	02.08.2009	-140.3
7	17.09.2009	606.6
8	05.05.2010	602.6
9	20.06.2010	858.5
10	05.08.2010	264.1

Processed PALSAR data and each perpendicular baseline. Ten L-band radar images are obtained from ascending track (Path: 599, Frame: 230-240). Perpendicular baselines (B_perp) are in reference of Data #1. Image cover area is shown in Figure 4-1.

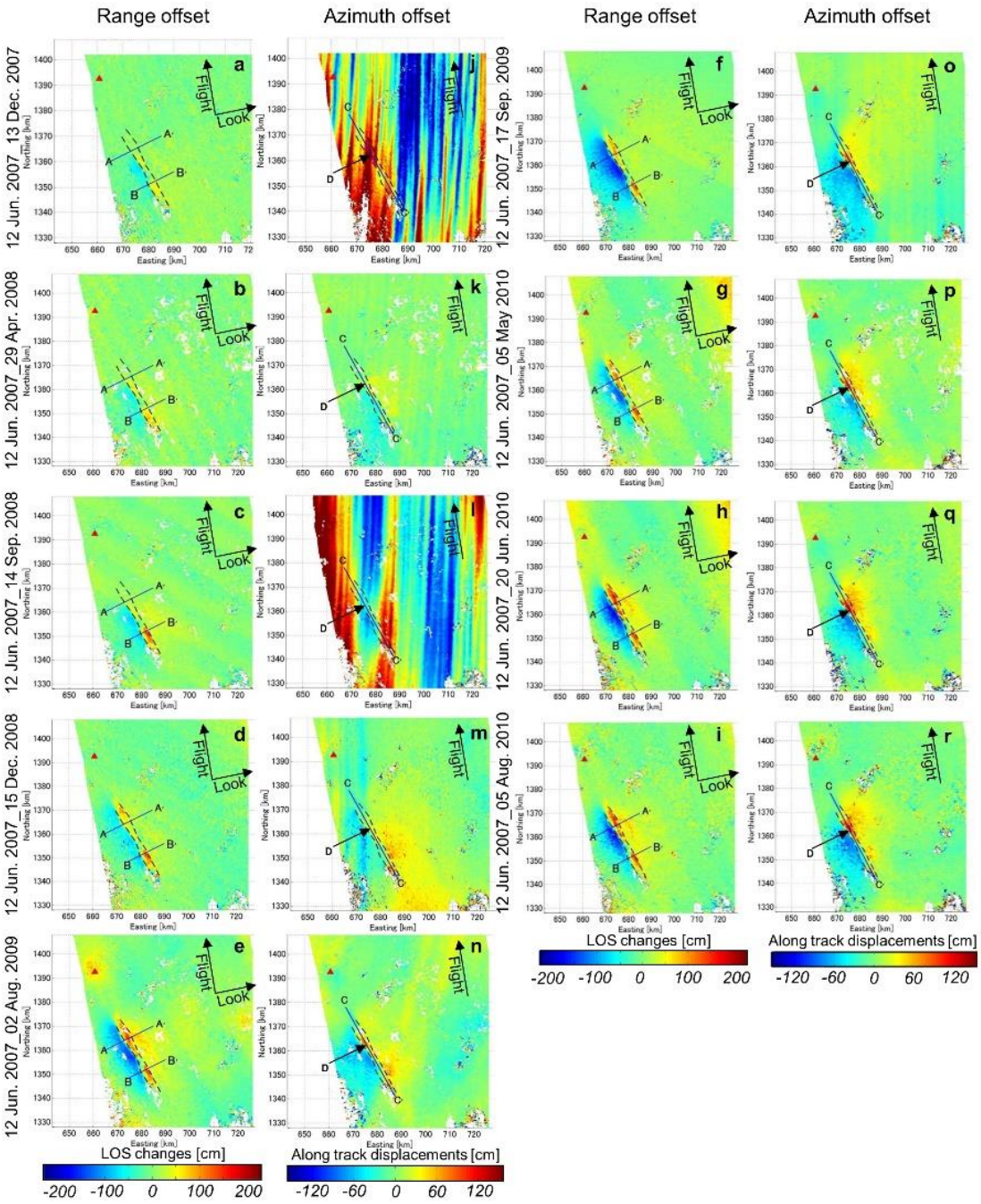


Figure 4-2. PALSAR -1 pixel-tracking data for the dike intrusion sequence in Afar. Cumulative range (a-i) and azimuth offset (j-r) from 12 June 2007. Cross sections of range offsets across north and south part of a graben (profiles A-A', B-B') are shown in Figures 4-4b and 4-4c. Cross sections of azimuth offsets along the graben floor (profile C-C') are shown in Figure 4-4d. Point D (Black arrow) shows a point which is a maximum positive signal in Figure 4-2r. Black dashed lines show top locations of two faults in our model.

4.2 SAR data and processing method

Pixel tracking technique can provide us with two independent displacement data sets that are sensitive not only to the line-of-sight direction (range offset) but also to the along-track direction (azimuth offset) (Jonsson et al., 2002; Kobayashi et al., 2009; Simons et al., 2002; Tobita et al., 2001). Our processed images were acquired from only ascending track and thus did not allow us to completely resolve the 3D displacements. However, the range and azimuth offset data in the present satellite track can well constrain the displacement field, because the satellite flight direction is nearly in parallel with the rift-axis, and the range and azimuth offsets are sensitive to such displacement that are perpendicular and parallel to the rift-axis, respectively. Highly coherence over longer temporal separation in the L-band SAR data is even more important and helpful to robustly constrain the displacements. Because ALOS/PALSAR was launched in January 2006 and the images became available since 2007 in this study area, we cannot quantify the surface displacements due to the earlier events in 2005-2006. For the PALSAR data processing, we used the commercial GAMMA software (Wegmüller & Werner, 1997). In performing pixel tracking technique, we set the search window size of 64×192 pixels for range and azimuth directions with sampling interval of 16×36 pixels. Artificial error due to the topography were reduced by using the 3 arc-second SRTM DEM (Shuttle Radar Topography Mission digital elevation model) (Farr et al., 2007).

While both the range and azimuth offset indicate that the displacements are distributed over the ~40 km-long graben structure (Figures 4-2 and 4-3), the azimuth offset shows positive signal (toward N349°E) greater than 1 m over the northern half of the graben floor, and no such positive signals can be observed outside the graben floor (Figures 4-2 and 4-3). Time-series of pixel tracking results are shown in Figure 4-2 and the details of the dataset are indicated in Table 4-2. Also, it is

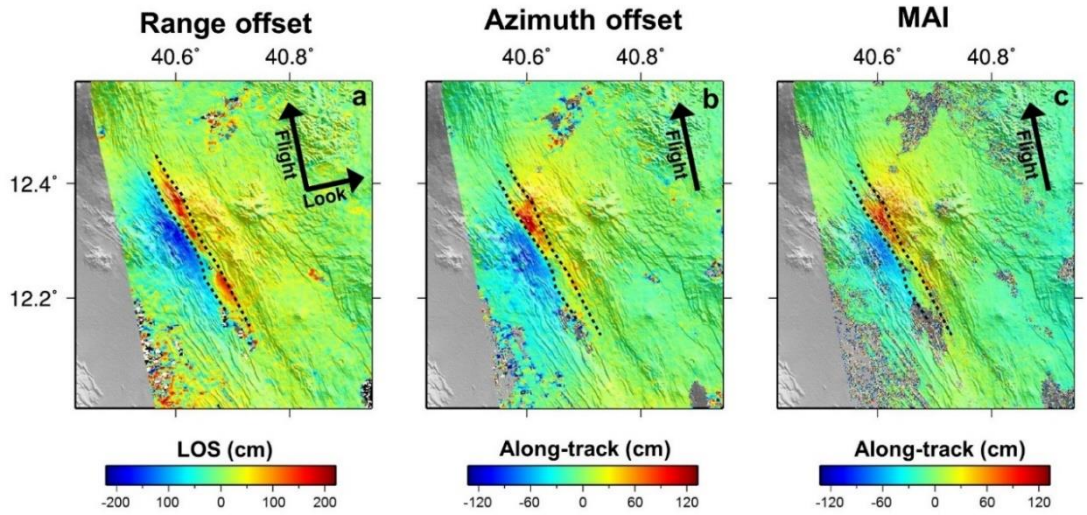


Figure 4-3. PALSAR-1 pixel tracking and MAI from 12 June 2007 to on 5 August 2010. (a) Range offset, (b) azimuth offset, and (c) MAI data. Positive signals indicate LOS lengthening in range offset and horizontal displacements along the satellite flight direction (NNW), respectively. Dotted lines traced signal discontinuities in the pixel tracking. Arrows indicate the direction of radar irradiation (Beam) and satellite flight direction (Flight), respectively.

important to note that the offset fields between the graben floor and the shoulders are clearly discontinuities. Namely, the graben floor moved along the satellite flight direction independently from both sides of the graben. Those positive signals in the azimuth offset implied that the rift-parallel horizontal movements did indeed occur as observed during the 2007 Natron event. We confirmed that multiple aperture interferometry (MAI) (Bechor & Zebker, 2006)), which is a phase-based method to detect horizontal displacements along the satellite tracks, also indicated the same signals as the azimuth offset data (Figure 4-3c). Thus, the rift-parallel horizontal displacements at the graben floor were indeed occurring at least since 2007. Given the presence of discontinuities in both the range and azimuth offsets across the boundaries between the graben floor and both sides, we can easily rule out a possibility that the rift-parallel motion could be caused by the volume changes of a magmatic source. We will further discuss the mechanisms of the movement in the following sections.

Casu and Manconi (2016) have shown short-baseline time-series of pixel tracking data, using C-band ENVISAT/ASAR dataset during the post-2005 rifting event. Although they did not insist on the rift-parallel motion at the graben floor, we can again clearly identify ~80 cm of northward rift-parallel movements in the displacement velocity from 2006 to 2010 (see Figure 6b in Casu & Manconi, 2016). Namely, the rift-parallel motion at the graben floor during the post-2005 rifting event was confirmed by both L-band and C-band data. Meanwhile, in view of the 3D displacement for the largest event in September 2005 shown by Wright et al. (2006) and Grandin et al. (2009), there appear few rift-parallel displacements.

In order to examine if there is any relationship between the rift-parallel movements and the intruded magma volume, we compared the temporal evolution of the azimuth offset data with the estimated volume of magma injection at each rifting event by Hamling et al. (2010) and Wright et al. (2012) (Figure 4-4a); our fault model shown later is derived from cumulative displacements. In view of each azimuth offset profile along the rift-parallel graben floor (Figure 4-4d), the temporal evolution of azimuth offset does not show clear correspondence to the timing of magma intrusion. However, there appears to be some lagged correlations with a delay time of ~6 months or more, which might be consistent with the absence of the rift-parallel motion during the first largest Event 1 if the rift-parallel motion took place with significant delay (Grandin et al., 2009; Wright et al., 2006).

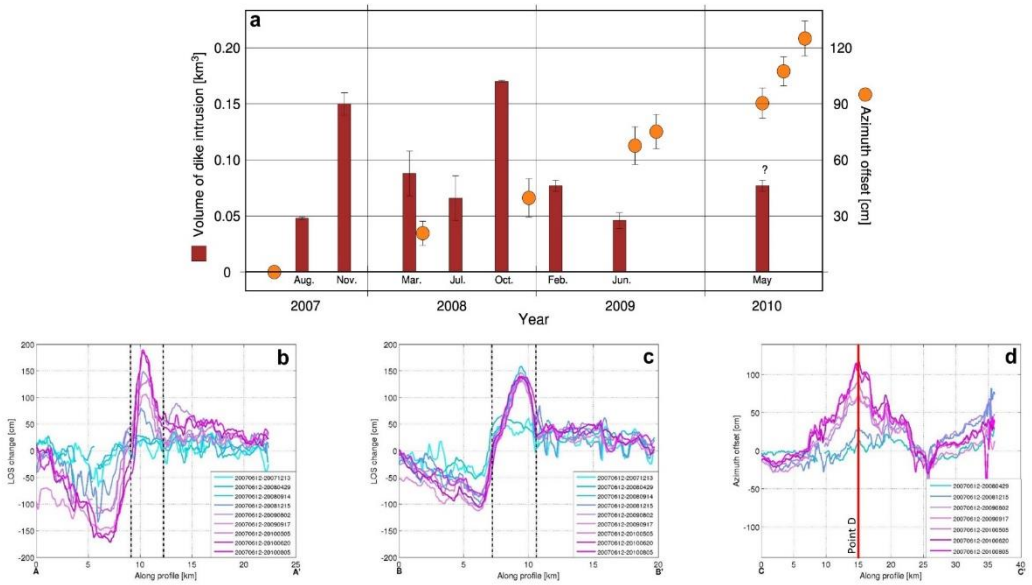


Figure 4-4. Temporal evolution of cumulative azimuth offset and its cross-sections of pixel tracking. (a) Volume of dike intrusion and temporal evolution of azimuth offset. Left-vertical axis shows volume of magma intrusion (Red bars) whose data are shown in Hamling et al. (2009) and Wright et al. (2012). Right-vertical axis shows azimuth offset (Orange circles) at a point that indicate the maximum positive signal at a graben floor (Point D). Vertical error bars represent the root-mean-squares at the non-displacement field in each of the results. (b-d) Temporal evolution of the range and azimuth offset along each cross-section in Figure 4-2. Black dashed lines are the location of the graben-bounding fault.

4.3 Fault source model

We have derived a fault slip distribution model in an elastic half space that can explain the cumulative displacements from June 2007 to August 2010 (Figure 4-5). We applied quad-tree method to reduce the number of the data (Figures 4-5a and 4-5d). The slip and tensile opening distribution model consist of two graben-bounding faults and a dike segment (Figures 4-5g-l), which were constructed by triangular dislocation elements (Furuya & Yasuda, 2011; Meade, 2007). A Poisson's ratio of 0.25 and a rigidity of 30 GPa were assumed. In deriving the slip and tensile opening on each segment, we constrained both the slip direction and the smoothness of the inferred slip and opening distributions (Furuya & Yasuda, 2011; Himematsu & Furuya, 2015). Standard deviations of each component were

derived by using iterative inversions with random noise (Wright et al., 2004) (Figure 4-6). The slip distributions revealed that the strike-slip mostly concentrated near the surface, whereas the peak of the strike-slip (1.1 m at maximum) is located at a depth of 2 km on the west-dipping fault. Cumulative geodetic moment release of the strike components alone turned out to be 1.61×10^{18} Nm (Mw = 6.07), while the total geodetic moment release, which includes both normal faulting and tensile opening, is 1.82×10^{19} Nm. It turns out that even the strike-slip contributions in the geodetic moment release alone were five times as great as the cumulative total seismic moment release (3.3×10^{17} Nm) during the observation period (Belachew et al., 2013). Considering that very few strike-slip earthquakes were detected by local seismic networks, the gap of those moment releases suggested that these strike-slips were aseismic. We checked that synthetic displacements could explain both observation results with root-mean-square (RMS) misfits of 12.9 cm and 7.0 cm for range and azimuth offset, respectively.

Some previous models derived from the ENVISAT/ASAR InSAR data showed ~2.5 m opening even during each individual event (Grandin, Socquet, Doin, et al., 2010; Ian J. Hamling et al., 2010). In contrast, our tensile opening is estimated to be 2.3 m even for the cumulative displacements, much smaller than previous estimates. We should keep in mind, however, that both Grandin et al. (2010a) and Hamling et al. (2010) did not include any fault segments but only tensile opening in their models, because the missing data over the graben floor did not let them to include the contribution by fault slip. On the other hand, other models by Ebinger et al. (2010) and Hamling et al. (2009) included not only tensile opening but also fault segments and provided us with the cumulative opening from 2005 to 2009 (Ebinger et al., 2010; Hamling et al., 2009). The accumulation diagram by Ebinger et al. (2010) indicates ~2.5 m cumulative opening along the southern part of the Manda-Hararo Dabbahu magmatic segment during 2007-2009, which is nearly consistent with our estimated opening distribution. We consider that such models including only dike segments will overestimate an opening

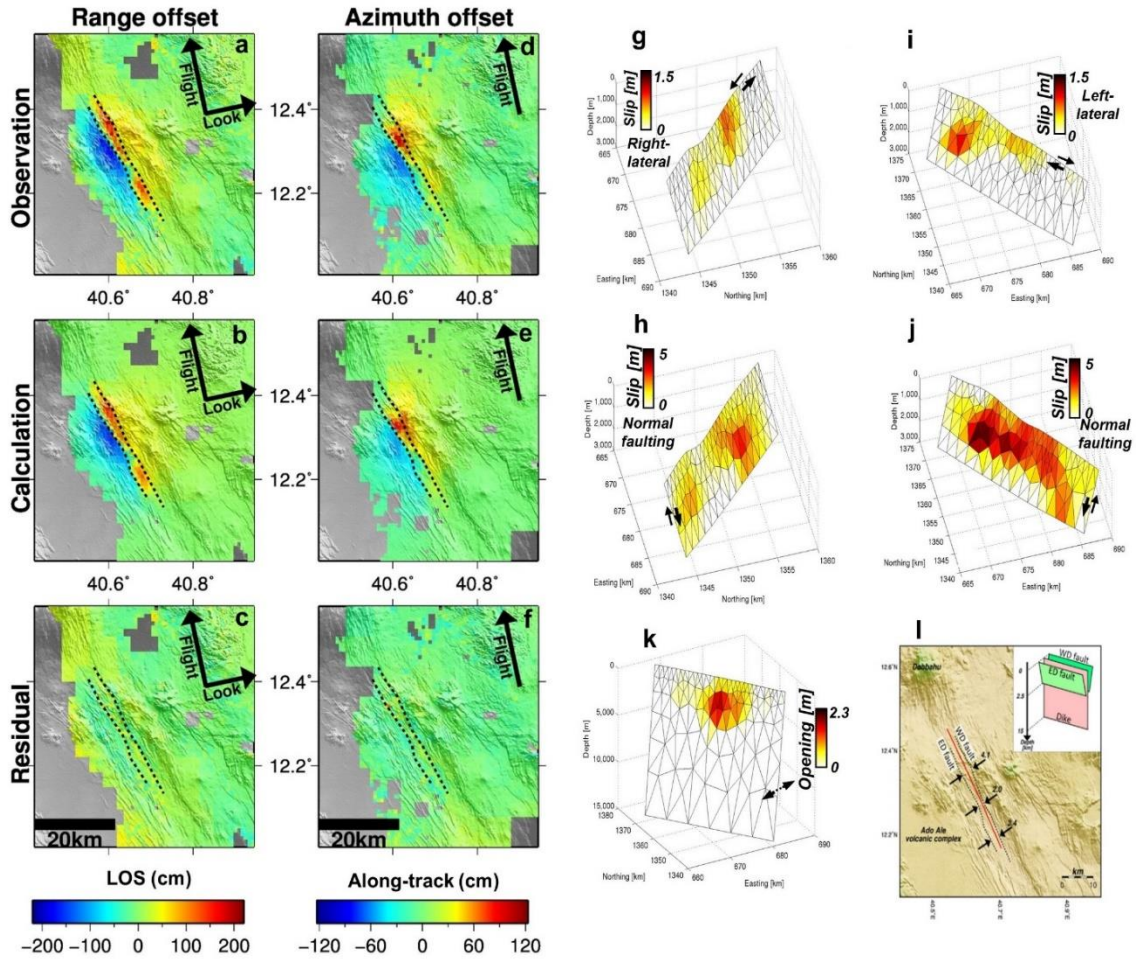


Figure 4-5. Our optimal elastic model for the PALSAR-1 pixel-tracking data. Range offset observation (a), calculation (b) and misfit residual (c). Azimuth offset observation (d), calculation (e) and misfit residual (f). Slip distributions on each fault segment. Left-lateral strike-slip (g) and normal slip (h) on the east-dipping fault. Right-lateral strike-slip (i) and normal slip (j) on the west-dipping fault. (k) Dike opening distribution. (l) Overview and geometry of the fault model. Black and red lines indicate top locations of the two faults and the dike segments, respectively. Numbers with black arrows are graben widths at each point. Inset shows schematic image of fault model geometry.

volume, probably the observed significant displacements were entirely attributed to the tensile opening despite the presence of displacements due to fault segments.

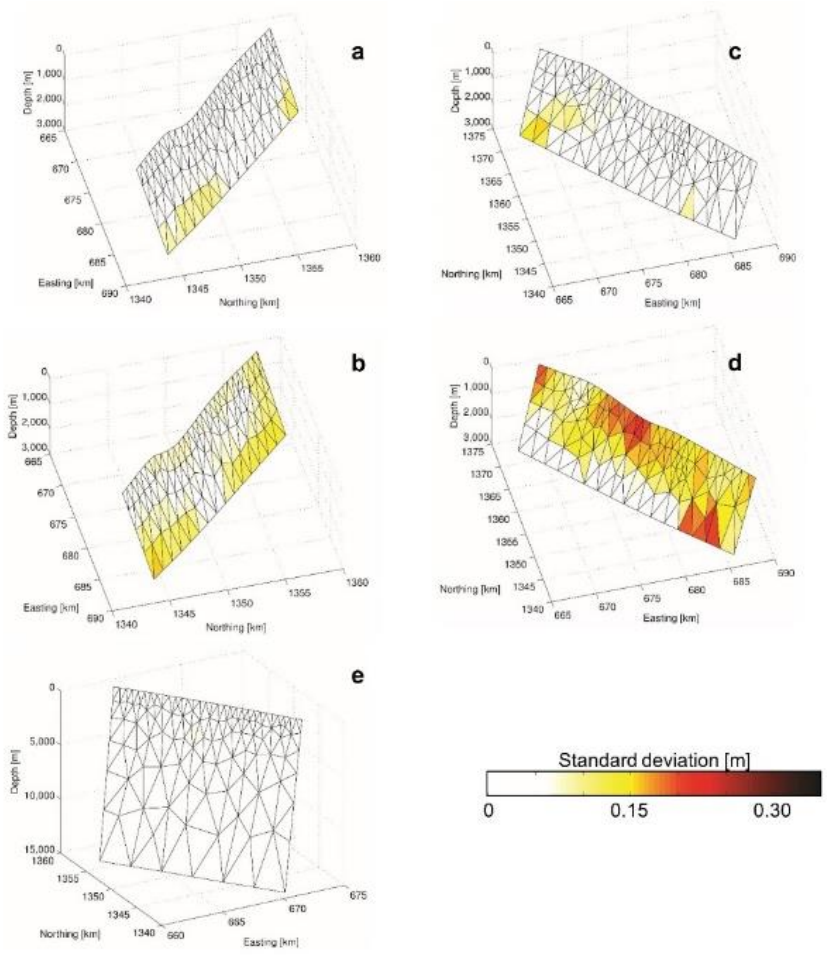


Figure 4-6. Standard deviations of faulting and opening distributions. Slip error was calculated by 200-times iterative inversion with random noise. Standard deviations of left-lateral strike-slip (a) and normal slip (b) on east-dipping fault, that of right-lateral strike-slip (c) and normal slip (d) on west-dipping fault, and that of dike opening (e).

We computed Coulomb stress changes (ΔCFF) caused by tensile opening upon the two graben-bounding faults in order to assess if the dike intrusion promoted the inferred fault slip (Figure 4-7) (King et al., 1994). Positive stress changes that correspond to unclamping are concentrating at shallower depths (0-1.5 km) on each receiver fault. The distributions of positive stress changes are consistent with the inferred strike-slip distributions, but a peak of strike-slip located at a depth of 2 km where slight negative stress changes were indicated. Thus, the stress changes due to dike opening did

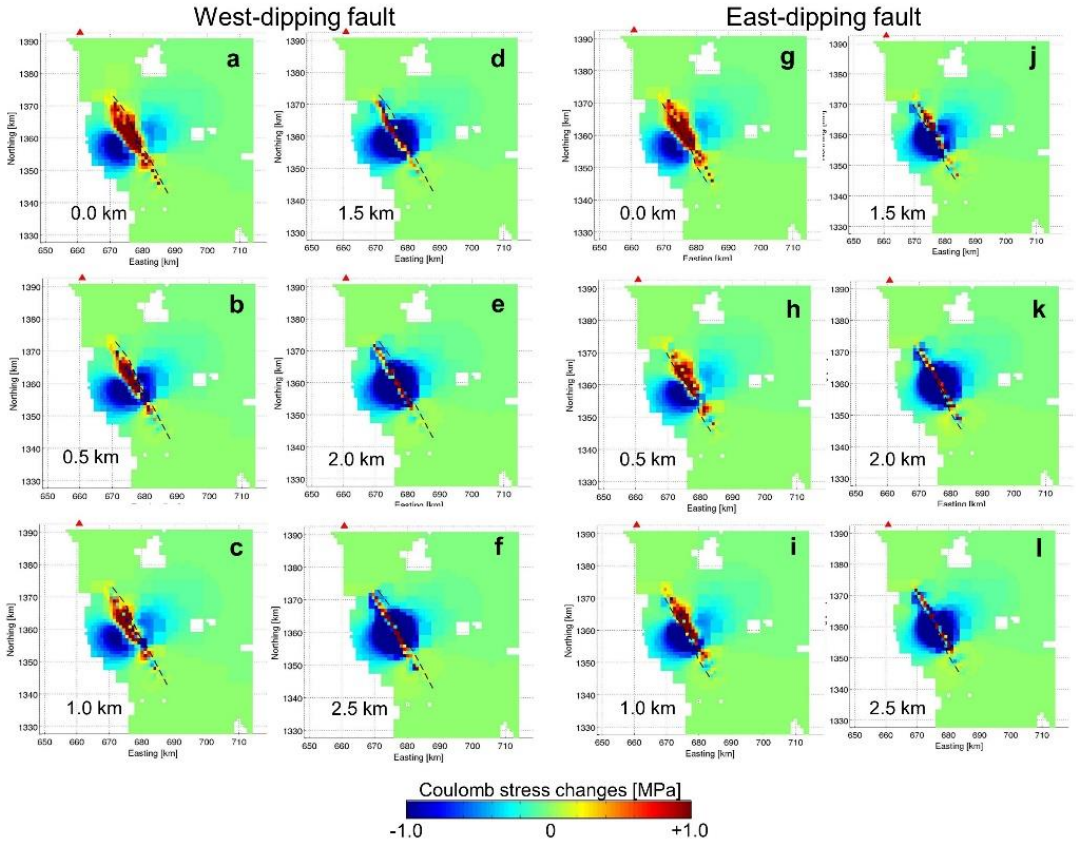


Figure 4-7. Coulomb stress changes due to dike opening in our model for each receiver fault. Horizontal slices of stress changes associated with dike opening inferred from our model on west-dipping fault (a-f) and east-dipping fault (g-l). Depths of slice are shown at bottom-left corner of each panel. Positive stress changes indicate promoting fault slip on receiver fault. Black dashed lines show top locations of each receiver fault. Red triangles located at the Dabbahu volcano.

not prevent the aseismic strike-slip in the shallower part, but the stress changes were unlikely to be a driver of the rift-parallel motion.

4.4 Discussion

4.4.1 Aseismic slip consistent with rate-and-state friction law

Our pixel tracking data and the fault model indicate that the observed displacements are mostly caused by aseismic processes, because cumulative seismic moment release can only explain less than 2% of the geodetic moment release. Aseismic slip plays a role in strain accommodation during rifting events

(Calais et al., 2008), and can be one of the key drivers for earthquake swarms at volcanic or geothermal area including divergent plate boundaries (Lohman & McGuire, 2007; Vidale & Shearer, 2006; Wicks et al., 2011). According to the rate-and-state dependent friction law, aseismic slip tends to occur at shallower depths of crust, in which stable slip tends to take place (Dieterich, 1979; Ruina, 1983; Toda & Stein, 2002). The slip tendency is consistent with our slip distribution estimates, which indicate the strike-slip patches are mostly located at shallower depths than the normal faulting patches (Figure 4-5).

4.4.2 Any relevance to strike-slip earthquakes along divergent plate boundaries?

Even divergent plate boundaries under an extending stress regime include potential for causing strike-slip earthquakes. Most accepted mechanisms of strike-slip earthquakes under extensive stress regime are bookshelf faulting (Green et al., 2014; Mandl, 1987; Tapponnier & Courtillot, 1990) and dog-bone seismicity (Toda et al., 2002). The observed rift-parallel displacements, however, look like block-like uniform movement of the graben floor and cannot be explained by either bookshelf faulting or dog-bone seismicity even if those mechanisms worked by aseismic processes.

4.4.3 Block-like motion of graben floor as a response to horizontal flow of plume material?

The elastic fault model can successfully explain the rift-parallel block motion but does not clearly tell the dynamical mechanisms. We may interpret that the rift-parallel block-like motion of the graben floor would represent the passive advection of the upper crust that is coupled with the horizontally underlying flow of sill; the sill would be deeper than 5 km in light of the depth tensile opening (Figure 4-5). Although sill intrusion has been incorporated as a horizontally lying mass to reproduce uplift signals (Fialko et al., 2001), we do not observe any uplift signals but horizontal movements that were kinematically explained by shallow aseismic strike-slip in our model. In the framework of elastic modeling, however, we can no longer express the effects of flowing sill that can

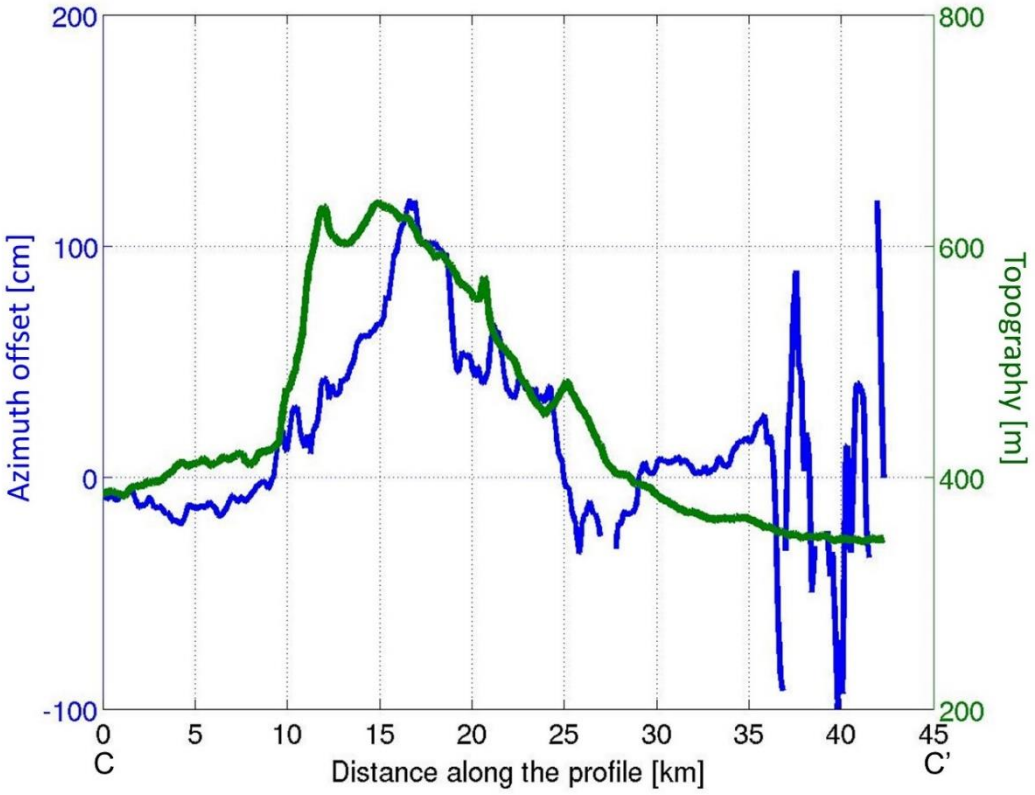


Figure 4-8. Cross sections of topographic height and cumulative azimuth offset from 12 June 2007 to 5 August 2010 along the profile C-C' in Figure 4-2. Green and blue lines indicate topographic height and azimuth offset from 12 June 2007 to 5 August 2010 along the C-C', respectively.

viscously couple with the overlying crust. Meanwhile, in a recent thermo-rheological geodynamic model that aims to reproduce the presence of both active and passive rift zones around the Tanzanian craton in central East African Rift (EAR) (Koptev et al., 2015), similar rift-parallel displacements have been demonstrated during the dynamic topographic evolution. Although there are significant gaps in terms of both spatial- and temporal-resolutions between the thermo-rheological geodynamics model and our geodetic observations, and the model does not yet reproduce the episodic processes such as rifting, the simulated rift-parallel displacements could be essentially what we observed geodetically. A key simulated process relevant to the geodetic observations could be a channelized flow of plume material, which is a deflection of the plume head at the cratonic keel (Albers & Christensen, 2001;

Sleep, 1997). The lateral channelized plume flow can generate narrow strain localizations and induce slow surface movements along rift axes (Koptev et al., 2015). Around Lake Natron in the simulation results, the surface velocity indicated southward horizontal movements on the order of a few millimeters per year, which is consistent with a direction of the rift-parallel displacements in the 2007 Natron rifting episode (Himematsu & Furuya, 2015).

A seismic tomography results showed low velocity zones at the southern edge of Afar, where we may expect the upwelling mantle plume (Bastow et al., 2008). A Moho depth distribution along the western-edge of Afar also indicates that crustal thickness becomes thinner toward NNW (Hammond et al., 2011). If the plume material flows along the rift axis in the western Afar, the plume material would form a channel toward NNW. The direction is also consistent with the rift-parallel movements over the graben floor in Afar. Assuming that the plume channeling causes along-axis surface velocity on the order of a few millimeter per year as in the numerical model over the central EAR, the amplitude of the rift-paralleled displacements (~1 m) in Afar is largely consistent with the strain accumulated from an interval of rifting cycle (~400 years) (Ebinger et al., 2010; Grandin et al., 2010a) and the surface velocity. We may thus interpret the rift-parallel displacements in both Natron and Afar as caused by the channelized flow that would be also responsible for dike intrusion. In other words, rift-parallel block-like motion of graben floor might be absent under magma-poor passive rifting.

Chapter 5

Icecap and Crustal Deformation Associated with the 2014-2015 Bárðarbunga Dike Intrusion Episode Inferred from SAR Pixel Tracking

Some contents in this chapter are preparing to submit to *Journal of Geophysical Research: Solid Earth*

Himematsu, Y., F. Sigmundsson, M. Furuya (2018) Icecap and crustal deformation associated with the 2014 Bárðarbunga dike intrusion episode inferred from SAR pixel tracking, *In preparation*.

Chapter 5. Icecap and crustal deformation associated with the 2014-2015 Bárðarbunga dike intrusion episode inferred from SAR pixel tracking

5.1 Introduction

Iceland is a subaerial part of the divergent plate boundary between the North American plate and the Eurasian plate with a spreading rate of 18-19 mm/yr in the N100-105°E direction (e.g., DeMets et al., 2010). Combination of both an oceanic spreading ridge and a mantle plume beneath the central Iceland leads to the formation of the complex divergent plate boundary (Figure 5-1). The divergent plate boundary in Iceland consists of several volcanic systems, some of which are covered with glaciers or icecaps. The Vatnajökull icecap, the largest icecap in Europe, covers some of the most active volcanic systems in central Iceland (Figure 5-1). Subglacial volcanic eruptions may induce lahars and floods due to ice melting as heat transfers from magma, that is known as "jökulhlaup" (Björnsson, 2003; Gudmundsson et al., 1997). Such jökulhlaups are one of the primary volcanic hazards in Iceland.

The central volcano of the Bárðarbunga volcanic system is one of the subglacial volcanoes under the Vatnajökull icecap, with a 10 km diameter caldera (Figure 5-1). In 2014-2015, a major dike intrusion episode occurred in the volcanic system. Seismicity propagated away from the Bárðarbunga caldera and a fissure eruption occurred at Holuhraun, 10 km north of the margin of the Vatnajökull icecap (Figure 5-1). Rectilinear propagation of seismicity and the fissure eruption suggested a migration of magma (dike) from a source beneath the Bárðarbunga caldera (Sigmundsson et al., 2015). The magma passed through pre-existing fractures which were formed during previous eruption episodes (Gudmundsson et al., 2016; Hjartardóttir et al., 2015; Pedersen et al., 2017; Ruch et al., 2016). Both

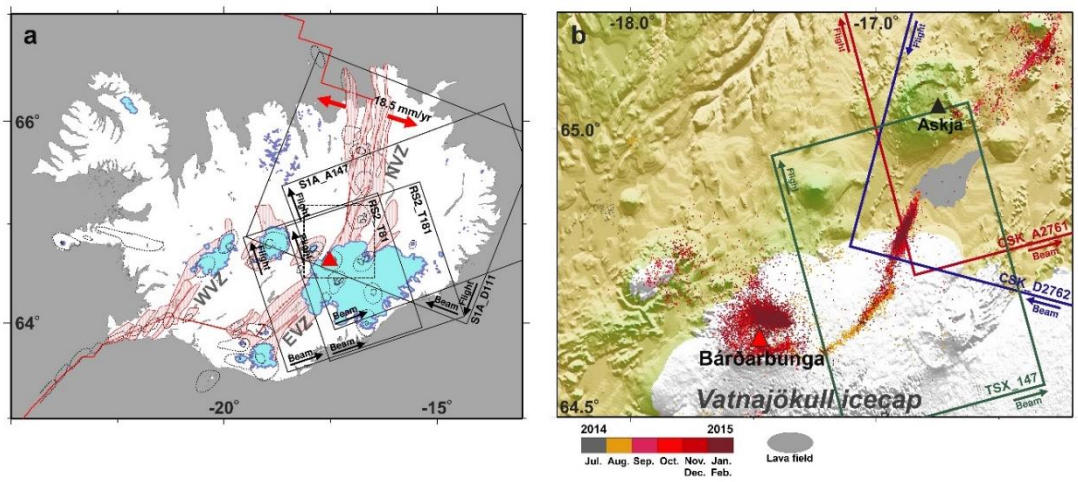


Figure 5-1. (a) Map showing the volcanic systems (dashed lines), calderas (combed lines), and associated fissure swarms (red transparent) in Iceland. Dashed box shows a region of Figure 5-1b. RADARSAT-2 (RS2) footprints are shown as solid black boxes. Outline data of glaciers or icecaps (light blue) is from the Randolph Glacier Inventory version 6.0 (GRI consortium, 2017). (b) Colored dots locate hypocenter locations from July 2014 to February 2015 (source, Icelandic Meteorological Office database, "http://hraun.vedur.is/ja/viku/", last accessed on 17 October 2017). Footprints of Cosmo-SkyMed (CSK) and TerraSAR (TSX) images are shown as colored boxes. Each direction of satellite flight ("Flight") and looking ("Beam") are shown as arrows. Gray region marks the 2014-2015 lava field outline traced by comparing back scatter intensity between two CSK images which acquired before and after the episode (28 July 2014 - 6 March 2015 on Track D2762).

numerical and analog models suggested that variation in regional strain and gravitational potential due to topographic and ice mass load strongly contributed to the lateral magma propagation (Heimisson et al., 2015; Sigmundsson et al., 2015; Urbani et al., 2017). The main Holuhraun fissure eruption began on 29 August 2014 at the northern end of seismic propagation. The eruption continued until February 2015 and generated 84 km^2 lava field at the Holuhraun plain (Hjartardóttir et al., 2015; Pedersen et al., 2017; Sigmundsson et al., 2015). Overview flight observation reported that a minor eruption occurred between the main eruption site and the icecap edge on 5-7 September 2014 (Hjartardóttir et al., 2015).

Previous geodetic studies in the area have reported ground displacements associated with the dike intrusion. Satellite radar interferograms and GPS measurements revealed the displacements in WNW-ESE direction at north of the Vatnajökull icecap, which were caused by the dike intrusion as well as the evolution of the collapse of the subglacial Bárðarbunga caldera (Parks et al., 2017; Riel et al., 2015; Ruch et al., 2016; Sigmundsson et al., 2015). The direction of horizontal displacements is nearly consistent with that of far-field tectonic stress. However, as the focal mechanisms indicated, the observational data require some shearing along the dike (Ágústsdóttir et al., 2016; Parks et al., 2017; Ruch et al., 2016; Sigmundsson et al., 2015).

Ruch et al. (2016) applied SAR pixel tracking technique, and showed temporal evolution of the graben region, where conventional InSAR could not be used to detect the signal. Based on such data, Ruch et al. (2016) proposed that the evolution of graben formation almost ceased as of 6 September 2014, whereas the fissure eruption still continued. Ruch et al. (2016) did not use those signals over the icecap for their inversion model. Over the northernmost part of the dike outside the icecap, their inversion model indicated 4.5 m of opening and 1 m of left-lateral shearing across the dike. They proposed that both the opening and the shearing indicated the cumulative strain accommodation of oblique opening since a previous rifting episode in 1797. The digital elevation model (DEM) differences before and after the episode showed graben subsidence not only over the non-ice region but also above the icecap, indicating subglacial graben formation (Dirscherl & Rossi, 2018; Rossi et al., 2016). Airborne altimetry observations revealed up to 65 m of cumulative subsidence at the Bárðarbunga caldera due to the deflation of sill-like magma source and ring-faulting around along a caldera boundary (Gudmundsson et al., 2016). Although some interferograms with short-temporal baseline could detect icecap subsidence due to the caldera collapse, these data could not reveal signals on icecap surface above the dike (Riel et al., 2015). After the fissure eruption ceased

on February 2015, moderate-scale earthquakes (M>4) have been observed along the Bárðarbunga caldera even by now, suggesting ongoing caldera uplift due to pressure increase, either renewed magma accumulation or viscoelastic relaxation (Sigmundsson et al., 2018).

Although direct evidence of a subglacial volcanic eruption has not been reported so far, the magma may have been implied to approach the bedrock surface. Observations on a seismic array show pre-eruptive tremor at depth shallower than 3 km, suggesting magma reaching close to the bedrock surface (Eibl et al., 2016). An airborne altimetry study detected three circle-like ice sink holes (ice cauldrons) along the dike path before the fissure eruption (Reynolds et al., 2017; Sigmundsson et al., 2015). The volume of ice cauldron is up to 18 million m3. A numerical model demonstrates that formation of at least one of the ice cauldrons required magma penetration into the ice (Reynolds et al., 2017). Chemical compositions in river water discharged from the icecap during and after the eruption show notable changes, suggesting subglacial eruptions before the Holuhraun eruption (Galeczka et al., 2016). Despite the indications of subglacial eruptions, no jökulhlaup has been reported. Stored subglacial meltwater would contribute to promote a hydraulic-driven speed-up of glacier flow speed due to decreasing friction between ice and bedrock (e.g., Iken & Bindschadler, 1986). At Vatnajökull, for example, meltwater derived from a discharging subglacial lake water facilitated an acceleration of basal sliding at the bottom of glacier as observed by InSAR in 1995-1996 (Magnússon et al., 2007).

The aims of this chapter are to infer subglacial crustal deformation associated with the 2014-2015 Bárðarbunga dike intrusion episode, and to evaluate the advantage of pixel tracking approach for mapping subglacial crustal deformation. To our knowledge, few studies have reported subglacial crustal deformations associated with the subglacial dike intrusion due to InSAR

decorrelation problems at ice surfaces. To achieve these aims, we employ primarily the satellite SAR pixel tracking data to infer the subglacial crustal deformation.

5.2 SAR data and processing method

5.2.1 Processing method and SAR dataset

Satellite synthetic aperture radar (SAR) is one of the remote sensing techniques to observe the Earth's surface characteristics in the form of back-scatter intensity and reflected microwave phase. The phase difference between two SAR images allow us to map the surface movement with high spatial resolution between data acquisition interval (Interferometric SAR; InSAR). The cross-correlation-based pixel tracking approach can detect surface movement as a local residual of image coregistration using SAR amplitude (Michel et al., 1999; Strozzi et al., 2002; Wright et al., 2006). The pixel tracking identifies local residuals within an arbitral window size (64-256 pixels) after two SAR images are precisely coregistared. The spatial resolution of pixel tracking is controlled by the window size. The approach is suitable for detecting meter-scale surface movement, such as glacier flow or large-scale crustal deformation e.g. associated with dike intrusion. Measurement error of the pixel tracking approach depends on the accuracy of image coregistration. Although we coregister two images with an accuracy of 1/10-1/20 pixels, some factors such as changing surface characteristics due to covering/melting snow on the icecaps cause decorrelation problems. Standard deviation of pixel trackings at stable regions can be regarded as a measurement of the accuracy (Kobayashi et al., 2009).

The window size and sampling interval for each dataset in this chapter are described in Appendix A. We discarded the cross-correlation of below 0.05 as missing data. We corrected for stereoscopic effect, an artificial elevation-dependent offset, in pixel tracking results (Kobayashi et al., 2009) using a digital elevation model from the advanced spaceborne thermal emission and reflection

radiometer (ASTER) satellite mission. All SAR data were processed by using GAMMA software package (Wegmüller & Werner, 1997).

We applied the pixel tracking approach to X-band COSMO-Skymed (CSK), TerraSAR-X (TSX), and C-band RADARSAT-2 data (RS2) for detecting both icecap surface change and crustal deformation due to the subglacial dike intrusion in 2014. We also analyzed C-band Sentinel-1A (S1A) data to identify the temporal evolution of icecap surface changes during the 2014-2016 period (Appendix A). Spatial resolution of CSK and TSX data is 1-2 m, while the spatial resolution of RS2 data is 4-5 m (Appendix A). Spatial coverage of CSK and TSX images is, however, smaller than that of RS2 data (Figure 1). In this chapter, we refer to the period of 16 August-6 September 2014 as a co-diking period. Although the fissure eruption and the caldera collapse were continuing after the observation period, the crustal deformation associated with the dike intrusion mostly ceased when the dike propagation path had been formed (e.g., Ruch et al., 2016). Glacial isostatic adjustment (GIA) around the northernmost part of Vatnajökull icecap does not influence our measurements significantly and can be ignored, because GIA signal is less than 2-4 cm/yr for both horizontal and vertical components (Drouin et al., 2017).

Table 5-1. SAR dataset in this chapter and scale factors for correction of icecap signal

Satellite [a]	Orbit [Track] [b]	Date [c]	Data acquisition interval [Days] [d]	Scale factor [Days] [e]	Result [f]
Cosmo-SkyMed	Ascending [2761]	30 Jul. 2014 12 Sep. 2014	44	22	Figure 5-2
	Descending [2762]	13 Aug. 2014 23 Sep. 2014	41	44	Figure 5-2
TerraSAR-X	Ascending [147]	26 Jul. 2012 4 Sep. 2014 20 Nov. 2014	-	-	Figure 5-4
RADARSAT-2	Ascending [81]	1 Aug. 2014 18 Sep. 2014	48	35	Figure 5-6
	Ascending [181]	8 Aug. 2014 1 Sep. 2014	24	18	Figure 5-6

a Name of SAR satellite.

b Satellite flight direction. Ascending and descending means flight from SSE to NNW, and NNE to SSW, respectively.

c Date of observation of master and slave images.

d Intervals between data acquisition between master and slave images.

e Scale factor to correct the icecap signal in the co-diking signal. See section 5.2.4.

f Showing where we can see the result.

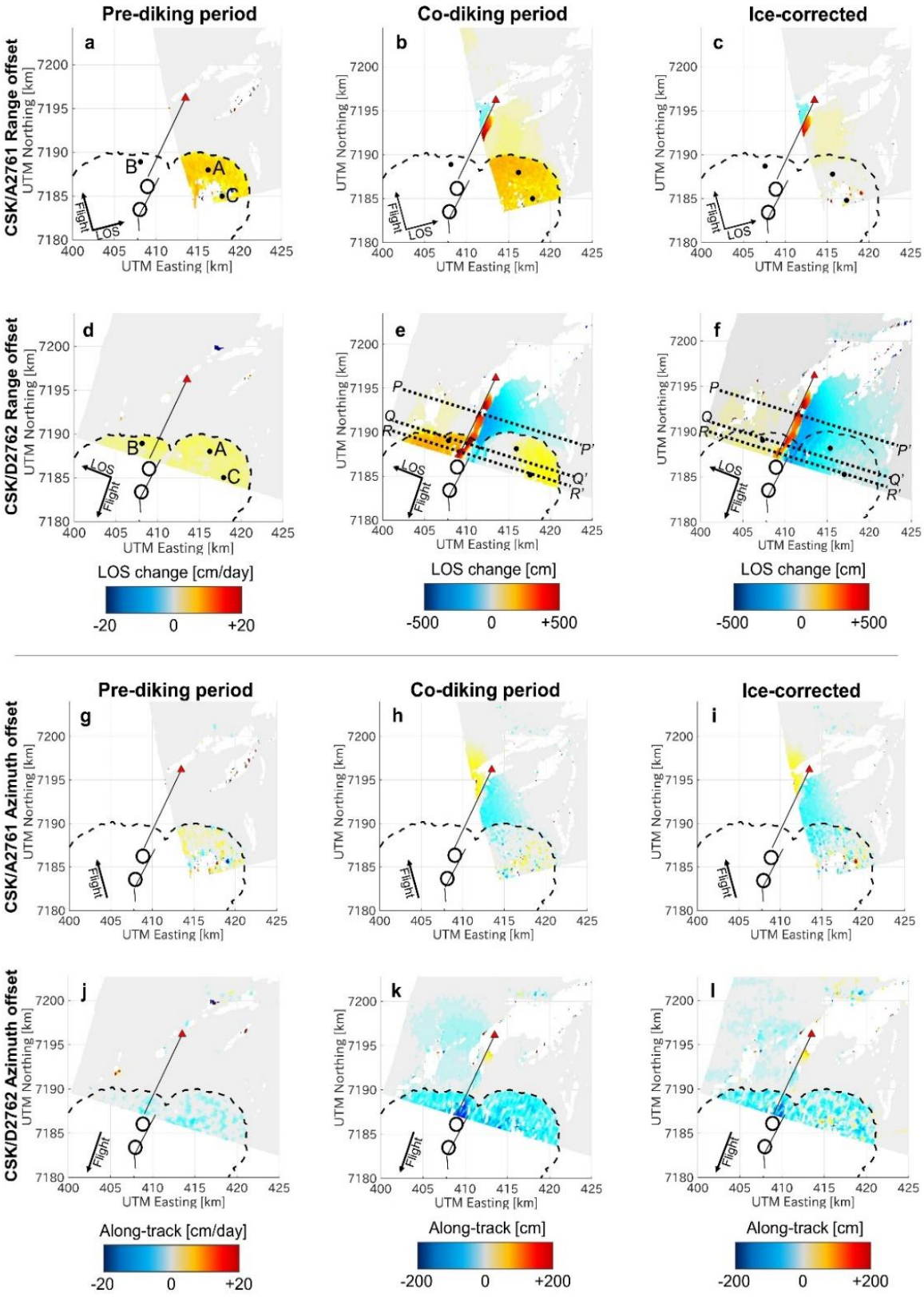

Pre-diking period
Co-diking period
Ice-corrected
CSK/A2761 Range offset
CSK/D2762 Range offset
CSK/A2761 Azimuth offset
CSK/D2762 Azimuth offset
a
b
c
d
e
f
g
h
i
j
k
l
A
B
C
P
Q
R
P'
Q'
R'
Flight
LOS
UTM Northing [km]
UTM Easting [km]
7180
7185
7190
7195
7200
400
405
410
415
420
425
LOS change [cm/day]
-20
0
+20
LOS change [cm]
-500
0
+500
Along-track [cm/day]
-20
0
+20
Along-track [cm]
-200
0
+200

Figure 5-2. Pre- and co-diking Cosmo-SkyMed (CSK) pixel tracking results and ice-corrected signal. CSK range offset (line-of-sight: LOS) from ascending track (a-c, pre-diking: 28 June-30 July 2014, co-diking: 30 July-12 September 2014, ice-corrected) and descending track (d-f, pre-diking: 28 July-12 August 2014, co-diking: 12 August-23 September 2014, ice-corrected). CSK azimuth offset (along-track) from ascending track (g-i) and descending track (j-l), respectively. Dashed lines trace outline of the icecap. Solid black lines and circles are the locations of dike segments and ice cauldrons after Sigmundsson et al. (2015), respectively. Dotted lines show the profiles P-P', Q-Q', and R-R' displayed in Figure 5-7. Positive signal for azimuth and range offset indicates horizontal displacement toward satellite flight direction and line-of-sight change away from satellite, respectively. Red triangle denotes the Holuhraun main eruption site during the episode. Black dots are selected points of time series of ice surface change in Figure 5-9. Black dots with capital letters (A-C) locate observation points for time-series of icecap surface changes (Figure 5-9). Coordinates are in UTM zone N28.

5.2.2 Observation result during pre- and co-diking period

CSK pixel trackings during the pre-diking period reveal the steady-state of ice surface movement and no significant changes outside the icecap (Figures 5-2a, 5-2d, 5-2g and j, Table 5-1). CSK pre-diking range offset from both ascending and descending show positive signals on the icecap (Figures 5-2a and 5-2d). Positive line-of-sight (LOS) changes observed from both ascending and descending tracks indicate downward movement, possibly implying ice thinning. Rate of the LOS change on the icecap is about 15 cm/day in the ascending track and 5 cm/day in the descending track, respectively. Azimuth offsets during the pre-diking period indicate northward horizontal movement of the icecap because azimuth offsets are insensitive to vertical displacement and represent only the horizontal displacements along the satellite flight direction (Figures 5-2g and 5-2j). Both azimuth offsets show less than 5 cm/day on the icecap without any significant displacements at ice-free region except for decorrelation noise. The northward icecap movement can be explained by gravity-driven ice flow along topographic gradient at the region (Bjornsson & Einarsson, 1990). Using both range and azimuth offsets from ascending and descending track, we retrieved a three-dimensional (3D) movement field of the steady-state ice flow by solving over-determined least-square problem because the unit vector of displacement are independent (Tobita et al., 2001). Pre-diking 3D displacement

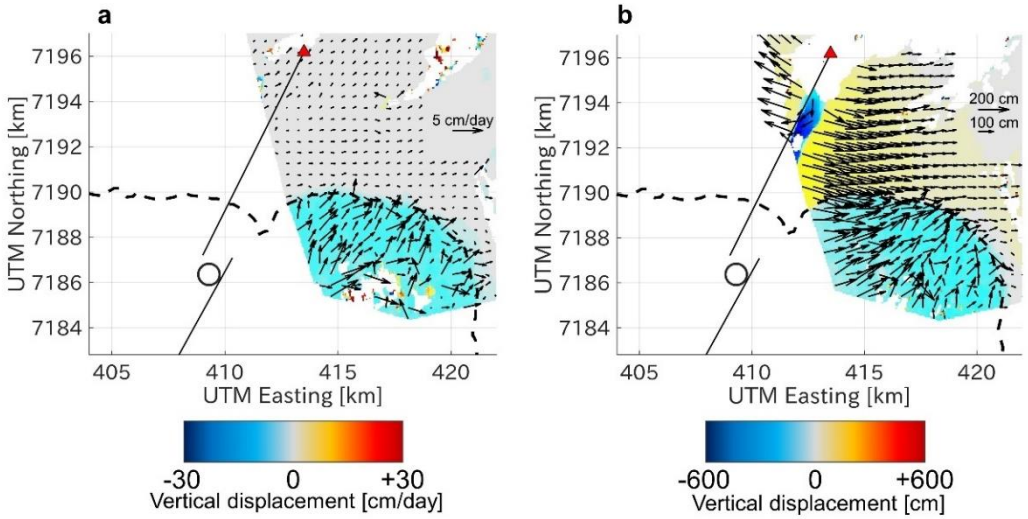


Figure 5-3. Pre-diking and co-diking 3D displacements inferred from CSK data. (a) Inferred pre-diking three-dimensional (3D) displacement rate. (b) Cumulative co-diking 3D displacement. Both are retrieved from Cosmo-SkyMed (CSK) range and azimuth offset from ascending and descending tracks. Arrows show the direction and amount of horizontal movement. Note that scales of horizontal movement are shown at the right-top in each result. Note that each color scales are different from each other. Dashed lines trace outline of the icecap. Solid black lines and circles are the locations of dike segments and ice cauldrons after Sigmundsson et al. (2015), respectively. Red triangle denotes the Holuhraun main eruption site during the episode. Coordinates are in UTM zone N28.

shows NNE horizontal movement (less than 5 cm/day) with downward movement (~20 cm/day) on the icecap during the observational period (Figure 5-3a).

Figures 5-2b and 5-2e show CSK range offset during the co-diking period. We regard a pair of 30 July 2014 – 12 September 2014 from ascending track and that of 12 August 2014 – 23 September 2014 from descending track as cumulative offsets during the co-diking period (Table 5-1). The pixel tracking data show signals of crustal deformation outside the icecap and icecap surface movement. The range offsets at ice-free region indicate graben formation associated with the dike intrusion as previous studies have already reported (Ruch et al., 2016). Positive signals along the dike indicate the subsidence; maximum positive offset is 5 m in CSK descending range offset (Figure 5-2e). We

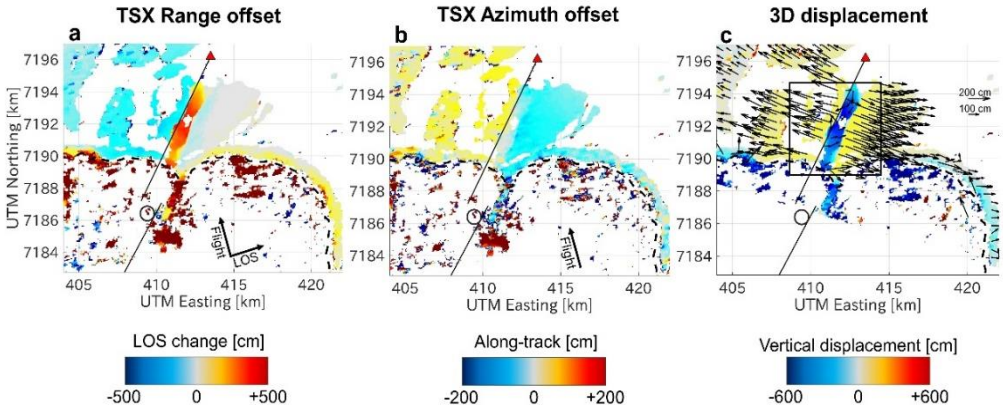


Figure 5-4. Stacked TerraSAR-X (TSX) pixel tracking and co-diking 3D displacement inferred from CSK and TSX dataset. Stacked TerraSAR-X (TSX) range offset (a) and azimuth offset (b) of 27 July 2012-4 September 2014 and 4 September 2014-20 November 2014. (c) Cumulative co-diking 3D displacement inferred from TSX ascending and CSK descending data. Black box shows the region of Figure 5-5a. Arrows show the direction and amount of horizontal movement. Scale of horizontal movement are shown at the right-top in the result. Dashed lines trace outline of the icecap. Solid black lines and circles are the locations of dike segments and ice cauldrons after Sigmundsson et al. (2015), respectively. Red triangle denotes the Holuhraun main eruption site during the episode. Coordinates are in UTM zone N28.

identified the maximum subsidence at ice-free region near the minor eruption site along the graben subsidence (Figure 5-5). CSK descending range offset reveals less than 50 cm at western half of graben flank and 1.5 m of negative signal at eastern half of graben flank (Figure 5-2e).

While the pre-diking range offset reveal only positive signal on the icecap (Figures 5-2a and 5-2d), the CSK co-diking range offset from descending track show negative signal on the icecap near the graben (Figure 5-2e). Negative signals of LOS change from right-looking descending track indicate eastward displacement and/or uplift. Thus, these negative signals imply icecap surface changes associated with subglacial crustal deformation. The descending range offset also indicates graben subsidence under the icecap because positive signal with signal discontinuities is detected even on the icecap. By contrast, we cannot find any signal variations across the icecap in the CSK co-diking

ascending range offset (Figure 5-2b).

The co-diking ascending azimuth offset shows about 1m of symmetric signal at the graben flanks (Figure 5-2h). Although there are little signal above the icecap, we find a clear offset discontinuity along the icecap edge. The co-diking descending azimuth offset shows very little signal at the graben flanks, because the observations are sensitive to displacements nearly parallel to the graben (Figure 5-2k). At the graben floor, we can identify ~1 m of positive offset at the northern half of graben subsidence and ~1m of negative offset at the southern half of graben subsidence, that is, horizontal movement toward the minor eruption site at the graben floor.

The 3D displacements derived from both CSK ascending and descending data during co-diking period show not only crustal deformation of graben formation but also icecap surface change due to subglacial ground deformation (Figure 5-3b). At ice-free region, the 3D displacements reveal ~3 m of rift-perpendicular horizontal displacement with ~1 m of uplift at each graben flank, and ~5 m of subsidence with 1 m of SSW horizontal displacements at the graben floor. Although icecap surface far from the graben moves toward north, the co-diking 3D displacements represent eastward movement on the icecap near the graben. Due to the subglacial ground deformation, icecap horizontal displacements near the graben are larger than that far from the graben.

Figure 5-4 shows cumulative TSX pixel tracking between 26 July 2012 and 4 September 2014 and between 4 September 2014 and 20 November 2014 (Table 5-1). Although spatial resolution of TSX data is nearly the same as that of CSK data, the TSX pixel trackings are noisier than CSK pixel tracking because temporal baseline of the first TSX pair is over two years. Due to the decorrelation problems, the TSX data could not detect icecap surface displacement, while the TSX

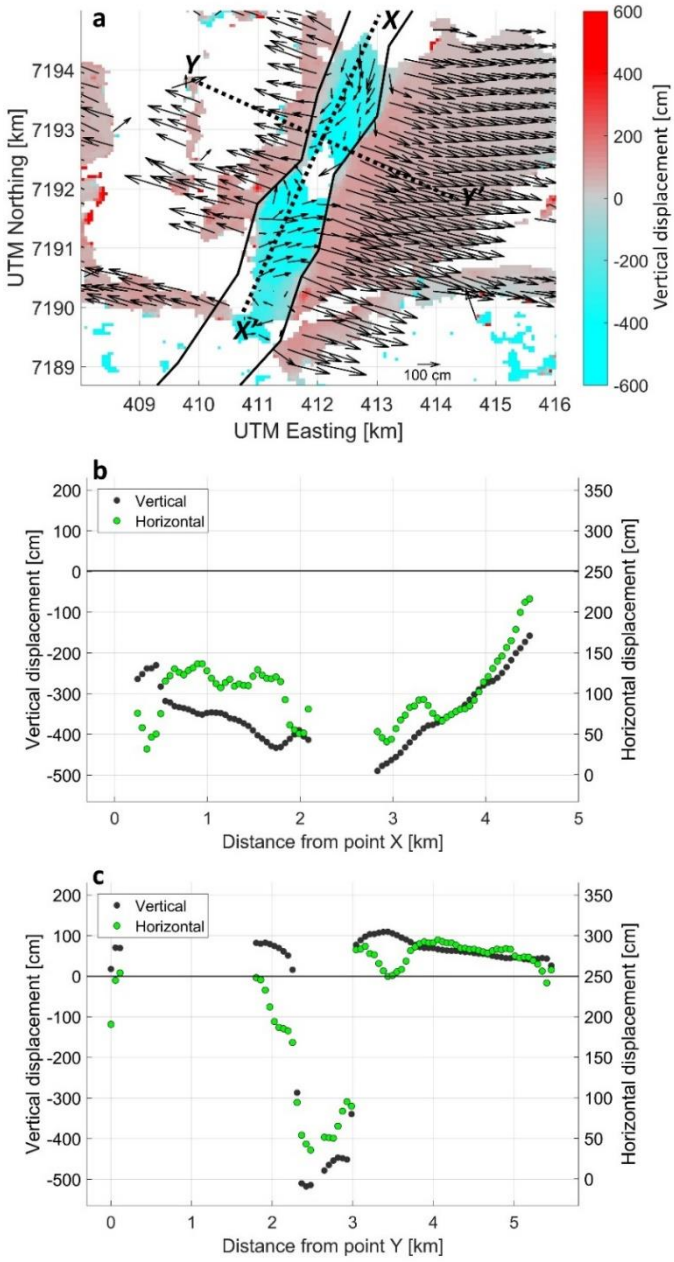


Figure 5-5. Enlarged 3D displacement inferred from CSK and TSX dataset and cross-section across and along the graben subsidence. (a) Enlarged 3D displacement inferred from TSX ascending and CSK descending data. The displayed region is shown in Figure 5-4c. Black solid lines trace discontinuities of vertical displacement. Dashed lines show locations of profiles along the graben (X-X'), and that across the graben (Y-Y'). Arrows show the direction and amount of horizontal displacement. Scale of horizontal displacement is shown at the right-bottom of the figure. (b) Profile of vertical (grey dots) and horizontal displacement (green dots) along X-X'. (c) Profile of vertical (grey dots) and horizontal displacement (green dots) along Y-Y'. Right axis shows the vertical displacement. Left vertical axis shows the horizontal displacement.

pixel trackings reveal wider displacement field over the ice-free region than the CSK ascending data. TSX range offset shows 5 m of positive signal at the subsiding graben. The amplitude of positive signal corresponds to the CSK co-diking range offset from ascending track in Figure 5-2b. TSX azimuth offset shows not only signal at the graben flank, implying NW-SE extending horizontal displacement, but also horizontal displacement toward the minor eruption site at the graben subsidence; 1 m of negative signal at the northern half of graben floor and 40 cm of positive signal at the southern half of graben floor. The negative signal at the northern half of graben floor was also identified in the CSK co-diking azimuth offset from ascending track. Figure 5-4c shows another co-diking 3D displacements which are inferred from TSX ascending and CSK descending data, and Figure 5-5a shows enlarged 3D displacements near the graben. The region is shown in Figure 4c as black box. The 3D displacements indicate 6 m of subsidence with 1 m of rift-parallel horizontal displacements toward the minor eruption site at the graben floor (Figures 5-4c and 5-5a). At the graben flanks, 3 m of WNW-ESE horizontal displacements, which are nearly perpendicular to the graben axis, with 1 m of symmetric uplift (Figures 5-4c and 5-5c).

RS2 data was acquired from two individual ascending tracks; track 81 (T81) and 181 (T181). We employed a larger window size for RS2 dataset to reduce decorrelation noise (Figure 5-6, Table 5-1). We processed one RS2 pair of 1 August 2014 – 18 September from T81 to infer co-diking offset. RS2 T181 dataset is used to check whether we can detect consistent displacement patterns with the RS2 T81 pixel tracking. Pre-diking range offsets indicate positive signal on the icecap, implying ice thinning, as we showed with CSK range offsets reveal in Figures 5-6a and 5-6d. The pre-diking RS2 azimuth offset are seriously contaminated by noise, and we could not identify any signals of icecap surface movement (Figures 5-6g and 5-6j). Co-diking RS2 range offsets reveal rectilinear positive signal along the dike at both non-ice region and the icecap, indicating graben subsidence. RS2 co-diking azimuth offsets show signal discontinuities along the dike at both ice-free region and icecap

(Figure 5-6h and 5-6k). The signal signs on both ice-free and icecap regions are consistent with each other, and signal amplitude on the icecap is stronger than that at ice-free region.

5.2.3 Estimation of subglacial ground deformation

We evaluate crustal deformation taking place beneath the icecap using pixel tracking data as presented in Chapter 5.2.2. Since our TSX data showed only co-diking signal, we used only CSK and RS2 data to infer the subglacial crustal deformation. Our strategy to estimate the subglacial ground deformation is to subtract the scaled pre-diking signal (cm/day) from the co-diking signal (cm). Here we assume that the pre-diking data contain only the icecap surface movement. The scaling factors in each case were determined so that the inferred crustal deformations became smooth at the edge of the icecap. Each of data acquisition intervals and the scale factors are shown in Table 5-1.

Figures 5-2c and 5-2f show the corrected icecap signal, call it “ice-corrected signal” as follow. The ice-corrected CSK range offsets from both ascending and descending track show insignificant offsets along the icecap edge, indicating that the icecap surface movement in CSK range offset could be well-corrected. Although the CSK coverages over the icecap are limited, the CSK range offsets isolate the subglacial crustal deformation due to the dike intrusion. Figure 5-7 shows the profiles of co-diking and ice-corrected range offset across the graben. The profiles of the co-diking signal at non-ice region (profile P-P’) and the ice-corrected signal (profiles Q-Q’ and R-R’) also suggest that the icecap signal in the co-diking signal well-corrected because all signal trends are similar. The icecap signal correction was also functioning as expected in the CSK ascending azimuth offset (Figure 5-2i), whereas the 1 m of negative residual was still leaving on the icecap in the CSK descending azimuth offset (NNE horizontal displacement) even though we tried to change the scale factors to reduce the icecap signal (Figure 5-2l).

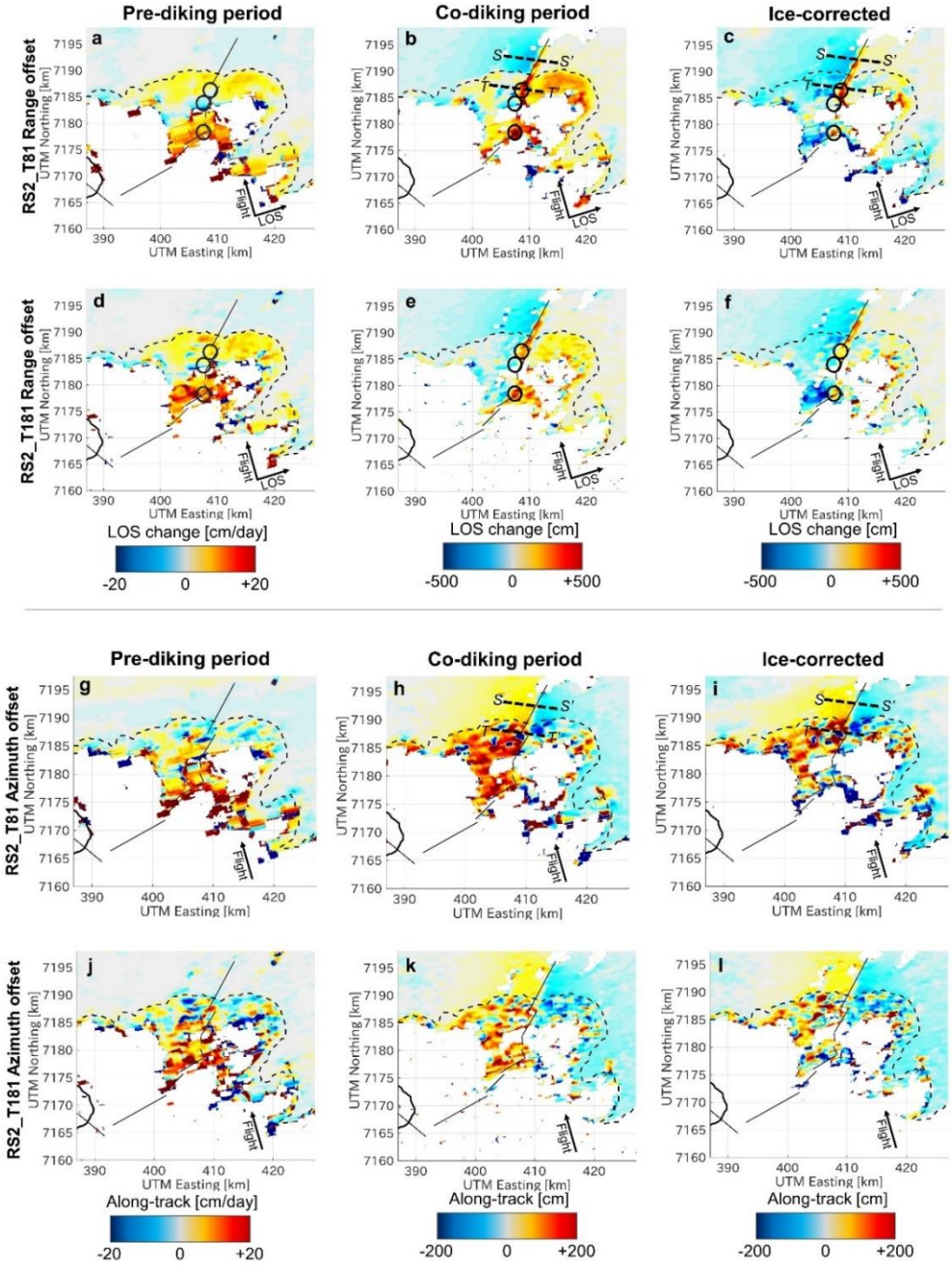


Figure 5-6. RADARSAT-2 (RS2) pixel tracking results during pre- and co-rifting period and ice-corrected signal. RS2 range offset (line-of-sight: LOS) from track 81 (a-c, pre-diking: 8 July 2014-1 August 2014, co-diking: 1 August 2014-18 September 2014, ice-corrected) and track 181 (d-f, pre-diking: 28 June 2014-8 August 2014, co-diking: 8 August 2014-1 September 2014, ice-corrected). RS2 azimuth offset (along-track) from track 81 (g-i) and track 181 (j-l). Dotted lines show the profiles of R-R', and S-S' in Figure 5-8. Dashed lines trace outline of the icecap. Solid black lines and circles are the locations of dike segments and ice cauldrons after Sigmundsson et al. (2015), respectively. Red triangle denotes the Holuhraun main eruption site during the episode. Black dots are selected points of time series of ice surface change in Figure 5-9. Black dots with capital letters (A-C) locate observation points for time-series of icecap surface changes (Figure 5-9). Coordinates are in UTM zone N28.

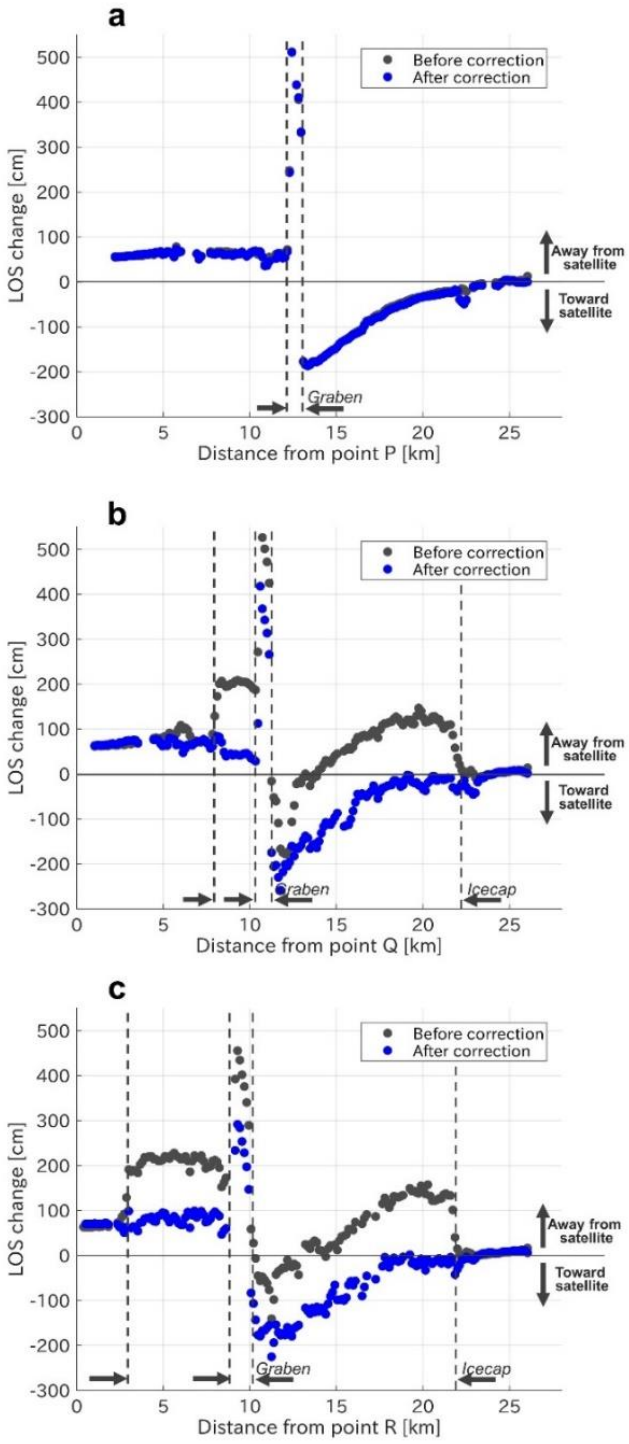


Figure 5-7. Cross sections of descending Cosmo-SkyMed (CSK) range offset during the co-diking signal (grey dots) and ice-corrected signal (blue dots). Profiles along P-P' (a), Q-Q' (b), and R-R' (c). Each location of cross section is shown in Figure 5-2. Unit vector of CSK descending range offset is [e_{east}, e_{west}, $e_{vertical}$] = (-0.443, 0.118, -0.889). Arrows indicate locations of icecap terminus along each cross section. Vertical dotted lines show the icecap edge and displacement discontinuities.

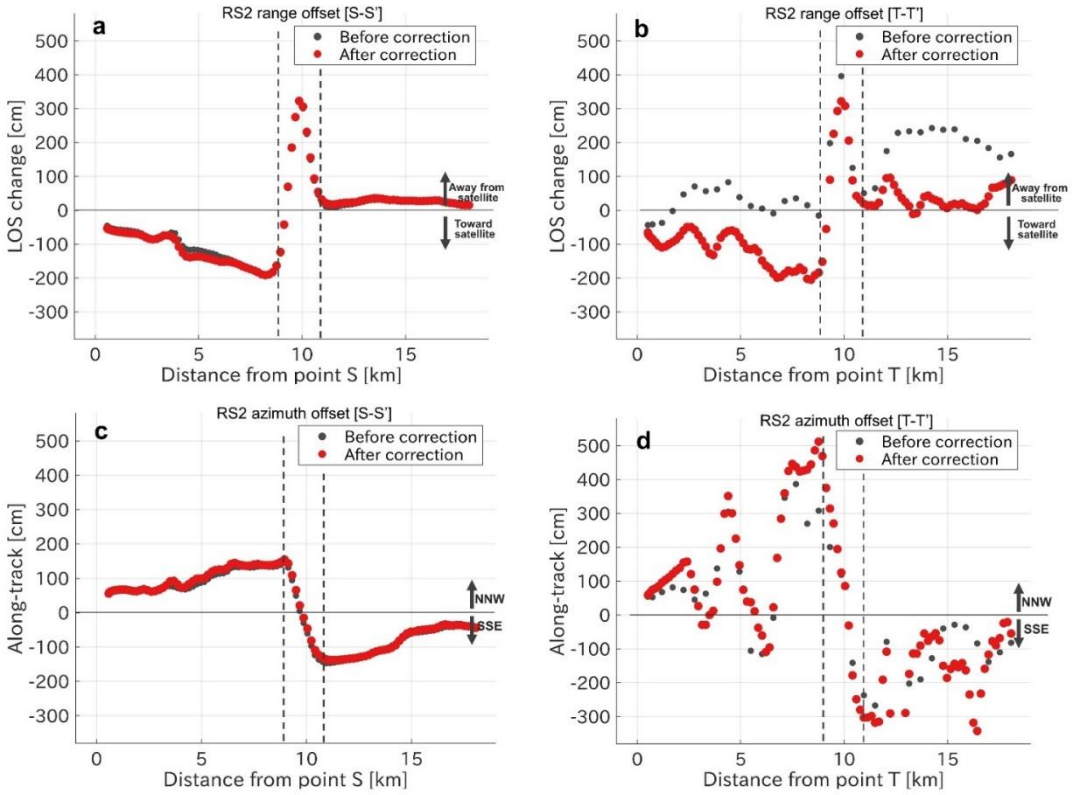


Figure 5-8. Profiles of RADARSAT-2 (RS2) range and azimuth offset in Track 81 during the co-diking signal (grey dots) and ice-corrected signal (red dots). (a) Profile S-S' and (b) profile T-T' of range offset. (c) Profile S-S' and (d) profile T-T' of azimuth offset. The locations of profile S-S' and T-T' are shown in Figure 5-6. Unit vector of RS2 range offset and azimuth offset is $[e_{east}, e_{west}, e_{vertical}]$=(-0.443, 0.118, -0.889). Dotted lines show the location of displacement discontinuities.

Figures 5-6c and 6f show the RS2 ice-corrected signal, and the profiles along S-S' and T-T' show in Figure 5-8. Co-rifting RS2 range offsets also show the signal of both crustal deformation and icecap surface movement, the rectilinear positive signal in the corrected range offsets implies the graben subsidence beneath the icecap.

5.2.4 Temporal changes of icecap surface change

In order to study the temporal changes of icecap surface at the northernmost part of the icecap, we applied pixel tracking approach to both CSK and C-band Sentinel-1A data from 2014 July to end of 2016 (Figure 5-9, Appendix A). We set 256 by 256 pixels of window size for range and azimuth

direction, respectively. In this chapter, we used only range offset to evaluate the temporal variation of icecap surface movement. Because the incidence angles are slightly different between CSK and S1A dataset, we normalized LOS displacement by the cosine of the radar incidence angle as follow to correct the variation of observation geometry.

$$\Delta LOS = \frac{d_{LOS}}{\cos i}$$

ΔLOS is independent of vertical component of LOS displacement, d_{LOS} is the measured LOS displacement, and i is the radar off-nadir angle. The temporal variation shows the data within 500 by 500 m around the observation points A-C where the points are shown in Figure 2a-e. We discarded the cross correlations of below 0.05. No filtering functions in space and time domains were employed. Here we did not consider variations of microwave penetration depth through ice and snow depending on the radar wavelength and polarization (Rignot et al., 2001).

Figure 5-9 shows the temporal variation of vertical component of LOS of CSK and S1A data. The time-series of both ascending and descending tracks show positive peaks of vertical component of LOS change during summers, suggesting ice thinning due to ice melting. Maximum vertical component of LOS change is 5-8 cm/day at the observation points. The time of reaching maximum peak are slightly different from year to year between June and September, although maximum values of vertical component of LOS change are similar through 2014-2016. Only few centi-meters per day of positive or negative vertical component of LOS change were observed from autumn to spring, indicating relatively stable conditions.

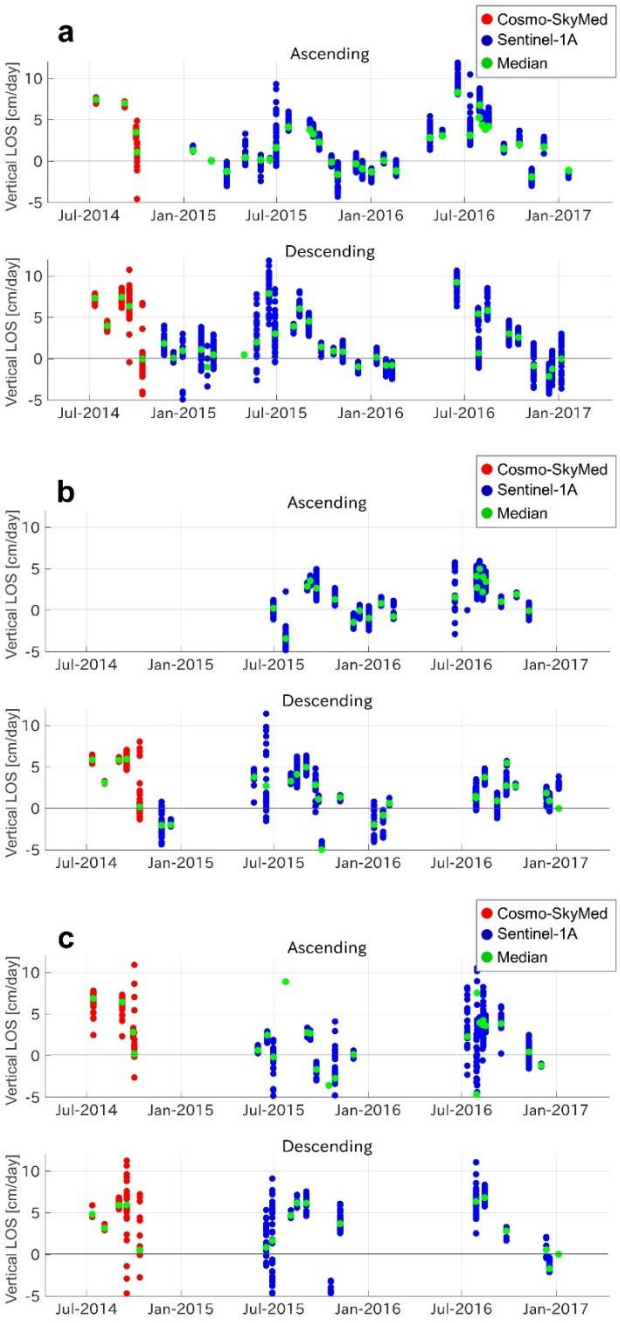


Figure 5-9. Time-series of vertical component of line-of-sight (LOS) change on the icecap from June 2014 to January 2017. The data are inferred from COSMO-SkyMed (CSK, Red dots) and Sentinel-1A (S1A, Blue dots) range offset within 500 by 500 m around points A (a), B (b), and C (c), where the locations of points A-C are shown in Figures 5-2 a-f. The vertical component of LOS change is decomposed by using cosine of off-nadir angle. Off-nadir angles for CSK and S1A data are 27.3 and 33.4 degrees, respectively.

5.3 Elastic modeling

5.3.1 Model setting and geometry

The ice-corrected signals provide us with the crustal deformation signals under the icecap due to the dike intrusion, extending the spatial coverage of observations. Crustal deformation is often interpreted by analytical solutions for rectangular dislocation (Okada, 1985, 1992) or triangular dislocation (Meade, 2007) in an elastic half-space and we follow that approach. Our model consists of a vertical dike and two graben bounding fault planes, in order to reproduce both near-graben and far-field displacement. Using the ice-corrected signals, we invert for the distributions of both dike opening and fault slip. We used analytical solutions for triangular dislocation elements in a homogeneous elastic half space from Meade (2007) to represent curved planar segments without gaps and/or overlaps. Each plane is constructed by triangular elements using Gmsh software (Geuzaine & Remacle, 2009). Patch size of the triangular elements varies from 800 m at shallowest part (0 m) to 2500 m at deepest part (8 km) because spatial resolution of opening/slip distributions at deeper part is worse than that at shallower part. The geometries of the fault segment are similar to the model in Ruch et al. (2015), but the dike segment is extended to further southward as we have more observational constraints on deformation under the icecap. Intersection of fault segment with the Earth surface can be inferred from the sharp displacement discontinuities in CSK and TSX pixel tracking data, indicating surface ruptures of the fault above the dike. Other parameters of each segment are determined by using trial-and-error approach so that we could minimize root mean square misfit and plausible opening/slip distributions (e.g., Furuya and Yasuda, 2011).

In our model, we allow only pure opening along the dike and normal faulting along the graben-bounding faults, because the co-diking 3D displacement reveals the rift-perpendicular horizontal displacement at the graben flanks. The opening/slip distributions were inferred from solving a weighted non-negative least square problems to minimize misfit residuals. A smoothing constraint

for the opening/slip distributions is imposed by using a Laplacian operator to reduce solution roughness and to obtain plausible opening/slip distributions (Simons et al., 2002; Wright et al., 2003).

In addition to the pixel tracking results, we also employed a RS2 InSAR and multiple aperture InSAR (MAI) data (Bechor & Zebker, 2006) (Table 5-2) in our inversion. Although both InSAR and MAI data are lacking data where displacement gradient is high, measurement accuracies of InSAR and MAI are better than that of pixel tracking data. Thus these data are expected to well constrain the far-field displacement. InSAR shows line-of-sight change inferred from phase difference between two coregistered satellite SAR data (Massonnet & Feigl, 1998). Multiple aperture interferograms (MAI) reveal along-track displacement inferred from forward- and backward-looking interferograms (Bechor & Zebker, 2006). Forward- and backward-looking interferograms are derived from two sub-band single look complex images by the azimuth split-beam method. Measurement accuracy of MAI is slightly worse than that of InSAR because of losing a part of band width for azimuth direction. Each standard deviation is shown in Table 5-2.

We applied InSAR and MAI method to RS2 data by using GAMMA software as well as the pixel tracking approach (Table 5-2). We employed an adaptive filter with a window size of 32 pixels to avoid phase unwrapping error (Goldstein & Werner, 1998). The InSAR and MAI were unwrapped phase by using brunch cut algorithm (Goldstein et al., 1988). Topography-dependence signal in the InSAR was corrected by using the mosaiced 1-arc second digital elevation model (DEM) of TanDEM-X and EMISAR (Magnússon et al., 2005). We did not remove any long wavelength phase trend across the data.

The data are weighted by the inverse of diagonal covariance matrices from root mean square (RMS) at the non-deformed area (Table 5-2). The inverted data were subsampled by averaging

neighbor values in space (“multi-looking”) to reduce noise and to reduce number of data. Numbers of data are shown in Table 2. The CSK descending azimuth offsets (Figure 5-2j) and TSX pixel tracking (Figures 5-4a and 5-4b) at the icecap were masked, because strong residuals of icecap signal were left.

5.3.2 Distribution of dike opening and fault slip

Figure 5-9a shows the inferred distributions of opening along the dike and normal faulting along the two graben bounding faults. A peak in opening is located near the southern end of graben bounding faults at the shallowest depth of the dike segment, where the northernmost ice-cauldron formed. The maximum dike opening in our model is 6.1 m. The volume of dike opening inferred from our model is 0.4 km3, which is about 27 % of the predicted volume of magma ejection (Gudmundsson et al., 2016; Pedersen et al., 2017). The distribution of opening in our model is nearly consistent with the model in Sigmundsson et al. (2016), whereas the previous model presented bimodal peaks of pure opening. Our model has little opening at the southern end of the dike because our data does not constrain the opening distribution there. As previous models have demonstrated, the opening distribution concentrates at depths shallower than 5 km, which is clearly above the seismicity along the dike (Ágústsdóttir et al., 2016). The limited seismicity at the shallower depths of 5 km implies little brittle failure due to the low crust rigidity, where pure opening is distributed in our models. The 6 m of normal faulting along the graben-bounding faults can explain almost all of the 6 m of graben subsidence in the 3D displacements (Figures 5-3b and 5-4c). The standard deviations of opening/slip distributions are inferred from the 200-times iterative inversions with synthetic 2D correlated noises (Wright et al., 2003) (Figure 5-10b). The opening uncertainty at a shallow part of the dike segment with the graben-bounding faults is about 60 cm, while the maximum standard deviation of dike opening is 3.1 m at the southernmost of the dike. The estimated standard deviations of normal faulting are below 50 cm, which is significantly less than the inferred normal faulting distributions. The large opening error at the southernmost part of the dike originates from the fact that the displacement data

limited, although the far-field displacement estimated from InSAR and MAI data was expected to constrain the southernmost dike opening.

We evaluated it the ice-corrected signal at the icecap contributed to improve the elastic model. The opening/slip distributions in Figure 5-12 are inferred from the data that are masked above the icecap ("ice-masked model"). The model geometry and other parameters are the same as our best-fit model. Although about 1 m of dike opening was inferred at the southern part of dike, larger standard deviation was identified, indicating less reliability of dike opening. Also, the ice-masked model shows a large artificial implausible slip distribution and large standard deviations at the southern edge of faults. While the distribution patterns of opening/slip are slightly different at the ice-free region, standard deviation of ice-masked model is almost equal to that of our best-fit model at the ice-free region. We therefore conclude that the ice-corrected signal contributes to improve the modeled slip distributions.

Figure 5-11 compares subsampled observations with the calculations based on the inferred opening/slip distributions, and residuals for each data. Root mean square errors (RMSE) are reported at the right bottom of each residual panel. Overall, the synthetic range offsets could well reproduce the signal pattern of each observation. Our model can also reproduce two sharp offset discontinuities along the graben in the range offsets. Even though the weight of CSK descending range offset is larger than that of any other offsets, the misfits are still left in this data set, especially positive residuals at the western part of graben flank. The misfit may derive from a scaled decorrelation noise during the correcting the icecap signal (Figures 5-2d-f). Although the weights of azimuth offset for the inversion are relatively low, the RMSE of azimuth offset is similar level with that of range offset. Our model cannot retrieve well the rift-parallel displacement at the graben subsidence in the azimuth offsets. Regarding the southern half of RS2 data coverage, it is hard to assess whether our model could

reproduce the observations well or not because the observation offsets on the icecap are contaminated by decorrelation noise even if the data were subsampled coarsely. The broad signal patterns of both range and azimuth offset can be reproduced, although the predicted RS2 azimuth offset was significantly underestimated.

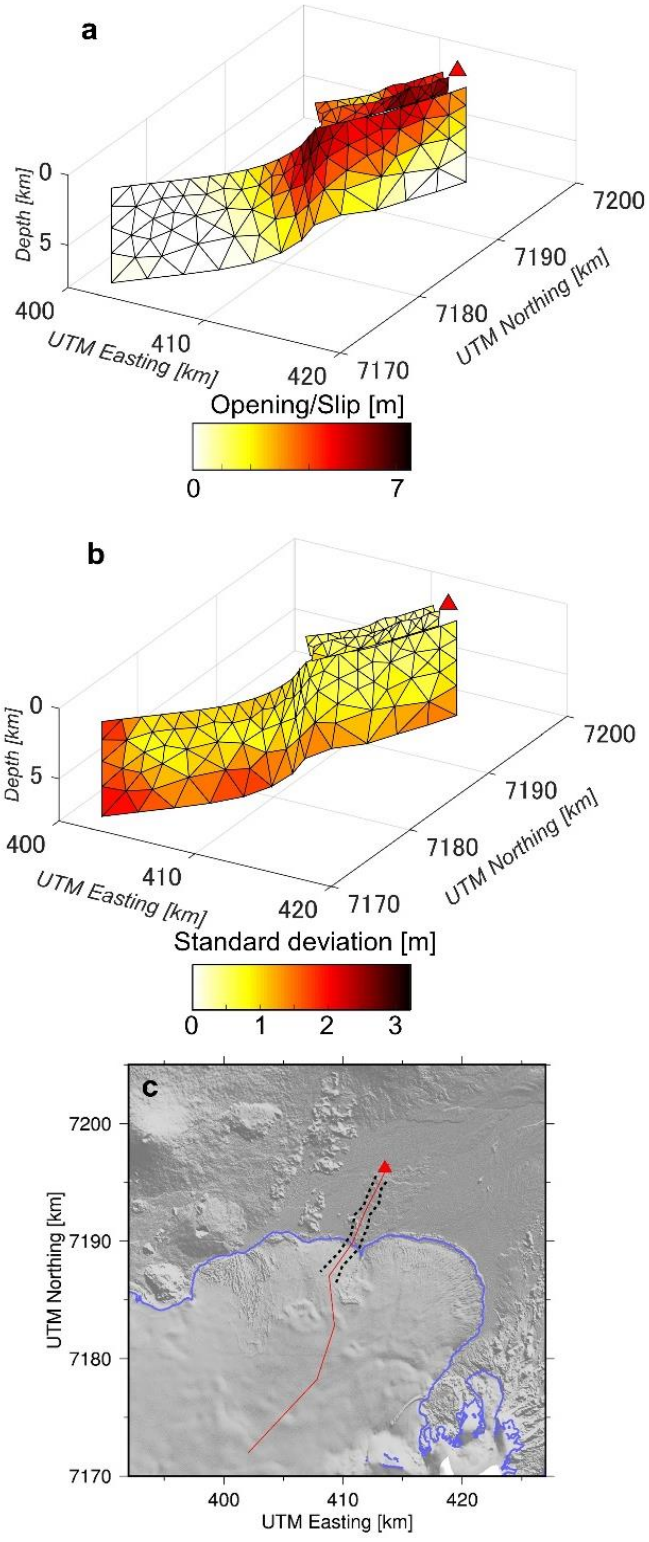
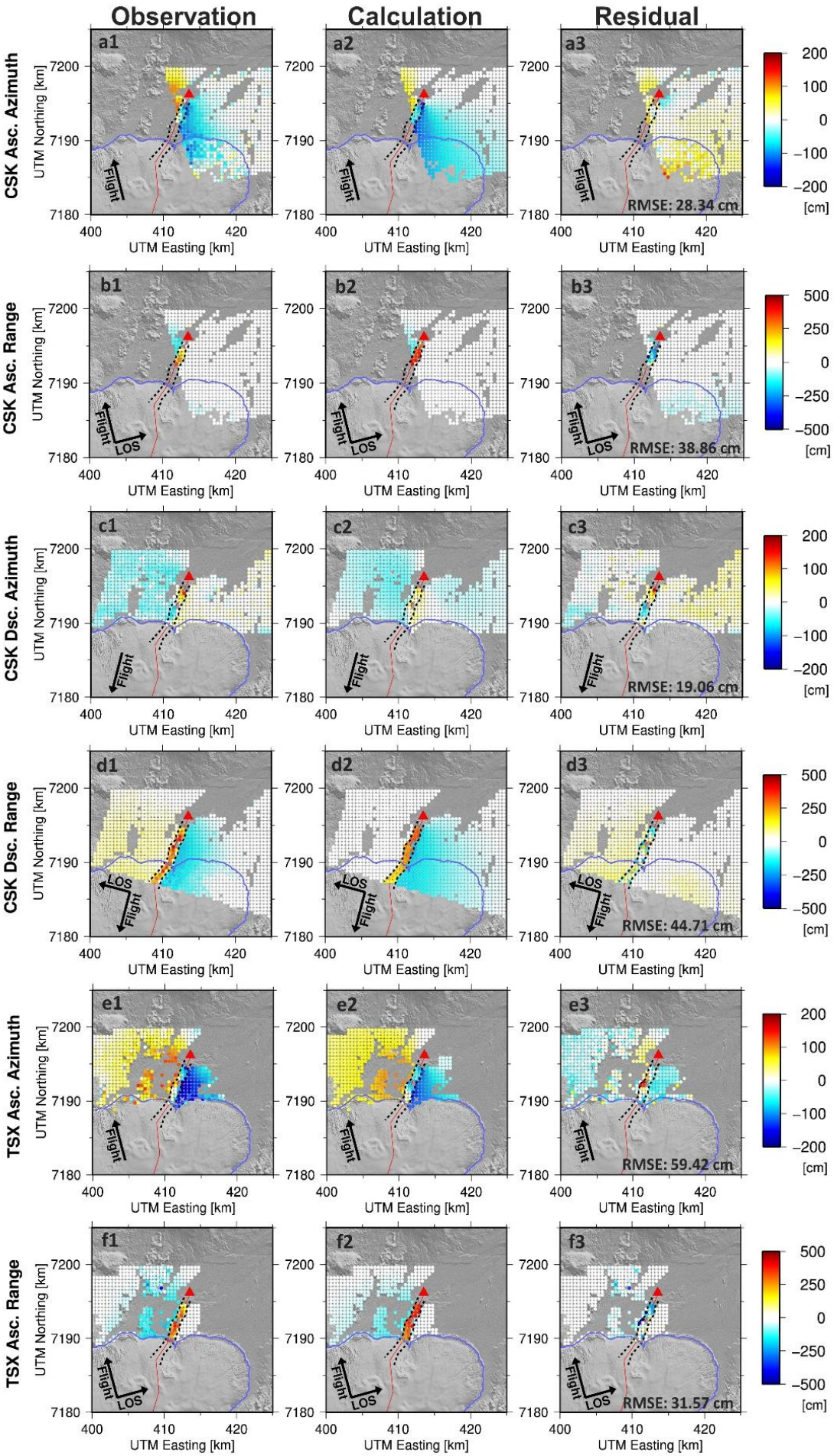


Figure 5-10. Our optimal elastic model and the model geometry. (a) Inferred dike opening and normal faulting along the graben-bounding faults. (b) Standard deviations are derived from 200-times iterative inversions with synthetic 2D random noise. The distributions are projected from NE. (c) Map showing the top location of dike and graben bounding faults, and outline of the icecap. Red triangles show the location of the Holuhraun main eruption site. Light blue line traces the outline of the Vatnajokull icecap. Black dashed lines show the top location of graben bounding faults. Coordinates are in UTM zone N28.


Observation
Calculation
Residual
CSK Asc. Azimuth
CSK Asc. Range
CSK Dsc. Azimuth
CSK Dsc. Range
TSX Asc. Azimuth
TSX Asc. Range
a1
a2
a3
b1
b2
b3
c1
c2
c3
d1
d2
d3
e1
e2
e3
f1
f2
f3
RMSE: 28.34 cm
RMSE: 38.86 cm
RMSE: 19.06 cm
RMSE: 44.71 cm
RMSE: 59.42 cm
RMSE: 31.57 cm
Flight
LOS
UTM Northing [km]
UTM Easting [km]
7180
7190
7200
400
410
420
200
100
0
−100
−200
500
250
−250
−500
[cm]

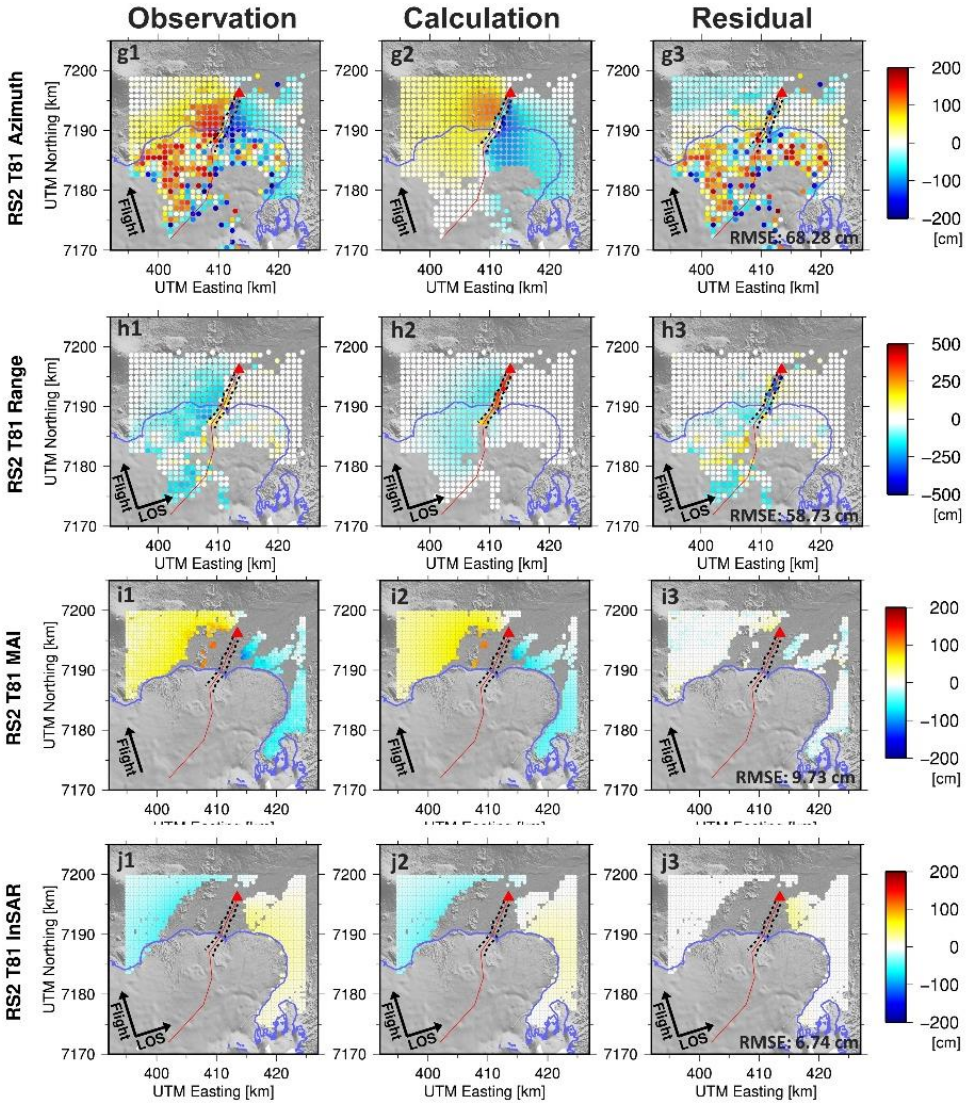


Figure 5-11. C omparison of observations, calculations derived from our model, and residuals. (a-j1) Subsampled observations, (a-j2) calculations inferred by the slip/opening distribution, and residuals (a-j3). (a1-3) Cosmo-SkyMed (CSK) ascending azimuth offset, (b1-3) CSK ascending range offset, (c1-3) CSK descending azimuth offset, (d1-3) CSK descending range offset, (e1-3) TerraSAR-X (TSX) ascending azimuth offset, (f1-3) TSX ascending range offset, (g1-3) track 81 (T81) RADARSAT-2 (RS2) azimuth offset, (h1-3) T81 RS2 range offset, (i1-3) T81 RS2 multiple aperture interferogram (MAI), (j1-3) T81 RS2 interferogram (InSAR). Positive signal of azimuth and range offset show horizontal displacement toward satellite flight direction and line-of-sight change away from satellite, respectively. Dashed black and solid red lines project top edges of graben-bounding faults and the dike segment in out model. Red triangles locate the Holuhraun main eruption. Arrows indicate the directions of satellite flight ("Flight") and line-of-sight ("LOS"), respectively. Blue solid lines traced the outline of icecap.

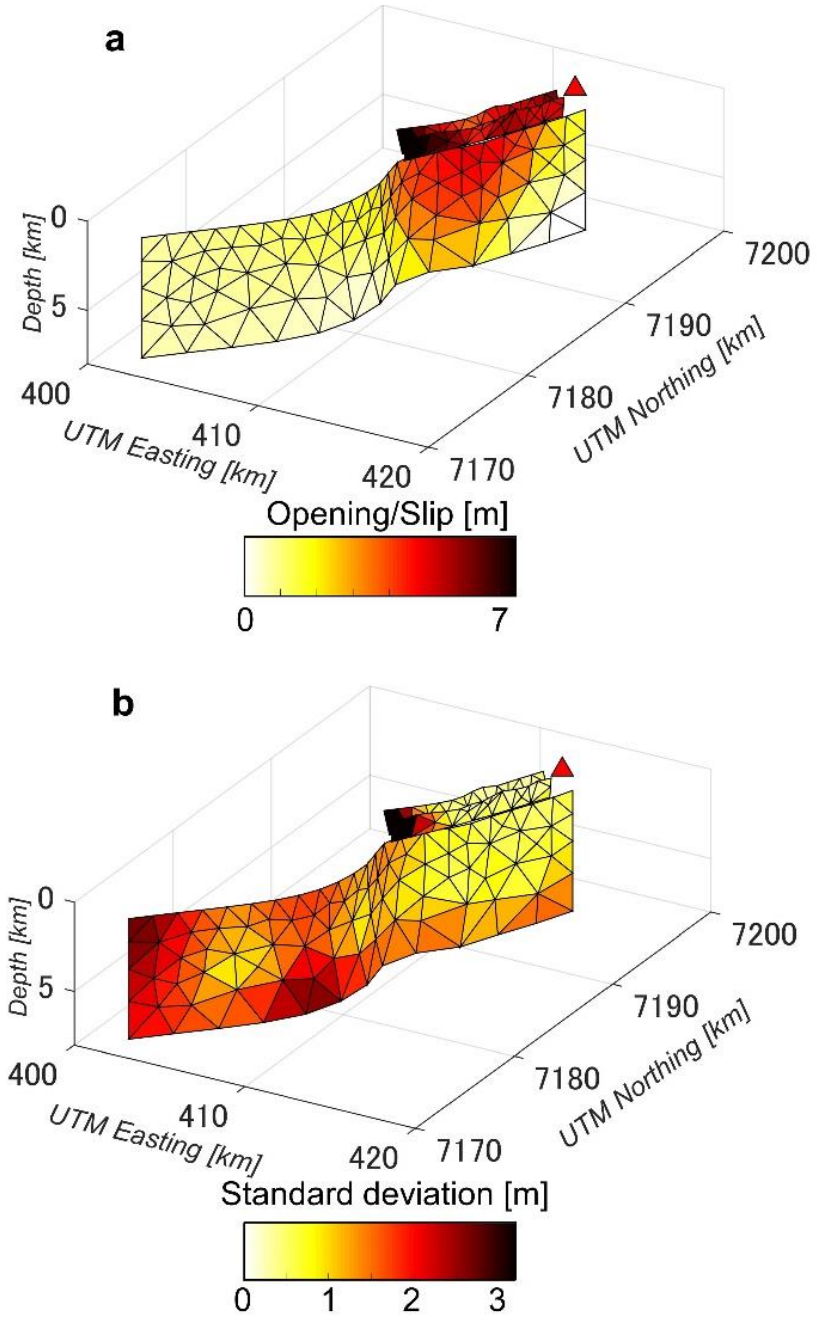


Figure 5-12. Dike opening and normal faulting distributions inferred from the observations which are masked above the icecap and its standard deviations. (a) Inferred dike opening and normal faulting along the graben-bounding faults. (b) Standard deviations are derived from 200-times iterative inversions with synthetic 2D random noise. The distributions are projected from NE. Details are same as Figure 5-10. Color scales are also same in Figure 5-10.

Table 5-2. Dataset for inferring elastic model

Satellite [a]	Orbit [b]	Data [c]	RMS [cm] [d]	Weight [%] [e]	Number of data [f]
Cosmo-SkyMed	Ascending	Range offset	9.3	7.6	3139
		Azimuth offset	10.8	6.6	3208
	Descending	Range offset	3.8	18.5	5137
		Azimuth offset	18.7	3.8	3577
TerraSAR-X	Ascending	Range offset	19.0	3.7	2002
		Azimuth offset	16.1	4.4	2413
RADARSAT-2	Ascending	Range offset	12.76	5.6	727
		Azimuth offset	16.1	4.4	772
		MAI	9.9	7.2	4102
		InSAR	1.9	38.2	2683

a Name of SAR satellite

b Satellite flight direction. Ascending means flight from SSE to NNW. Descending means flight from NNE to SSW.

c Input data for modeling.

d Root-mean-square at non-deformation area. RMS can be regard as measurement accuracy of the dataset.

e Relative weight for the inversion in Chapter 5.3. The weight is based on RMS.

f Number of input data for inversion in Chapter 5.3.

5.4 Discussion

We confirmed that the pixel tracking approach is suitable for isolating subglacial crustal deformation using the scaled pre-diking and co-diking signals. Although we detected the deformation signals above the icecap along northern half of the dike using the RS2 data, the RS2 pixel tracking data showed data lacking above the icecap around the Bárðarbunga caldera. Even though we processed RS2 dataset with shorter temporal baseline, we could not detect the signal there. First possibility is that there are few surface characteristics above the icecap. The pixel tracking approach finds the most similar characteristic within an arbitral window size using a cross-correlation function. The northern edge of the icecap surface where we revealed surface movement using the pixel tracking approach looks surface characteristics there due to steady-state of ice flow, however the icecap surface around the caldera looks smooth expect for the caldera outline. Because the approach cannot distinguish a region where we would like to find with an others region with smooth, we cannot reveal the surface Second possibility is that warm climate during the episode can change ice surface condition. Variation of the back-scatter intensity between two SAR images also induces the decorrelation problem. Even though the topographic height of the summit is about 2000 m and Iceland is one of the Arctic regions, we presume that the climate in summer makes it easier to melt and freeze which induces to vary ice surface condition. Third possibility is the carrier frequencies of radar microwave. The longer the wavelength of radar microwave is, the deeper penetration depths of microwave through ice is (Rignot et al., 2001). In general, the condition near ice surface is more sensitive to precipitation and temperature change comparing with that at the deeper part of ice. The scatter characteristics above ice can be more stable if we employ SAR data acquired by using longer-wavelength radar microwave such as L-band SAR data. We processed a pair of PALSAR-2 data to detect the icecap surface change during the event (Figure 5-13). Even though the data acquisition interval of the PALSAR-2 data we processed is 14 days, the PALSAR-2 interferogram revealed the signals of steady-state of icecap flow. We, however,

could not infer the icecap surface change due to the subglacial dike intrusion using PALSAR-2 dataset because the image did not cover the ice region above the dike. We also show the others CSK pixel tracking data with short intervals of image acquisition covering the Bárðarbunga caldera (Figures 5-14 and 5-15). The CSK pixel tracking data acquired from August to September indicate missing signals above both the Vatnajökull icecap and the ice at Tungnafellsjökull volcano even though the data acquisition interval was 1 day (Figures 5-14 and 5-15), while we revealed signals of the caldera subsidence in the CSK pixel tracking data during October. Thus we propose from these figures that second factor is supposed to be the strongest contributor for missing data in our pixel tracking data, although the others factors can also influence to contaminate our observation data.

In this chapter, the subglacial crustal deformation was inferred by subtracting the scaled pre-diking signal from the co-diking signal (Figures 5-2 and 5-6). Although the icecap signal was corrected well in the range offset, we cannot ignore significant residuals in the RS2 and CSK azimuth offsets. One possibility of the residuals is the difference of physical properties between crust and ice. Generally, crustal deformation can be described as elastic response. Instantaneous ice deformation can also be approximated as elastic deformation, because ice deformation can be described by a non-linear Burger's body viscoelastic model (Tsai et al., 2008). Assuming the co-diking displacement occurs within a short time, we can regard the icecap deformation due to the subglacial crustal deformation as elastic deformation. In order to evaluate the icecap movement due to the subglacial crustal deformation accurately, we may, however, need to consider about the difference of physical properties.

Simulated ice mass balance of the Vatnajökull icecap near Holuhraun during 1991-2006 shows that average mass loss during summer corresponds to 4-6 m of ice thinning (Björnsson & Pálsson, 2008). Our time-series results are broadly consistent with the numerical simulation if we

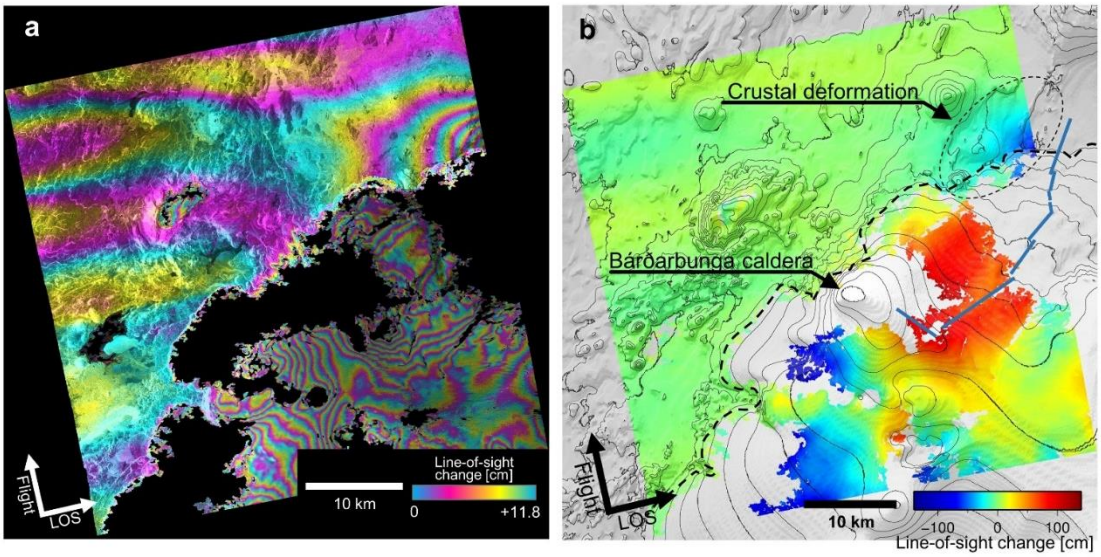


Figure 5-13. A PALSAR-2 interferogram across the Bárðarbunga caldera. a) Wrapped interferogram. Color cycle represents 11.8 cm of displacement along the line-of-sight direction. b) Unwrapped interferogram. Positive signal indicates line-of-sight displacement away from the satellite. Blue lines indicate the dike path inferred from migrated seismicity (Sigmundsson et al., 2015).

assume 5-7 cm/yr of vertical change for 90 days in summer time even if ice mass loss have been accelerating after the study by Björnsson & Pálsson (2008) was published. We note that maximum vertical component of LOS change rate in the summer of 2014 is similar to that in 2015 and 2016. Also, vertical component of LOS change rate during winter of 2014-2015, when the fissure eruption had been still ongoing, decreases to near zero, same as that in winter of 2015-2016 and 2016-2017. These findings suggest no significant regional basal melting anomaly due to the event.

Our optimal model involves both advantages and disadvantages comparing with previous models. Previous models allowed not only opening but also sinistral shearing along the dike based on their geodetic observations and the left-lateral strike-slip earthquakes (e.g., Sigmundsson et al., 2015; Ruch et al., 2016). The amount of shearing is less than 1 m to fit their observations. Our elastic model, however, allowed only pure opening along the dike because the retrieved 3D displacements show rift-

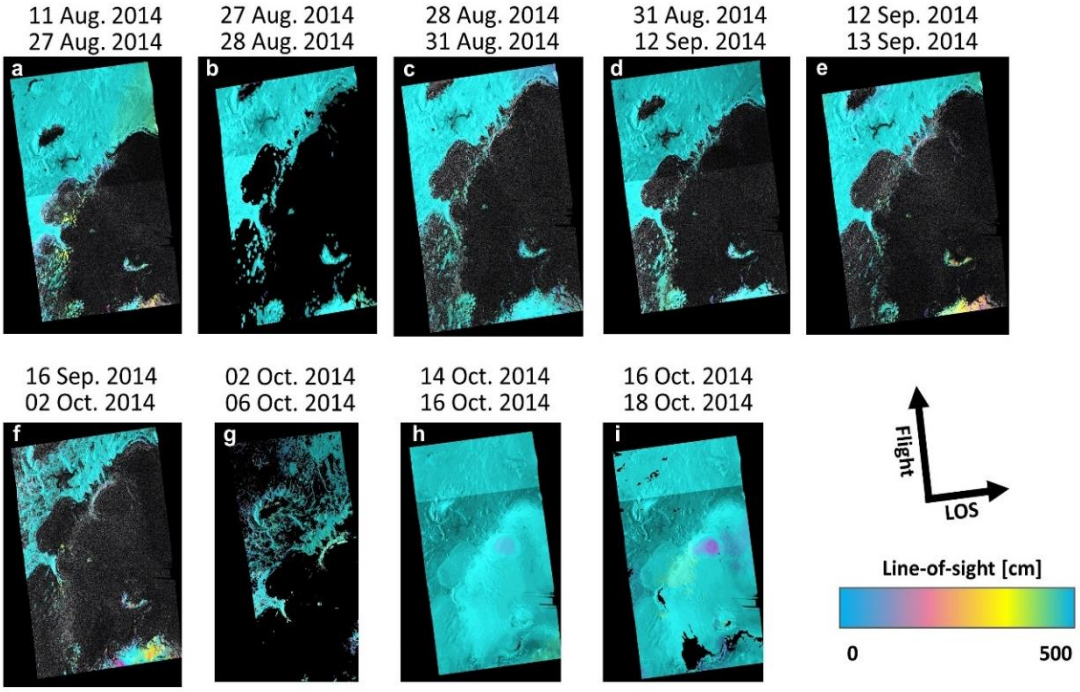


Figure 5-14. CSK pixel tracking data observed from ascending track across the Bárðarbunga caldera. Black color shows data lacking induced by decorrelation problems. Image acquisition date are presented above each figure and Appendix A. Black arrows show the satellite flight direction (Flight) and the beam illuminate direction (LOS), respectively.

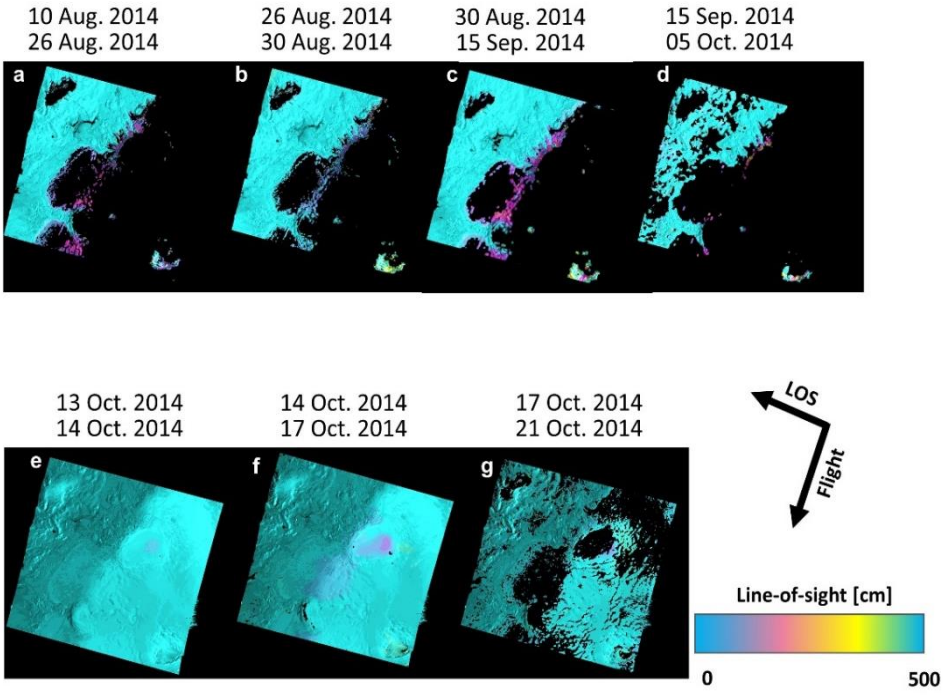


Figure 5-15. CSK pixel tracking data observed from descending track across the Bárðarbunga caldera. Details are same as Figure 5-14.

perpendicular horizontal displacements at the graben flanks with few left-lateral displacements (Figures 5-3b and 5-4c). We confirmed that our model could retrieved the pixel tracking observations well even at the inferred subglacial crustal deformation (Figures 5-11). Although we did not employ GNSS data for our inversion, the optimal model in this chapter has been constrained by the far-field displacement derived from RS2 InSAR and MAI data instead of GNSS observation (Figures 5-11i and 5-11j). The requirement of shearing for fitting the geodetic observations would need to debate in detail. Another issue in our model is that our model did not consider the tectonic stress (Spaans & Hooper, 2018). Although previous GNSS measurement have revealed 18-19 mm/yr of extensional displacement toward WNW-ESE (DeMets et al., 2010), we ignored the tectonic stress because we focus on only the short-term displacement in this chapter.

5.5 Post-emplacement deformation of Holuhraun lava field

The Bárðarbunga dike intrusion episode accompanied fissure eruptions from September 2014 to Fubruary 2015 and 83 km^2 of the lava field formation at Holuhraun plain which located the north of Vatnajokull icecap (Gudmundsson et al., 2016; Pedersen et al., 2017; Sigmundsson et al., 2015). After ejected magma emplaced, the lava deforms, usually thinning, due to thermal contractions of lava, degassing and solidification (Caricchi et al., 2014). Post-emplacement deformations of lava fields observed by InSAR have reported, such as at Hekla volcano, Iceland (Wittmann et al., 2017), Miyakejima volcano, Japan (Furuya, 2004). Regarding the Holuhraun lava field, a TanDEM-X DEM difference observation between September 2014 and February 2015 showed 42-45 m of the lava field height change due to the fissure eruption (Dirscherl & Rossi, 2018; Rossi et al., 2016). On the other hands, the post-emplacement deformation in the lava field have not reported, to our knowledge. We provide preliminary results of the post-emplacement lava field deformation using L-band PALSAR-2 dataset as follow.

We applied the pixel tracking and the conventional stacking approaches to PALSAR-2 dataset for depicting the post-emplacement lava field deformations (Table 5-3). Analysis of PALSAR-2 data was computed by the GAMMA software. Topographic fringes were corrected by using 1arc-second ASTER GDEM, and long-wavelength fringes across the interferograms could be negligible. We adopted the minimum cost flow algorithm for the phase unwrapping (Costantini, 1998). We inferred the cumulative LOS changes by stacking interferograms of shortest temporal baseline in each track. Because the ascending PALSAR-2 InSAR spanning 2 February 2015 and 6 July 2015 was contaminated by phase unwrapping errors due to decorrelation problems, we employed the pixel tracking to depict LOS changes. The cumulative LOS change derived from the ascending PALSAR-2 dataset thus involves the pixel tracking and InSAR data. To correct observation geometries between the ascending and descending LOS changes, we normalized as vertical components of LOS change by dividing LOS change by cosine of each incidence angle. The equation for the correction is described in Chapter 5.2.4. We evaluate the temporal variation of lava field deformation at the maximum deformation site, and plotted signals within 500 m of the site. The variation from each median value can be considered as uncertainties of the observation.

Figure 5-16 shows the cumulative LOS changes derived from PALSAR-2 pixel tracking and InSAR and the temporal variation of vertical component of LOS change at the maximum displacement point which located slightly far from the eruption site. As we mentioned above, the ascending data involves both the pixel tracking and InSAR data, the descending data presented only InSAR data. Some InSAR showed decorrelation noises at outside regions of the lava field due to low signal-to-noise ratio (SNR). The low SNR could be caused by smooth surface characteristics where are few vegetations, covering/melting snow and covering volcanic ash. While the SNR above the lava

field was relatively high because the rough surface characteristics of the lava. The signal above the lava field therefore could be detected constantly. The deformation signals spread out from the eruption site toward northeastward direction as the topographic gradient is also sloping toward NE. The signal distributions are nearly consistent the lava flow through a channelized lava feeding system during the lava field formation (Pedersen et al., 2017). The maximum cumulative vertical component LOS changes in the ascending track depicted greater than 5 m of downward movements since February 2015. The temporal variation of decreasing deformation rate in the ascending data can be fitting by exponential and/or logarithmic functions rather than linear functions. For the descending data, the cumulative deformation amplitude is smaller than that of the ascending data. The reason is that the descending InSAR spanning 25 February 2015 to 8 April 2015 could also not show LOS changes correctly because of phase unwrapping errors. Although we applied the pixel tracking approach to the descending image pair, the procedure could not detect surface deformation signals because the descending PALSAR-2 data were acquired by using ScanSAR mode. Although applying the pixel tracking to the ScanSAR data is challenging for detecting signals due to worse spatial resolutions of SAR images, some papers have reported a glacier flow map of Greenland by applying the pixel tracking to Sentinel-1 interferometric wide (IW) swath mode, which depicts moderate spatial resolutions with wide coverages (e.g., Nagler et al., 2015). The PALSAR-2 ScanSAR could have detected the deformation signal if the research target area is wider and if the deformation is greater. Another pixel tracking spanning 24 November 2014 to 2 February 2015, indicating the co-eruptive period, depicted different signal trend, that is, greater 6m of negative signal with extending toward NE (Figure 5-17). Although negative signals from the ascending observation geometry propose eastward movements and/or uplifts, we expect that the negative signals in the pixel tracking indicate a combination of both eastward movements and uplift because of horizontal spreading and

accumulations of lava through channelized feeding systems. Lacking data region was inferred the newly lava covering area during the image acquisition interval.

Table 5-3. PALSAR-2 dataset for detecting the post-emplacement deformation.

Track	Orbit	Acquisition mode	Spatial resolution (Range, Azimuth [m])	Date [dd.mm.yyyy]	B_perp [m]
2	Ascending	Stripmap mode	4.3, 3.2	24.11.2014	0
				02.02.2015	225.40
				06.07.2015	224.63
				14.09.2015	65.63
				23.11.2015	193.58
				01.02.2016	173.76
				04.07.2016	106.53
				21.11.2016	129.67
				03.07.2017	167.39
				11.09.2017	184.94
113	Descending	ScanSAR mode (Swath No. 3)	19.0, 25.9	08.04.2015	0
				29.07.2015	-350.11
				02.12.2015	-190.00
				24.02.2016	-41.86

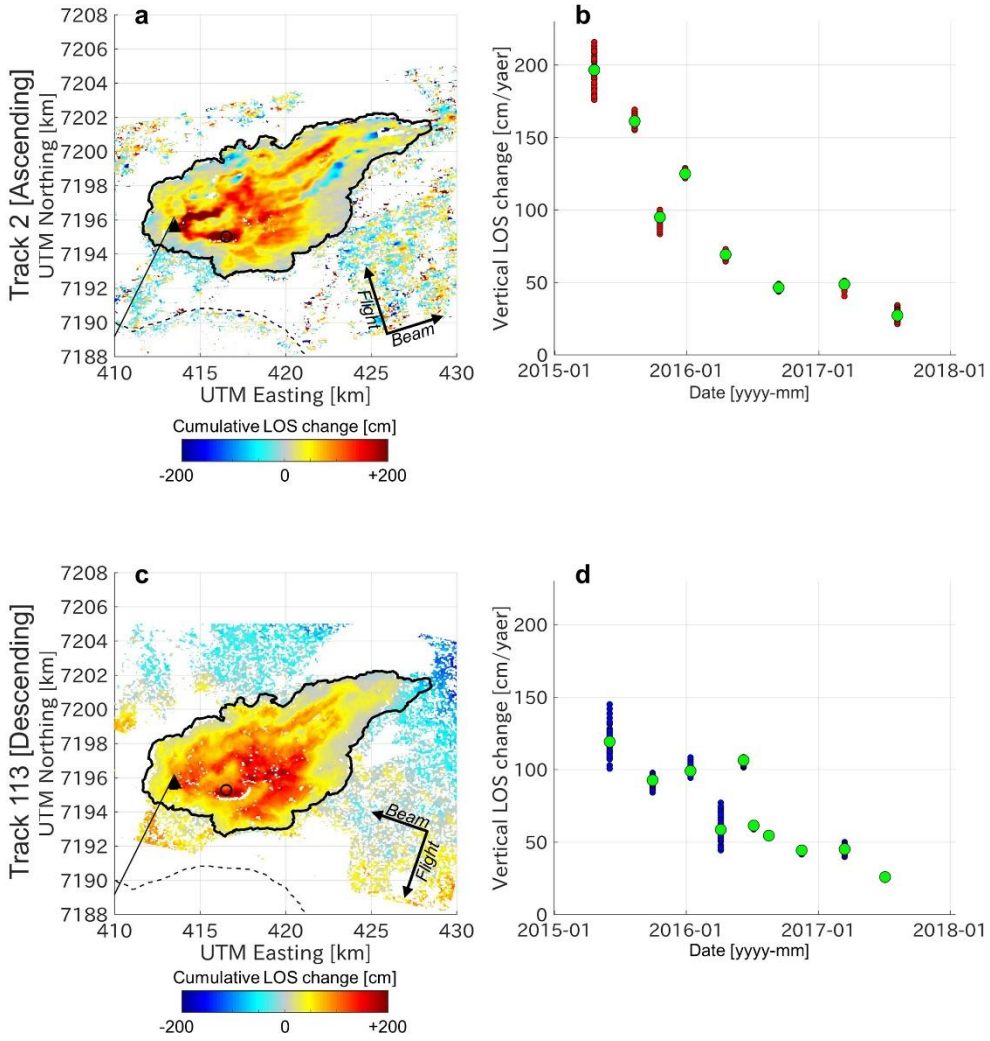


Figure 5-16. Lava field subsidence derived from stacked PALSAR-2 InSAR. (a, c) Cumulative vertical components of LOS change observed from the ascending (track 2) spanning 2 February 2015 to 11 September 2017 and the descending (track 113) PALSAR-2 data spanning 8 April 2015 to 23 August 2017, respectively. The vertical component LOS is normalized by divided LOS changes by their radar incidence angles for correcting observation geometries. Dashed line indicates the icecap outlines. Thin and thick solid lines are the dike path and the lava field outline, respectively. Black triangle located the fissure eruption site during the episode. Open circle indicates the point where the time-series of LOS change shows. Note that positive signals show LOS lengthening, approximating downward movement. b, d) Time-series of LOS changes of ascending and descending PALSAR-2 data, respectively. Green dots are median values of each dataset. Red and blue bots indicate the vertical component of LOS changes within 500 m of the observation point in the ascending and descending PALSAR-2 dataset, respectively.

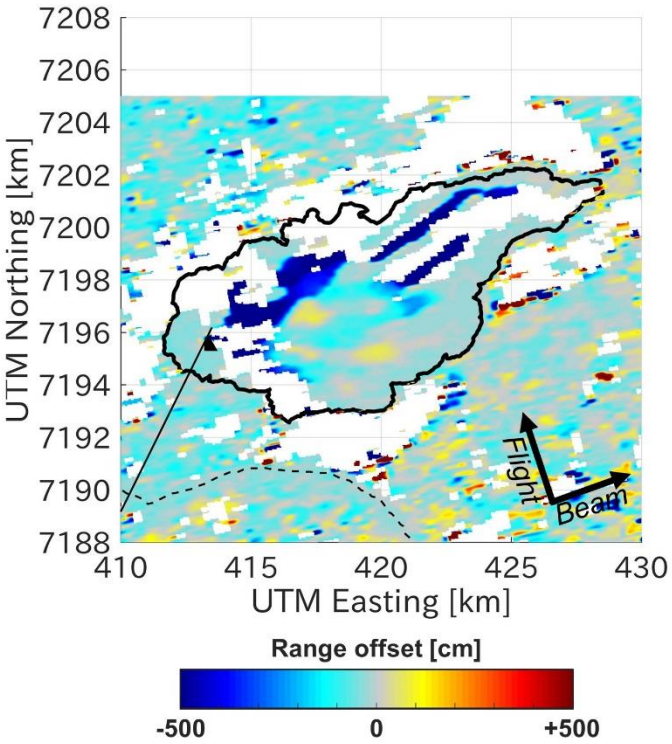


Figure 5-17. Range offset between 24 November 2014 and 2 February 2015. Negative signals indicate LOS shortening. Thick and thin lines trace the outline of the lava field and the dike, respectively. Dashed line presents the outline of the icecap.

Chapter 6

Dynamic Slip Partitioning Associated with the 2016 Kumamoto Earthquake Sequence, SW Japan

Main content in this chapter have been published in *Earth, Planets and Space*

Himematsu, Y., M. Furuya (2016) Fault source model for the 2016 Kumamoto earthquake sequence based on ALOS-2/PALSAR-2 pixel-offset data: evidence for dynamic slip partitioning, *Earth, Planets and Space*, 68:169, DOI 10.1186/s40623-016-0545-7

Chapter 6. Dynamic slip partitioning associated with the 2016 Kumamoto earthquake sequence, SW Japan

6.1 Introduction

Two Mw > 6 earthquakes hit Kumamoto prefecture on April 14, 2016 (Mw 6.2 [M_{JMA} 6.5] 12:26:41.1 UTC; Mw 6.0 [M_{JMA} 6.4], 15:03:50.6 UTC), followed by another shock (Mw 7.0 [M_{JMA} 7.3]) on the next day, 15 April (16:25:15.7 UTC) (Figure 6-1); the Mw is inferred by Japan Meteorological Agency (JMA) catalog (http://www.jma.go.jp/jma/en/2016_Kumamoto_Earthquake/2016_Kumamoto_Earthquake.html). After the main shock, the epicenters of aftershocks migrated from Kumamoto in NE and SW direction (Figure 6-1). According to the JMA focal mechanisms, right-lateral slip is the dominant component, whereas some focal mechanisms of the aftershocks indicate normal faulting. Moreover, not only the main shock but also the foreshocks and the aftershocks included significant non-double couple components (Figure 6-1), suggesting complex mechanisms of the Kumamoto earthquake sequence. Previous geological and geodetic observations pointed out the presence of Beppu-Shimabara rift system across the Kyushu island (Ehara, 1992; Matsumoto, 1979; Tada, 1993), along which the NE–SW trending seismicity of the 2016 Kumamoto earthquake sequence was distributed. The northeastern edge of the rift system is located at the most western part of the Median Tectonic Line that is the longest fault system in Japan (Ikeda et al., 2009). Meanwhile, the northernmost end of Okinawa trough reaches the southwestern edge of the rift system (Tada, 1984, 1985). The rift system contains geothermal area and active volcanic system including Kujyu, Aso and Unzen volcanoes. Based on geodetic observations by the first-order triangulation survey (Tada, 1984, 1985) and GPS network (Fukuda et al., 2000; Nishimura & Hashimoto, 2006), the central Kyushu region is inferred to be under N–S extension stress regime. Matsumoto et al. (2015) analyzed the focal mechanisms of shallow earthquakes in Kyushu from 1923 to 2013 and showed that Kyushu island was

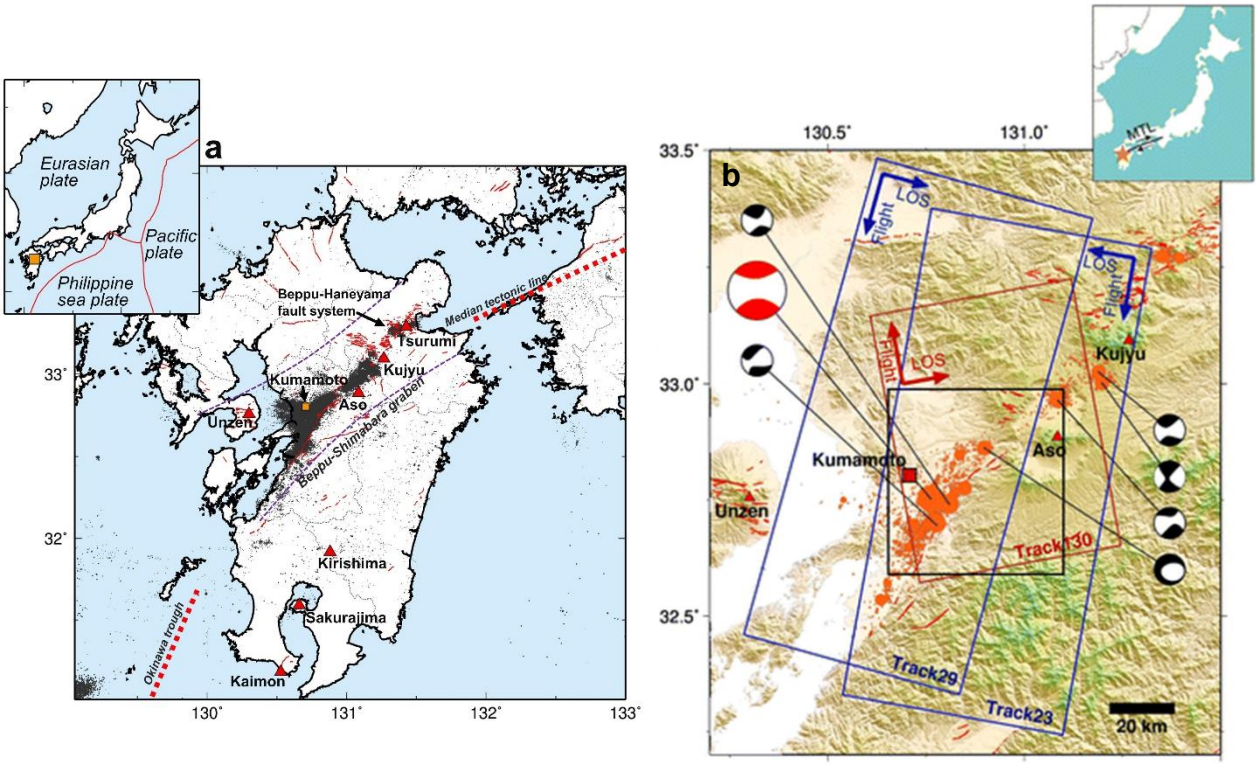


Figure 6-1. Study area in Chapter 6. (a) Japan islands with plate boundaries (red lines) in inset and Kyushu island with seismicity (grey dots) and active fault traces (red lines). Red triangles are active volcanoes across Kyushu island. (b) Orange circles indicate the locations of epicenter during 14-30 April 2014. Beachballs show each focal mechanism of earthquakes which are greater than M_w 5.5. The information of earthquake is derived from Japan Meteorological Agency (JMA) catalog.

Tectonic Line (MTL). In order to understand the mechanism of any seismic event, a variety of sources are available such as seismic wave, tsunami height, Global Navigation Satellite System (GNSS) network and SAR data. The focal mechanisms reported by JMA are based on seismological data that are acquired at distant stations from the hypocenter. Regarding the "main shock" of the Kumamoto earthquake sequences, however, it has been pointed out that another earthquake (M_{JMA} 5.7) occurred 32 s after the main shock at Yufu City, ~80 km to the NW from Kumamoto (JMA hypocenter catalog in Japanese [http://www.data.jma.go.jp/svd/eqev/data/daily_map/20160416.html]). Hence, the estimated mechanism solution based on the far-field and long-period seismic data could be biased due

to mixed-up wavelets. In contrast, co- and post-seismic displacements derived by geodetic techniques indicate permanent deformation signals in the near-field around the hypocenters, and thus, the estimated fault model could be less ambiguous, at least, in terms of the location and the geometry of these faults. Over the last two decades, a growing number of fault models have been derived from geodetic data such as GNSS and Interferometric SAR (InSAR). Regarding the 2016 Kumamoto earthquake sequences, Geospatial Information Authority of Japan (GSI) has shown first report of InSAR(Hanssen et al., 2001; Massonnet & Feigl, 1998) and Multiple Aperture Interferometry (MAI, Bechor & Zebker, 2006) observation results using the L-band ALOS-2/PALSAR-2 images (http://www.gsi.go.jp/cais/topic160428-index-e.html, last accessed on May 27, 2016).

In this chapter, we show the three-dimensional (3D) displacements associated with the Kumamoto earthquakes derived by applying pixel tracking technique to ALOS-2/PALSAR-2 data. Using the derived pixel tracking data, we develop a fault slip distribution model based on triangular dislocation elements in an elastic half-space and discuss its implication for the rupture processes of the 2016 Kumamoto earthquakes.

6.2 Methods and results

We processed ALOS-2/PALSAR-2 data (L-band, wavelength is 23.6 cm) acquired from stripmap mode with HH polarization at three tracks (Figure 6-1; Table 6-1), using GAMMA software (Wegmüller & Werner, 1997). Because the InSAR data were missing near the faults due to the problem in phase unwrapping, we applied pixel tracking technique to ALOS-2/PALSAR-2 data so that we could detect robust signals even if the displacement gradient was high (Kobayashi et al., 2009; Takada et al., 2009; Tobita et al., 2001). We set the window size of 32 × 64 pixels for range and azimuth with the sampling interval of 12 × 24 pixels for range and azimuth, respectively. The processing strategy in this

study is mostly the same as our previous studies (Furuya and Yasuda 2011; Abe et al. 2013). The technique originates in the precision matching of multiple images, and the local deviations from globally matched image indicate the displacements. Pixel tracking technique allows us to detect both range offset and azimuth offset. The range offset is a projection of the 3D displacements onto the local look vector from the surface to the satellite, whereas the azimuth offset is a projection of the 3D displacements along the satellite flight direction. Using the 3 pairs of ALOS-2/PALSAR-2 data (Table 1), we could obtain six displacement data projected onto six different directions (Figure 6-2). We can

Table 6-1. PALSAR-2 dataset in this chapter.

Pair No.	Track	Orbit	Date (dd.mm.yyyy)	B_perp [m]	Pixel spacing [Ran., Az. (m)]
1	23	D	03.07.2016	-122.43	1.4, 2.1
			18.04.2016		
2	130	A	03.12.2015	-147.36	2.8, 3.0
			21.04.2016		
3	29	D	14.01.2015	5.15	1.4, 1.8
			20.04.2016		

B_perp: Perpendicular component of baseline between master and slave image.
Orbit: Satellite flight direction from ascending (A) and descending (D) track.
Pixel spacing: Spatial resolution for range (Ran.) and azimuth (Az.) direction.

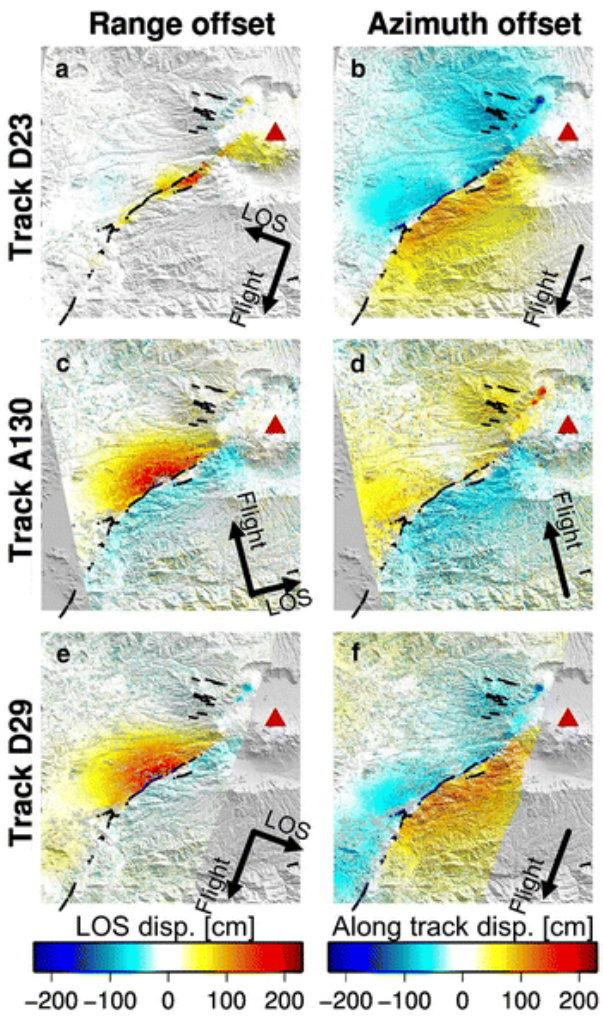


Figure 6-2. PALSAR-2 pixel tracking data which shows co-seismic displacement. (a, b) Track 23 observed from right-looking descending track. (c, d) Track 130 observed from right-looking ascending track. (e, f) Track 29 observed from left-looking descending track. Black arrows indicate each flight and line-of-sight (LOS) direction. Positive signals in range and azimuth offset show displacement along LOS away from the satellite and toward the satellite flight direction, respectively. Red triangles are the location of Mt. Aso. Black lines represent active fault traces derived from geological surveys (Nakata and Imaizumi, 2002).

identify three NE–SW trending signal discontinuities in the pixel tracking data (dotted curved lines in Figure 6-2), which we attribute to the surface faults due to the earthquake sequences and hereafter denote F1, F2 and F3, respectively. Geologically inferred fault traces by Nakata and Imaizumi (2002) are also shown in Figures 6-1 and 6-2. The longest discontinuity (NE–SW), F1, is located at a part of Futagawa fault system (Watanabe et al. 1979; Okubo and Shibuya 1993), extending from the northwestern area of the Aso caldera to Kumamoto City. Another signal discontinuity, F2, branches off from the southern part of the F1 toward SSW, which seems to be a part of Hinagu fault system (Watanabe et al. 1979). We can point out the other short signal discontinuity, F3, parallel to the F1 segment at the southwest flank of Aso caldera. The F3 segment is situated 2 km away from the longest F1 segment.

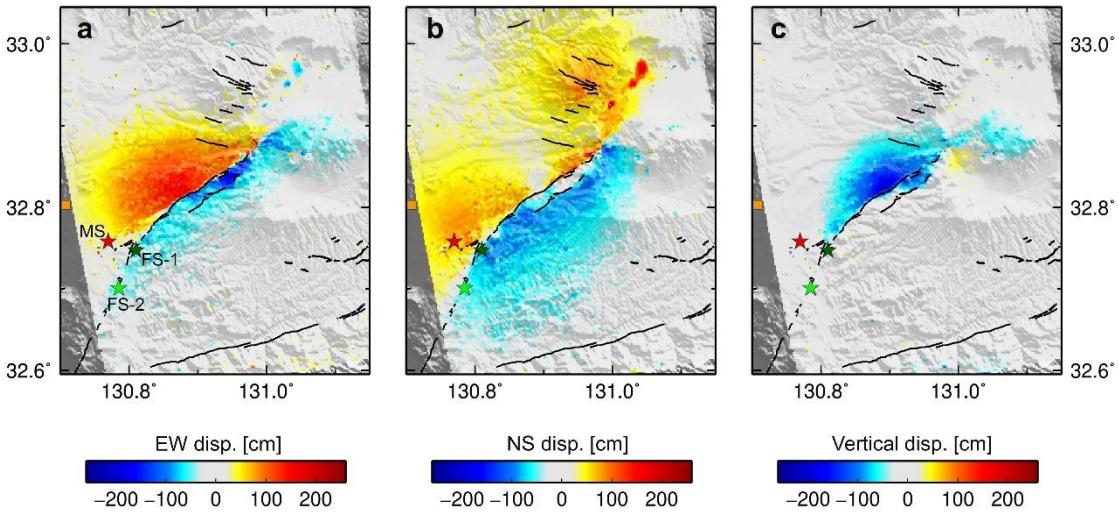


Figure 6-3. Cumulative 3D displacement inferred from our pixel tracking data of tracks 23 and 130. (a) East-west horizontal displacement, (b) North-south horizontal displacement, and (c) vertical displacement. Positive signals indicate eastward, northward, and uplift displacement, respectively. Black lines the Hinagu and Futagawa fault traces reported by Nakata and Imaizumi (2002). Black box shows the location of localized signal indicating NNE horizontal movement. Colored stars indicate the location of each centroid (Red: Mainshock, Strong and light green: Foreshocks (FS-1, FS-2)).

Based on these pixel tracking data, we derived the 3D displacement field from tracks 23 and 130 by solving an overdetermined least-squares problem without any weight functions (Figure 6-3). Although there are three available tracks, the data coverage becomes more limited when we use all the tracks (Figure 6-4), because we solved for the 3D displacement where the employed tracks are completely overlapped. Also, because the tracks 29 and 130 are viewing the surface from nearly the same look direction, we consider that the tracks 23 and 130 are the best combination to derive the 3D displacements. Considering the NE–SW striking of the F1 segment, the focal mechanism of the main shock (Mw 7.0) suggests mainly right-lateral motion with a near-vertical dip angle. Nonetheless, the northern side of the deformation area indicates significant subsidence by as much as ~200 cm (Figure 6-3). This subsidence signal can be explained by the normal faulting on NW-dipping segments, which would be plausible under the N–S extension stress field. In contrast, we could identify few uplift signals at the southern side. Besides the broadly distributed signals noted above, we can point out more

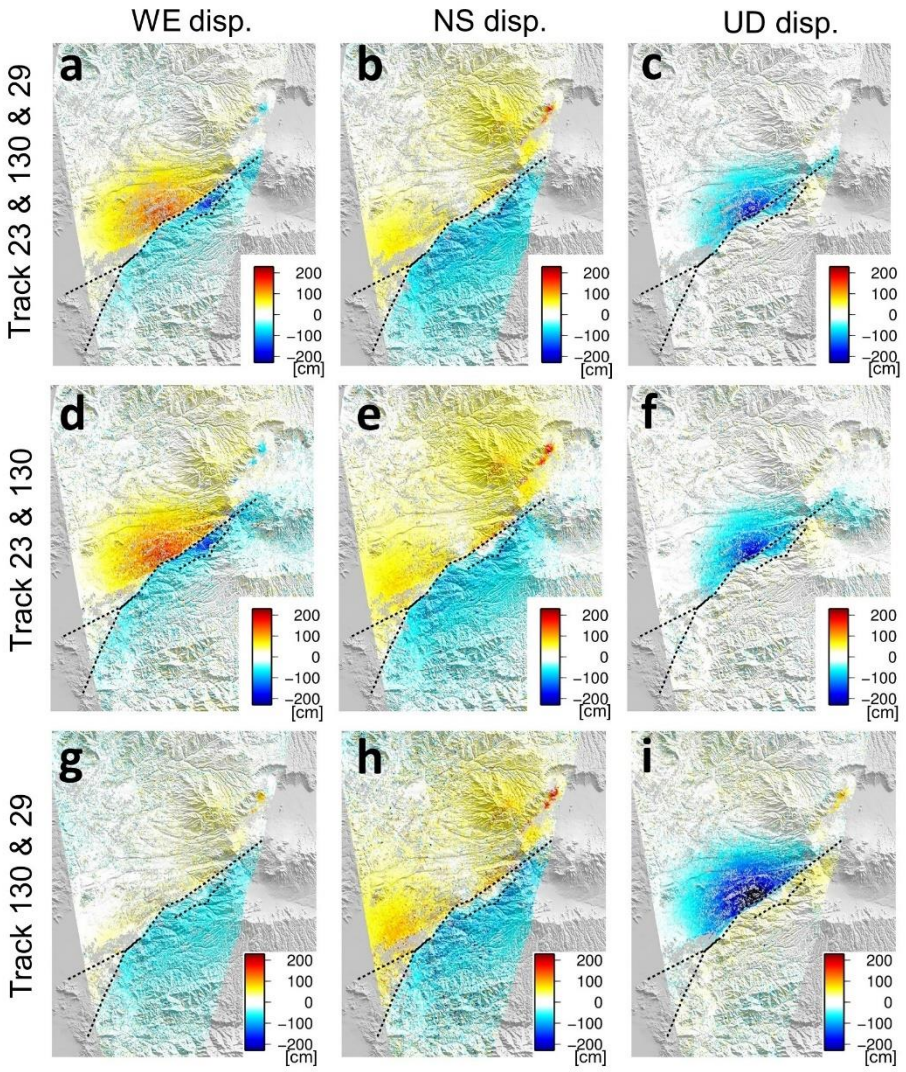


Figure 6-4. Comparison of cumulative 3D displacements inferred from three combination of PALSAR-2 pixel tracking data. The 3D displacement inferred from tracks 23, 130 and 29 (a-c), tracks 23 and 130 (d-f), and tracks 130 and 29 (g-i).

localized signals in places. We can identify the NE–SW trending patchy localized signals at the northern part of Aso caldera in the 3D displacement field (black boxes in Figure 6-3). These signals indicate ~200 cm of NNW movement with small vertical displacements. Moreover, the 3D displacements indicate subsidence signals by as much as 50 cm at the western part of Aso caldera, which is located at the eastern part of the deformation area. The detected subsidence signal significantly exceeds the empirical measurement error of pixel tracking which is 0.1 pixel in each image (e.g., Fialko et al. 2001). Moreover, the localized westward displacements can be found between

the two discontinuities (Figure 6-3a). These signals cannot be explained by the fault model below, and we provide our interpretations later on.

6.3 Fault source model

In this section, we present our fault model that can reproduce the pixel tracking data sets (Figure 6-2). Our model consists of three fault segments whose top positions trace the displacement discontinuities in the pixel tracking data (Figure 6-5). We also denote the three segments F1, F2 and F3, respectively. The bottom depths were set to be 20 km for F1 and F2 segments and 10 km for the F3 segment. Top depths of all segments are set to be surface. Each fault segment consists of triangular dislocation element, so that we can express the non-straight irregular fault trace as well as curved geometry; we use Gmsh software to construct triangular meshes (Geuzaine & Remacle, 2009). The actual parameterization of fault geometry was performed as follows: We firstly set the top locations of the faults by providing control points so that they can trace the displacement discontinuities in the observation data; shallowest part of the faults is thus non-planar. On the other hand, because of the lower resolution at greater depths, we assume that the deep part of these faults is essentially planar, and no control points for the fault plane at intermediate depths are given. The fault surface is derived by spline interpolation, based on the given control points on the top and the bottom. The location and depth of the bottom of the faults, i.e., dip angle, were derived by trial-and-error approach (Table 6-2; e.g., Furuya and Yasuda 2011; Abe et al. 2013). Based on the given location and geometry of the fault, we can solve the slip distributions as a linear problem with the constraints noted below. For the Green function, we use analytical solutions of surface displacements due to a triangular dislocation element in an elastic half-space (Meade, 2007). We assume Poisson ratio of 0.25 and crustal rigidity of 30 GPa.

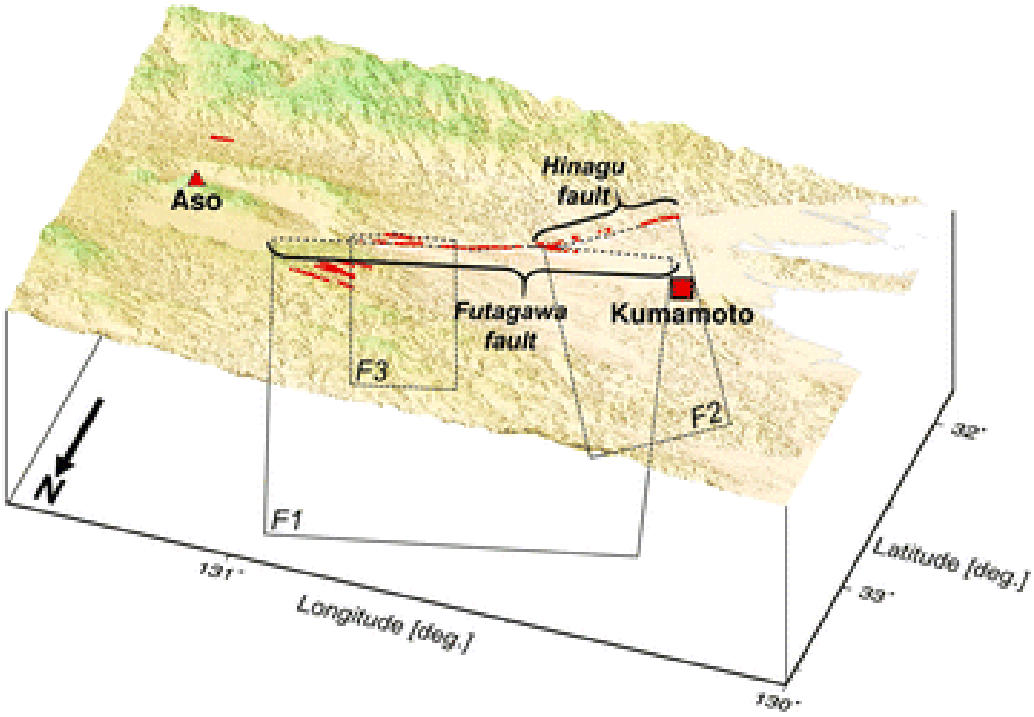


Figure 6-5. Schematic perspective of fault geometry of our inferred model viewing from NNE. Details of model parameter are shown in Table 2. Red lines indicate the traces of geological fault trace.

The size of a typical triangular mesh varies from the minimum (~1000 m) near the surface to the largest (~2000 m) toward the bottom of the segments because the resolution becomes worse at deeper depth. We applied median filter to the observed pixel tracking data to reduce noises. To invert for slip distributions on each segment that are physically plausible, we solve a non-negative least-squares problem that restricts the slip directions together with a constraint on the smoothness of the slip distributions (Furuya & Yasuda, 2011; Simons et al., 2002). Regarding the restrictions on the slip directions, whereas F1 was allowed to include both strike and normal slip, we further limited that F2 and F3 included only right-lateral and normal slip components, respectively. This is not only because we could reduce the number of degrees of freedom but also because the differences of the misfit residuals were insignificant even when we considered both slip components at F2 and F3. When F2 and F3 are allowed to include both slip components, the derived slip amplitude turned out to be less

than 15 cm. In deriving the slip distribution, we masked the before-mentioned patchy localized signals at the northern part of Aso caldera. Although the computed pixel tracking data from the estimated slip on the faults can mostly reproduce the observed displacement field, misfit residuals are still left around

Table 6-2. Parameters of our fault model

Segment No.	**F1**	**F2**	**F3**
Latitude [deg.]	32.82	32.77	32.82
Longitude [deg.]	130.87	130.81	130.93
Bottom [km]	20.0	20.0	10.0
Strike [deg.]	231.69	214.99	230.77
Dip [deg.]	78.69	86.51	65.61
Width [deg.]	20.0	20.0	
Length [km]	41.29	18.28	12.65
Slip constraint	Normal slip Right-lateral	Right-lateral	Normal slip
M_W (M_0 [Nm])	6.77 [1.80×10^{19}]	6.62 [1.05×10^{19}]	6.46 [0.61×10^{19}]

Latitude and Longitude present the center coordinates of top projection of faults. Slip indicates the direction of slip constraint on each fault segment. M_W is total geodetic moment release calculated by slip distribution. Top depth of all fault segments is located at surface [0 km].

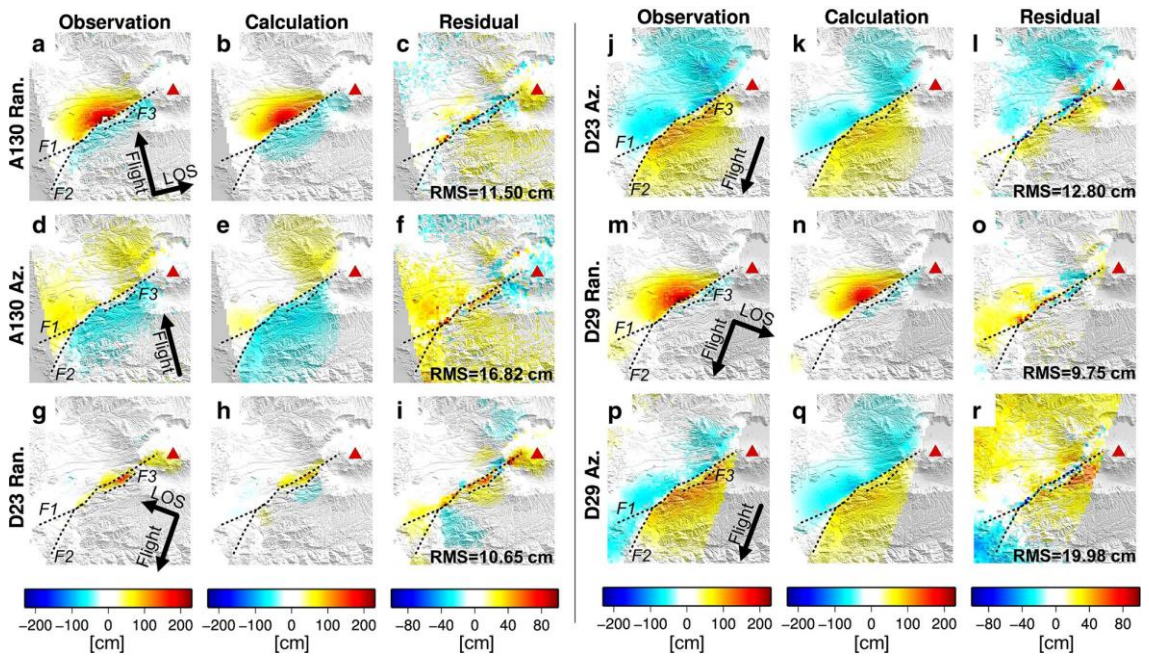


Figure 6-6. Comparison with observation of pixel-tracking data, calculation derived from our slip distribution and their residual. (a, d, g, j, m, p) Observations of pixel tracking data. (b, e, h, k, n, q) Calculated pixel tracking from our slip distribution on each segment. (c, f, i, l, o, r) Residual subtracted observation from calculation. Positive value in range offset and azimuth offset shows line-of-sight (LOS) increasing (moving away from satellite) and horizontal displacement moving toward the satellite flight direction, respectively. Color scales indicate displacement in centimeters. Red triangle marks location of Mt. Aso. Dashed lines trace the top location of the faults. Root mean square (RMS) are shown in each bottom right on residual framework.

the epicenter area, especially in the region between F1 and F3 (Figure 6-6); we discuss our interpretation later on. However, we do not further refine the fault model for now, because of the root-mean square (RMS) residual of each pixel tracking datum below 20 cm, which is largely comparable to the precisions of offset measurements (Kobayashi et al., 2009). Slip distributions in our model show the maximum right-lateral strike-slip of >5 m on F1 at a depth of 5 km and the maximum normal slip of 4.5 m on F3 at a depth of 6 km (Figure 6-7). Not only right-lateral slip but also normal slip (~2.5 m) is present on F1 segment. Because the depths of epicenters are located around 10 km according to JMA catalog, these slip distributions are nearly consistent with them. The 1-sigma uncertainties of slip distribution (Figure 6-8) were estimated from standard deviations of 200-times iterative inversions

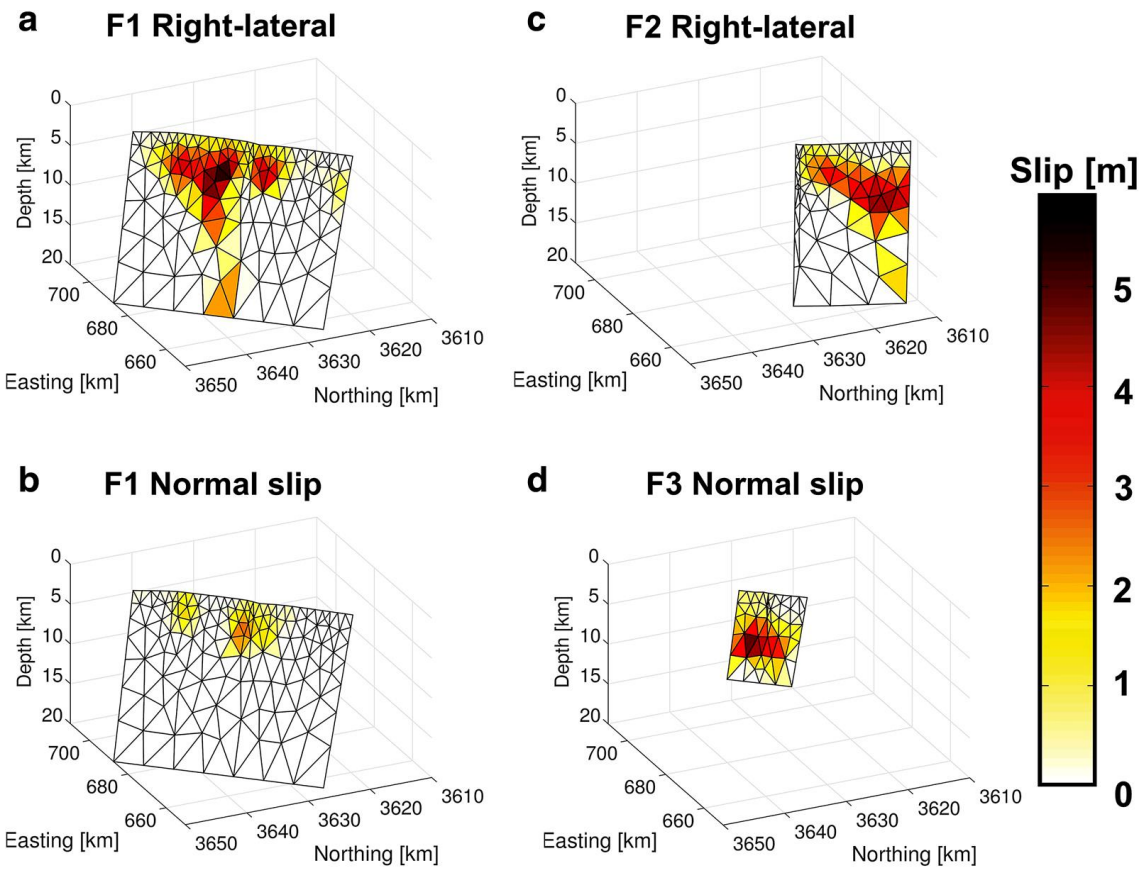


Figure 6-7. Slip distribution on each fault segment viewing from WNW. (a) Right-lateral slip on F1. (b) Normal slip on F1. (c) Right-lateral slip on F2. (d) Normal slip on F3. All figures are shown by same color scale in meters and are projected on same UTM (Universal Transverse Mercator) coordinate frame viewing from WNW (Zone 52).

with 2D correlated random noises (Furuya & Yasuda, 2011; Wright et al., 2003). Significant uncertainties are located at the lowest and side patches of fault elements, and the slip error is much less than the estimated slip amplitude. Total geodetic moment (GM) release in our fault model is 3.47 $\times 10^{19}$ Nm (Mw 6.96), whereas seismic moment (SM) of the main shock derived from JMA catalog is 4.06 $\times 10^{19}$ Nm (Mw 7.01) (Table 6-3). Although these moment release values seem to be nearly identical, we should note the differences in the details of each total moment (Table 6-3).

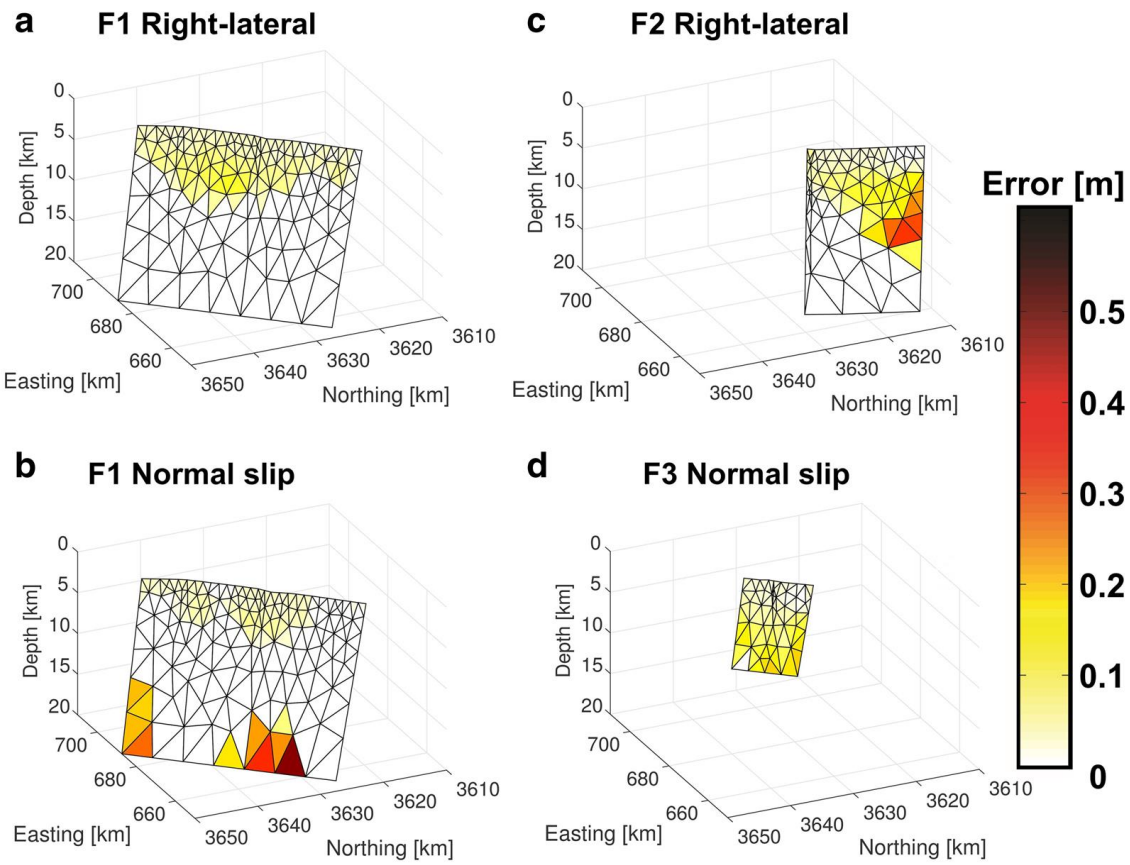


Figure 6-8. Slip 1-sigma uncertainties for each segment calculated by 200-times iteration of inversion with random noise. (a) Right-lateral slip on F1. (b) Normal slip on F1. (c) Right-lateral slip on F2. (d) Normal slip on F3. All figures are shown by same color scale in meters and are projected on same UTM coordinate frame (Zone 52).

6.4 Discussion

Remarkably, our fault model indicates that while the strike-slip dominates on F1 and F2, F3 is a pure normal slip fault (Figure 6-7; Table 6-3). The significant normal slip at F3 instead of at F1 could be derived, because the broad subsidence signals are located not only to the north of F1 but also between F1 and F3, and also because the deeper normal slip can explain the broader subsidence signals. Such a configuration of multiple faults is known as slip partitioning, which has been pointed out at active tectonic regions of oblique extension/compression stress regime (e.g., Bowman et al., 2003; Fitch, 1972). Our fault model thus suggests that the fault source regions are under oblique extension stress,

which is probably due to the combination of the shear stress by the western end of MTL and the extension stress associated with the backarc spreading of Okinawa trough (Nishimura and Hashimoto 2006; Ikeda et al. 2009; Matsumoto et al. 2015). Moreover, the deviation of a moment tensor from double couple, a so-called compensated linear vector dipole (CLVD) parameter ε, is 0.28 (JMA epicenter catalog); the ε could range from −0.5 to 0.5 and become zero for a perfect double couple. While a variety of interpretations on non-double couple components are possible (Julian et al., 1998), the moment tensor for the main shock by JMA provides us with such eigenvalues that can be decomposed into one normal faulting and one strike-slip earthquake on the assumption of no volume changes. Each moment release is shown in Table 6-3 as the SM, and the quoted moment by JMA is derived by $(\sigma 1 - \sigma 3)/2$, where σ1 and σ3 are the maximum and the minimum eigenvalues, respectively. Meanwhile, based on our slip distribution model, we computed the contribution from normal- and strike-slip faulting (Table 6-3) and the corresponding CLVD parameter (ε), and plotted the beach ball

Table 6-3. Total moment release derived from the inferred fault model (GM) and JMA catalog (SM).

			Slip component	M_0 [10^{19} Nm]	M_W
GM	Total			3.47	6.96
		F1	Right-lateral	1.76	7.76
			Normal slip	0.36	6.30
		F2	Right-lateral	1.05	6.62
		F3	Normal slip	0.61	6.46
SM	Total			4.06	7.01
			Right-lateral	3.40	6.95
			Normal slip	1.32	6.68

on the assumption of simultaneous rupture events (Figure 6-9). The ε turns out to be 0.26, and the synthetic beach ball is remarkably consistent with that by JMA (Figure 6-9). Therefore, independently from the JMA's moment tensor, the slip distributions at distinct segments in our fault model suggest that both normal faulting and strike-slip earthquakes have simultaneously occurred in a single event (Kawakatsu 1991; Kikuchi et al. 1993) and that no source volume changes occurred; we may call it dynamic slip partitioning. While Kawakatsu (1991) interpreted the non-double couple components in earthquakes at ridge-transform faults as simultaneous occurrence of both normal and strike-slip at transform faults, our fault model would be the first geodetic evidence for the simultaneous rupture hypothesis of non-double couple component with no volume changes. One of the possible explanations for the differences in the moment values of each slip type could be the mix-up of the two seismic waveforms of the main shock (M_W 7.0) and another event (M_{JMA} 5.7) that occurred after 32 s at Yufu City (Kato et al., 2016). However, it is also likely due to the simple assumption of homogeneous elastic body in the estimated geodetic moment. The patchy localized signals of the NNW horizontal movements (black boxes in Figure 6-3), which were masked in the inversion, would not be explained by co-seismic landslides, because directions of the local slope and the horizontal displacements are opposite. We can speculate that these localized signals may suggest the presence of additional small faults, because some faults inside a volcanic caldera are likely to be masked by the thick volcanic ash deposits. Regarding the localized westward signals between F1 and F3, it is possible to attribute to the left-lateral slip on F3. However, the inferred left-lateral strike-slip on F3 turned out to be insignificant as mentioned before; this may be because we used pixel tracking data for the inversion. Some reports of field-based surface rupture observations indicated left-lateral offsets near the southern end of F3; the strike angles were ~N70W (e.g., http://www.ckcnet.co.jp/pdf/kumamoto_0427.pdf, in Japanese). Given these reports and the modeling results, if the westward signals have their origin in faults, they may suggest the left-lateral faults in

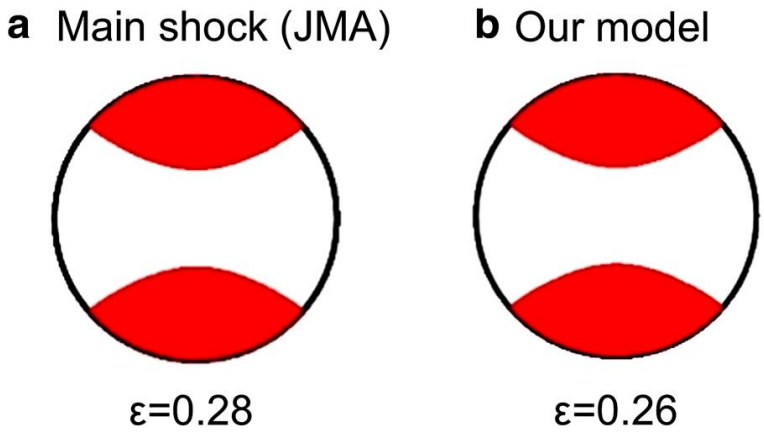


Figure 6-9. Focal mechanism of the mainshock during the episode derived from JMA catalog (a), and that derived from the inferred slip distribution (b). Both moment tensors are considered in arbitral coordinates. Deviations of moment tensor (ε) are shown below each beachball.

between F1 and F3 which strike ~N70W in a conjugate fashion. Although, to our knowledge, there are no reports of such seismic focal mechanisms, they might have occurred at very shallow depth without generating seismic waves. Another possible interpretation would be a co-seismic landslide; the local slop orientation seems to be consistent with this scenario. Furthermore, the 3D displacement showed ~50 cm subsidence at the western part of Mt. Aso (Figure 6-3c), which cannot be explained by our fault model. One possible interpretation of the subsidence signal at Mt. Aso is a consequence by extension of the magma chamber due to the westward movement by the right-lateral earthquakes, which is analogous to the subsidence as reported over the volcanoes on the northeastern Honshu after 2011 Tohoku-oki earthquake (Takada & Fukushima, 2013). However, while an effusive volcanic eruption with gas emission was observed after the main shock of the 2016 Kumamoto earthquake sequence, the casual relationship still remains unclear.

6.5 Post-seismic deformation revealed by PALSAR-2 data

We also show additional results, the post-seismic deformation associated with the 2016 Kumamoto earthquake detected by PALSAR-2 interferograms (Figures 6-11 and 6-12). Post-seismic deformations associated with earthquakes detected by InSAR have reported by lots of papers (e.g., Moore et al.,

2017). Generally, the post-seismic deformations are driven by after-slips and viscoelastic relaxation, the temporal evolution of post-seismic deformation can be expressed by logarithmic and exponential functions. Some previous studies have reported the far-field post-seismic deformations across Kyushu island revealed by GEONET GPS network and Sentinel-1A InSAR data, and their observations were modeled by the contributions of after-slip and viscoelastic relaxation (Kato et al., 2016; Moore et al., 2017; Pollitz et al., 2017). The post-seismic deformation near the surface ruptures appeared during the earthquake sequence has not been reported. Kato et al. (2016) reported that a campaign-based GPS measurement revealed 2-3 cm of horizontal displacement, however the observation stopped on May 2016. Moore et al. (2017) also reported the velocity of LOS change detected by Sentinel-1A dataset, although their observation period finished June 2016. According to their GPS and SAR measurements, the velocity of vertical displacement was inferred of 40 mm/yr (Moore et al., 2017). As of writing this thesis, we are expecting to detect the post-seismic deformation using satellite SAR data because SAR images are accumulating for over 2 years.

Sentinel-1 satellites have been observed with shorter acquisition intervals than PALSAR-2, however shorter wavelength microwaves are easier to cause decorrelation problem. Because most part of Kyushu island is covering with dense vegetation, longer wavelength microwave, such as PALSAR-2, is suitable for observing crustal deformation by InSAR. PALSAR-2 dataset and their footprints for detecting post-seismic deformations are shown in Table 6-4. We employed the conventional stacking approach to detect small crustal deformation and to mitigate artificial signal derived from tropospheric effects (e.g., Wright et al., 2001). Although we applied multiple aperture radar interferometry (MAI) approach to PALSAR-2 dataset, we could not distinguish significant deformation signal from the decorrelation noise. After PALSAR-2 interferograms were stacked, we decomposed quasi-eastwest (QEW) and quasi-vertical (QUD) displacements using stacked PALSAR-2 interferograms

Table 6-4. PALSAR-2 dataset for detecting the post-seismic deformation

Track	Acquisition date [dd.mm.yyyy]	B_perp [m]
A130	21.04.2016	0
	05.05.2016	57.3
	11.08.2016	136.9
	13.07.2017	90.1
	05.10.2017	215.1
A131	26.04.2016	0
	10.05.2016	362.1
	19.07.2016	191.9
	06.12.2016	389.6
	14.03.2017	116.5
	13.02.2018	287.3
	03.07.2018	296.7
	28.08.2018	222.5
D20	17.04.2016	0
	01.05.2016	90.9
	09.07.2017	46.2
	17.09.2017	-81.4

Track	Acquisition date [dd.mm.yyyy]	B_perp [m]
D23	18.04.2016	0
	16.05.2016	246.1
	13.06.2016	-38.7
	11.07.2016	21.1
	08.08.2016	-5.7
	19.09.2016	-114.5
	14.11.2016	-160.6
	13.11.2017	2.7
	05.03.2018	336.8
	20.08.2018	-52.4
	15.10.2018	-126.1

Track indicates the identification orbit numbers. All images are acquired from a right-looking geometry. *B_perp* indicates the perpendicular component of spatial baseline between two SAR images. Each *B_perp* value is shown with a reference of a first image.

observed from ascending and descending tracks with assuming few north-southward sensitivity in InSAR (Fujiwara et al., 2000). We processed PALSAR-2 images acquired from two independent ascending tracks (Track 130 and 131) and two descending track (Track 23) by using GAMMA software. We employed an adaptive filter with a parameter of 0.6 and a window size of 32 pixels to avoid phase unwrapping error (Goldstein & Werner, 1998). The interferograms were unwrapped phase using minimum cost flow algorithm (Costantini, 1998). Topography-corrected signals were corrected by the 10 m digital elevation model (DEM) which is provided by the Geospatial Information Authority in Japan. Long wavelength phase changes across the data were corrected by fitting 2D polynomial functions.

Figure 6-11 shows cumulative LOS changes revealed by stacked PALSAR-2 interferogram

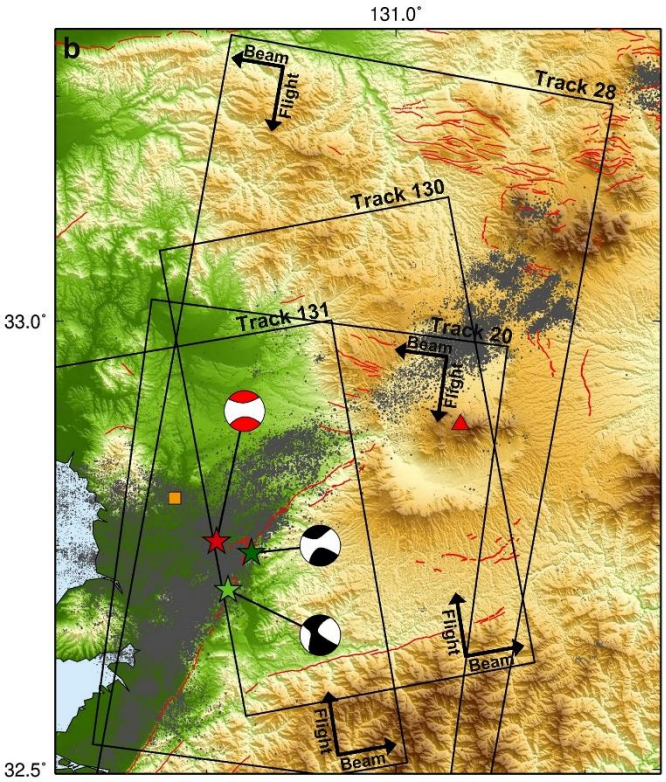


Figure 6-10. Study area and PALSAR-2 footprints for detecting post-seismic crustal deformation. Red lines mark active fault traces inferred by geological survey (Nakata and Imaizumi, 2002). Black boxes indicate coverages of PALSAR-2 image. Colored stars locate epicenters in the mainshock (red), and two foreshocks (green). Beach balls are focal mechanisms of each event. Grey dots represent a distribution of epicenters during 14-30 April 2014. Information of earthquake are derived from Japan Meteorological Agency catalog. Red triangle marks Aso volcano.

after the earthquake sequence for over one year. The cumulative LOS changes show signal discontinuities along the geological fault traces reported by Nakata and Imaizumi (2002) (Black lines in Figure 6-11). The descending interferogram shows +12 cm of maximum LOS change along the Futagawa fault where we set the top locations of F1 and F3 in our model, and the zonal positive signal is observed along the Futagawa fault toward SW (Figure 6-11b). Both outside of the zonal positive signal represents negative signal, although the signal sign changes across the surface rupture along the Futagawa fault. Another signal characteristic is that ~10 cm of positive signal broadly distributes across Aso caldera. The two-independent stacked-interferograms observed from ascending track show

similar signal characteristics, although the observation period in Track 130 is 10 months shorter than that in Track 131. We found significant a signal discontinuity along the Hinagu fault, and ~ 10 cm of negative signal near the northeastern part of Futagawa fault. To understand the detail description of the post-seismic deformation, we infer the QEW and QUD displacements, named the 2.5-dimensional analysis (Fujiwara et al., 2000). We inferred two independent QEW and QEW displacements using pairs of Track A130 and D23 (Figures 6-12a and 6-12b), and Track A131 and D23 (Figures 6-11c and 6-11d) for compensating sensitivity of LOS change, because each incidence angles are different. Same signal characteristics between each analysis data would be plausible, while differences of signal characteristics can be artificial error induced by residuals of correcting tropospheric artifacts and long wavelength signal. Above the Aso caldera, westward displacements with a NE-SW signal discontinuity at the northwest part of the Aso caldera and subsidence at the west part of the caldera were observed. The NE-SW signal discontinuity was also observed in the co-seismic displacement. Although the subsidence around the summit of Mt. Aso was also detected in the co-seismic deformation, we can find patch-shaped subsidence signals at the northwestern rim of the caldera in Figure 6-11b. The co-seismic deformation represented the similar distribution of horizontal displacement with few vertical displacements there (Figure 6-3c). At outside of the southwestern part of the Aso caldera, ~10 cm of uplift is distributed in the QUD displacement (Figures 6-12b and 6-12d). The co-seismic deformation detected few uplifts across the Futagawa fault and significant subsidence at the northern half of the displacement field. We also find that a zonal subsidence is extending toward southwest along the Futagawa fault and that a branch of zonal subsidence is distributed toward Kumamoto city. On the other hands, the QEW displacements show the similar trends of the co-seismic displacement, indicating eastward displacement at the north side across the fault trace and westward displacement at the detachment between Futagawa and Idenokuchi fault. We also find ENE-WSW discontinuity of westward movement at the southern part of the displacement field.

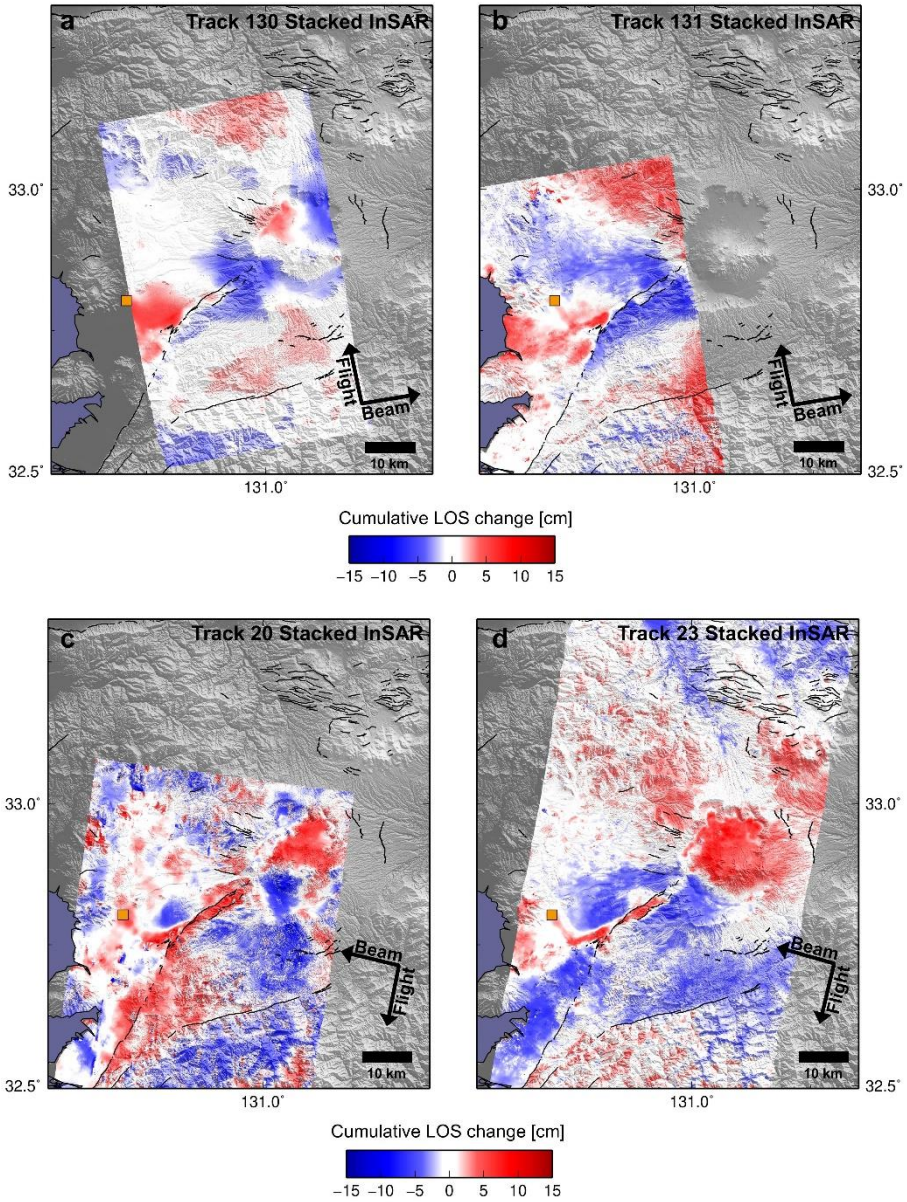


Figure 6-11. Stacked PALSAR-2 InSAR after the mainshock. Cumulative LOS changes derived from the conventional InSAr stacking approach in Track 20 (a), Track 23 (b), Track 130 (c), and Track 131 (d), respectively. Positive signal indicates LOS lengthening, indicating displacements away from the satellite. Black solid lines show geological traces of active faults reported by Nakata and Imaizumi (2002). Orange box is the location of Kumamoto city.

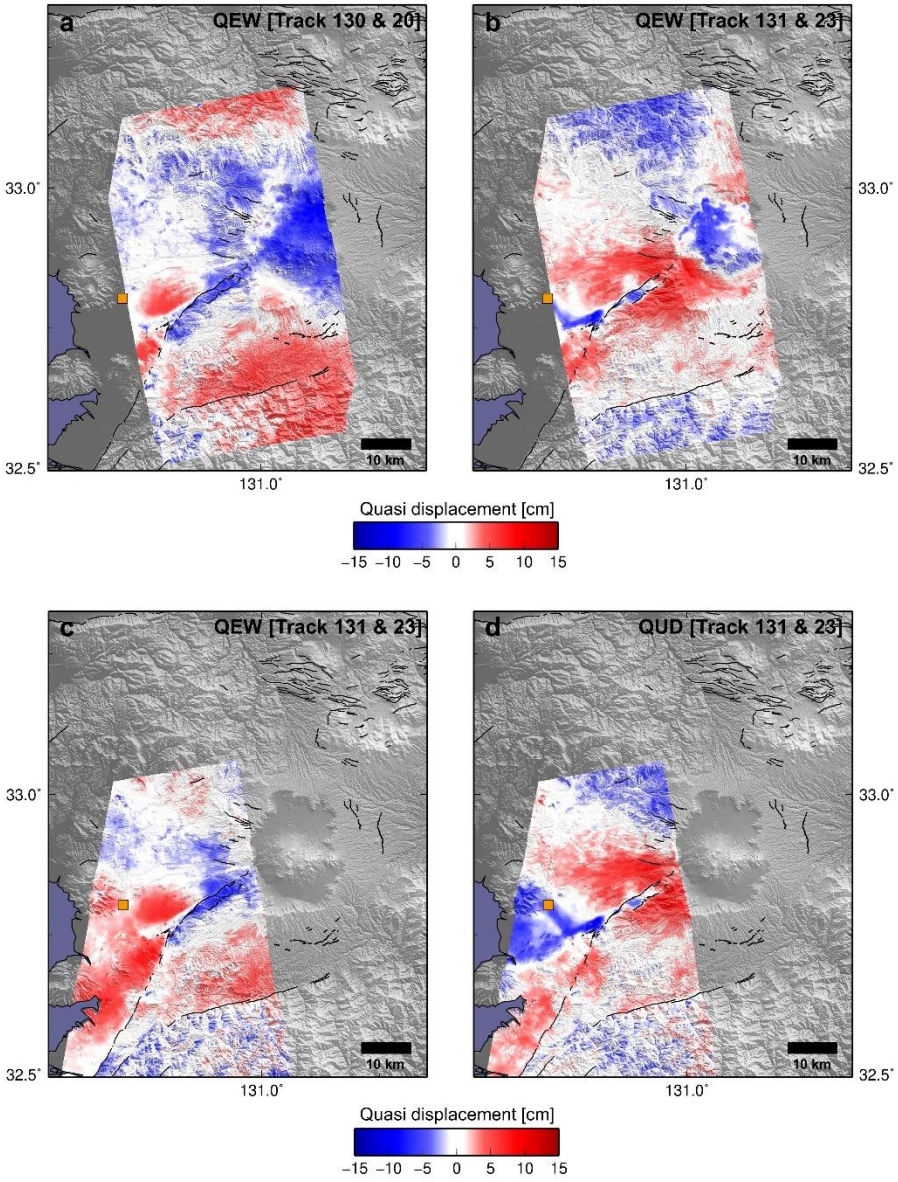


Figure 6-12. Cumulative quasi-displacements derived from the stacked PALSAR-2 interferograms. (a) Quasi-eastwest and (b) Quasi-vertical displacements inferred from the Track 20 and 130 InSAR. (c) Quasi-eastwest and (d) Quasi-vertical displacements inferred from Track 23 and 131 InSAR, respectively. Positive signals indicate quasi-eastward displacements and quasi-uplift displacements, respectively. Details are same in Figure 6-11.

Chapter 7

Thesis Findings and Conclusions

Chapter 7. Thesis findings and conclusions

This thesis has reported the crustal deformations revealed by satellite SAR data and their elastic models associated with three dike intrusions and one earthquake episode. We confirmed that most of episodes in this thesis occurred along the subaerial rifts and at shallower depths of crust. The observed crustal deformations induced surface break formations, indicating dislocations at the shallowest part of faults. Although InSAR is the most famous SAR analysis method for mapping crustal deformations with high measurement accuracy, revealing crustal deformations around surface ruptures derived from InSAR is challenging for now because of decorrelation problems. The decorrelation problems usually induce missing data around surface ruptures, we lose some pieces of important information of crustal deformation associated with the episode. In this thesis, we confirmed that the pixel tracking data depicted robust deformation signals associated with the 2005 Afar dike intrusion episode, the 2014-2015 Bárðarbunga dike intrusion episode, and the 2016 Kumamoto earthquake sequence comparing with the InSAR data for each episode. Although the interferograms for each episode showed missing data around the surface ruptures due to decorrelation problems, the pixel tracking data revealed the robust deformation signals with fewer missing data. Therefore we can conclude through this thesis that the cross-correlation-based pixel tracking approach would be suitable for detecting crustal deformation with fewer missing data, if the crustal deformation whose scale is greater than 1/10 pixels of spatial resolution of SAR images contains significant surface ruptures. Of course the pixel tracking is not completely utility SAR analysis method for detecting surface movement even if the scale of surface movement is greater than one meter as we faced the issue in Chapter 5. We challenged to infer the subglacial crustal deformation from icecap surface movements associated with the subglacial dike intrusion. The pixel tracking identified correlated signals only at the edge of icecap, could not at the higher part of icecap and around the Bárðarbunga caldera, although we tried parameters, such as

thresholds of cross-correlation and window size, for identifying plausible signals. Because the method is usually applied for estimating glacier flow velocity, we at first expected the signal could be detected by the pixel tracking, however, we could not be detected. The reasons are discussed in the discussion part in Chapter 5, but we might need to consider more for avoiding the induced decorrelation problems.

Concluding remarks for each episode are as follow.

In chapter 3, we detected the crustal deformation associated with the 2007 Natron dike intrusion episode in Tanzania using PALSAR-1 data. In addition to the two-pass InSAR data from both ascending and descending paths, we derived azimuth offset data that are sensitive to the displacements parallel to the satellite flight direction. We could thus demonstrate the 3D displacement fields. Besides the graben-like structure already pointed out in the previous studies, the 3D displacement fields indicate that the subsidence zone moved toward SSW. Our fault source model consists of one tensile-opening fault, one east-dipping fault, and two west-dipping faults. One notable difference of our fault model from previous studies is the presence of strike–slip component that turns to contribute to approximately 20% of the whole moment release. Because the focal mechanisms of the earthquakes during the 2007 swarm event represent nearly pure normal faulting, we consider that aseismic strike–slip on the faults is responsible for the horizontal movement of the subsidence zone.

In chapter 4, the post-2007 PALSAR pixel-offset and MAI data detected block-like horizontal displacements parallel to the rift axis on the graben floor by as much as ~1 m during the 2005-2010 Afar rifting episode. Our elastic fault model could reproduce the rift-parallel displacements by aseismic strike-slip on the graben-bounding faults. Stepping away from the elastic dislocation model and following the rheologically consistent numerical model of plume-lithosphere interaction, we may speculate that the rift-parallel displacements in both Natron and Afar rifting episodes could

be passive response of the upper crust to the underlying horizontal sill-like flow of plume material.

In chapter 5, we evaluated the possibility of isolating subglacial crustal deformations due to the dike intrusion under an icecap using satellite SAR data. The CSK, TSX, and RS2 pixel tracking results revealed both the ice flow and crustal deformations associated with the Bárðarbunga dike intrusion episode in 2014. The subglacial crustal deformations were inferred by correcting the icecap signal, by subtracting the scaled pre-diking signals from the co-diking signals. The icecap signals were corrected well in terms of the range offset, while some residuals remained in the azimuth offset. Our optimal elastic model without shearing along the dike could not reproduce the ice-corrected signals at the southern part of the dike completely, however, comparison of models with and without input data above the icecap confirmed that the ice-corrected signals improved the elastic model with dike opening and fault slip effectively. We expect that the SAR pixel tracking depicts crustal deformations associated with subglacial eruptions and/or subglacial dike intrusions in the Polar regions and/or at high altitude regions where ice covers, as we showed above.

In chapter 6, the results of pixel tracking applied to ALOS-2/PALSAR-2 data indicated three displacement discontinuities that were considered as the surface traces of the main source faults associated with the 2016 Kumamoto earthquake sequence. We thus constructed a fault slip distribution model containing three segments: F1 and F3 belong to the Futagawa fault system, and F2 belongs to the Hinagu fault system. The inferred slip distributions at each segment indicate that while the strike-slip is dominant at shallower depths of F1 and F2, only normal faulting is significant at greater depth of F3, suggesting the occurrence of slip partitioning during the earthquake sequence. Moreover, using our slip distribution, we computed the focal mechanism and the CLVD parameter, which turned out to be quite consistent with those derived from the seismic focal mechanism. Hence, we conclude that the

significant non-double couple components in the reported seismic focal mechanisms were due to the dynamic slip partitioning by simultaneous occurrence of both strike-slip and normal slip at the distinct segments. We also reported the post-seismic deformation until October 2018 revealed by the conventional stacking for PALSAR-2 interferograms.

The pixel tracking which strongly depends on image spatial resolutions had been recognized that the measurement accuracy of the data is worse comparing with that of InSAR data. However, we expect to improve the measurement accuracy of the pixel tracking because the spatial resolution of recent satellite SAR data is getting finer. While main topics in this thesis focus on only the co-seismic and co-diking crustal deformations at the subaerial rifts, the time-series analysis can reveal long-lasting deformations after the episodes due to the post-seismic and the post-diking processes, such as after-slip, viscoelastic relaxation, and aseismic magma intrusions. These processes are also helpful to understand strain fields and inhomogeneous structures at rift zones.

Bibliography

Abe, T., Furuya M., Takada Y. (2013). Nonplanar fault source modeling of the 2008 Iwate-Miyagi inland earthquake (MW 6.9) in Northeast Japan. Bulletin of the Seismological Society of America, 103, 507-518.

Ágústsdóttir, T., Woods, J., Greenfield, T., Green, R. G., White, R. S., Winder, T., et al. (2016). Strike-slip Faulting During the 2014 Bárðarbunga-Holuhraun Dike Intrusion, Central Iceland. *Geophysical Research Letters*, *43*, 1–9.

Albaric, J., Perrot, J., Déverchère, J., Deschamps, A., Le Gall, B., Ferdinand, R. W., et al. (2010). Contrasted seismogenic and rheological behaviours from shallow and deep earthquake sequences in the North Tanzanian Divergence, East Africa. *Journal of African Earth Sciences*, *58*(5), 799–811.

Albers, M., & Christensen, U. R. (2001). Channeling of plume flow beneath mid-ocean ridges. *Earth and Planetary Science Letters*, *187*, 207–220.

Amer, R., Mohamed, S., Robert, R., & John, E. (2012). Structural architecture for development of marginal extensional sub-basins in the Red Sea Active Rift Zone. *International Journal of Geoscience*, *2012*(February), 133–152.

Antonello, G., Casagli, N., Farina, P., Leva, D., Nico, G., Sieber, A. J., & Tarchi, D. (2004). Ground-based SAR interferometry for monitoring mass movements. *Landslides*, *1*(1), 21–28.

Aoki, Y. (1999). Imaging Magma Transport During the 1997 Seismic Swarm off the Izu Peninsula, Japan. *Science*, *286*(5441), 927–930. Retrieved from

Baer, G., & Hamiel, Y. (2010). Form and growth of an embryonic continental rift: InSAR observations and modelling of the 2009 western Arabia rifting episode. *Geophysical Journal International*, *182*, 155–167. https://doi.org/10.1111/j.1365-246X.2010.04627.x

Baer, G., Hamiel, Y., Shamir, G., & Nof, R. (2008). Evolution of a magma-driven earthquake swarm and triggering of the nearby Oldoinyo Lengai eruption, as resolved by InSAR, ground observations and elastic modeling, East African Rift, 2007. *Earth and Planetary Science Letters*, *272*(1–2), 339–352.

Baran, I., Stewart, M., & Claessens, S. (2005). A new functional model for determining minimum and maximum detectable deformation gradient resolved by satellite radar interferometry. *IEEE Transactions on Geoscience and Remote Sensing*, *43*(4), 675–682.

Bastow, I. D., Nyblade, A. A., Stuart, G. W., Rooney, T. O., & Benoit, M. H. (2008). Upper mantle seismic structure beneath the Ethiopian hot spot: Rifting at the edge of the African low-velocity anomaly. *Geochemistry, Geophysics, Geosystems*, *9*(12).

Bechor, N. B. D., & Zebker, H. A. (2006). Measuring two-dimensional movements using a single InSAR pair. *Geophysical Research Letters*, *33*(16), L16311.

Belachew, M., Ebinger, C., & Coté, D. (2013). Source mechanisms of dike-induced earthquakes in the dabbahu-Manda Hararo rift segment in Afar, Ethiopia: Implications for faulting above dikes.

Geophysical Journal International, *192*(3), 907–917.

Berardino, P., Fornaro, G., Lanari, R., & Sansosti, E. (2002). A new algorithm for surface deformation monitoring based on small baseline differential SAR interferograms. *IEEE Transactions on Geoscience and Remote Sensing*, *40*(11), 2375–2383.

Biggs, J., Amelung, F., Gourmelen, N., Dixon, T. H., & Kim, S. (2009). InSAR observations of 2007 Tanzania rifting episode reveal mixed fault and dyke extension in an immature continental rift. *Geophysical Journal International*, *179*(1), 549–558.

Bird, P., An updated digital model of plate boundaries, Geochemistry Geophysics Geosystems,4(3), 1027, doi:10.1029/2001GC000252, 2003.

Bjornsson, H., & Einarsson, P. (1990). Volcanoes beneath Vatnajokull, Iceland: Evidence from radio echo-sounding, earthquakes and jokulhlaups. *Jokull*, *40*, 147–167.

Bowman, D., King, G., & Tapponnier, P. (2003). Slip partitioning by elastoplastic propagation of oblique slip at depth. *Science*, *300*(5622), 1121–1123.

Brcic, R., Parizzi, A., Eineder, M., Bamler, R., & Meyer, F. (2010). Estimation and compensation of ionospheric delay for SAR interferometry. *International Geoscience and Remote Sensing Symposium (IGARSS)*, (3), 2908–2911.

Calais, E., D'Oreye, N., Albaric, J., Deschamps, A., Delvaux, D., Déverchère, J., et al. (2008). Strain accommodation by slow slip and dyking in a youthful continental rift, East Africa. *Nature*, *456*(7223), 783–788.

Casu, F., & Manconi, A. (2016). Four-dimensional surface evolution of active rifting from spaceborne SAR data. *Geosphere*, *12*(3), 697–705.

Chorowicz, J. (2005). The East African rift system. *Journal of African Earth Sciences*, *43*, 379–410.

Commins, D., Gupta, S., & Cartwright, J. (2005). Deformed streams reveal growth and linkage of a normal fault array in the Canyonlands graben, Utah. *Geological Society of America*, *33*(8), 645–648.

Coffin, M.F., Gahagan, L.M., and Lawver, L.A., 1998, Present-day Plate Boundary Digital Data Compilation. University of Texas Institute for Geophysics Technical Report No. 174, pp. 5.

Costantini, M. (1998). A novel phase unwrapping method based on network programming. *Geoscience and Remote Sensing, IEEE Transactions On*, *36*(3), 813–821.

Crider, J. G., & Pollard, D. D. (1998). Fault linkage: Three-dimensional mechanical interaction between echelon normal faults. *Journal of Geophysical Research*, *103*(B10), 24373–24391.

Delvaux, D., & Barth, A. (2010). African stress pattern from formal inversion of focal mechanism data. *Tectonophysics*, *482*, 105–128.

DeMets, C., Gordon, R. G., & Argus, D. F. (2010). Geologically current plate motions. *Geophysical Journal International*, *181*(1), 1–80.

Dieterich, J. H. (1979). Modeling of rock friction: 1. Experimental results and constituve equations.

Journal of Geophysical Research, *84*(9), 2161–2168.

Drouin, V., Sigmundsson, F., Ófeigsson, B. G., Hreinsdóttir, S., Sturkell, E., & Einarsson, P. (2017). Deformation in the Northern Volcanic Zone of Iceland 2008–2014: An interplay of tectonic, magmatic, and glacial isostatic deformation. *Journal of Geophysical Research: Solid Earth*, *122*(4), 3158–3178.

Ebinger, C. (1989). Tectonic development of the western branch of the East African rift system. *Geological Society of America Bulletin*, (7).

Ebinger, C., Ayele, A., Keir, D., Rowland, J., Yirgu, G., Wright, T., et al. (2010). Length and timescales of rift faulting and magma intrusion: the Afar Rifting Cycle from 2005 to present. *Annual Review of Earth and Planetary Sciences*, *38*, 439–466.

Ehara, S. (1992). Thermal structure beneath Kuju, central Kyushu, Japan. Journal of Volcanology and Geothermal Research, 54, 107-115.

Eibl, E. P. S., Bean, C. J., Vogfjörd, K. S., Ying, Y., Lokmer, I., Möllhoff, M., & Palsson, F. (2016). Silent Magma Flow Follows Tremor-rich shallow dyke formation: Bárdarbunga eruption, Iceland. *Nature Geoscience*, (April).

Fahnestock, M., Scambos, T., Moon, T., Gardner, A., Haran, T., & Klinger, M. (2016). Rapid large-area mapping of ice flow using Landsat 8. *Remote Sensing of Environment*, *185*, 84–94.

Farr, T. G., Rosen, P., Caro, E., & Crippen, R. (2007). The shuttle radar topography mission. *Reviews of Geophysics*, *45*(2004), 1–33.

Ferretti, A., Prati, C., & Rocca, F. (2000). Nonlinear subsidence rate estimation using permanent scatterers in differential SAR interferometry. *IEEE Transactions on Geoscience and Remote Sensing*, *38*(5), 2202–2212.

Ferretti, A., Prati, C., & Rocca, F. (2001). Permanent scatterers in SAR interferometry. *IEEE Transactions on Geoscience and Remote Sensing*, *39*(1), 8–20.

Fialko, Y., Khazan, Y., & Simons, M. (2001). Deformation due to a pressurized horizontal circular crack in an elastic half-space, with applications to volcano geodesy. *Geophysical Journal International*, *146*(1), 181–190.

Fitch, T. J. (1972). Plate convergence, transcurrent faults, and internal deformation adjacent to Southeast Asia and the western Pacific. *Journal of Geophysical Research*, *77*(23), 4432–4460.

Fujiwara, S., Nishimura, T., Murakami, M., Nakagawa, H., Tobita, M., & Rosen, P. a. (2000). 2.5-D surface deformation of M6.1 earthquake near Mt Iwate detected by SAR interferometry. *Geophysical Research Letters*, *27*(14), 2049–2052.

Fukuda, Y., Itahara, M., Kusumoto, S., Higashi, T., Takemura, K., Mawatari, H., et al. (2000). Crustal movements around the Beppu Bay area, East-Central Kyushu, Japan, observed by GPS 1996-1998. *Earth, Planets and Space*, *52*, 979–984.

Fukushima, Y., Cayol, V., Durand, P., & Massonnet, D. (2010). Evolution of magma conduits during the

1998–2000 eruptions of Piton de la Fournaise volcano, Réunion Island. *Journal of Geophysical Research*, *115*(B10), B10204.

Furuya, M., & Yasuda, T. (2011). The 2008 Yutian normal faulting earthquake (Mw 7.1), NW Tibet: Non-planar fault modeling and implications for the Karakax Fault. *Tectonophysics*, *511*(3–4), 125–133.

Furuya, M., Suzuki, T., Maeda, J., & Heki, K. (2017). Midlatitude sporadic-E episodes viewed by L-band split-spectrum InSAR. *Earth, Planets and Space*, *69*(1), 175.

Galeczka, I., Sigurdsson, G., Eiriksdottir, E. S., Oelkers, E. H., & Gislason, S. R. (2016). The chemical composition of rivers and snow affected by the 2014/2015 Bárdarbunga eruption, Iceland. *Journal of Volcanology and Geothermal Research*, *316*, 101–119.

Geuzaine, C., & Remacle, J.-F. (2009). Gmsh: A 3-D finite element mesh generator with built-in pre- and post-processing facilities. *International Journal for Numerical Methods in Engineering*, *79*(11), 1309–1331.

Goldstein, R. M., & Werner, C. L. (1998). Radar interferogram filtering for geophysical applications. *Geophysical Research Letters*, *25*(21), 4035.

Goldstein, R. M., Zebker, H. a., & Werner, C. L. (1988). Satellite radar interferometry: Two-dimensional phase unwrapping. *Radio Science*, *23*(4), 713–720.

Gomba, G., Parizzi, A., De Zan, F., Eineder, M., & Bamler, R. (2016). Toward operational compensation of ionospheric effects in SAR interferograms: The split-spectrum method. *IEEE Transactions on Geoscience and Remote Sensing*, *54*(3), 1446–1461.

Grandin, R., Socquet, A., Binet, R., Klinger, Y., Jacques, E., De Chabalier, J. B., et al. (2009). September 2005 Manda hararo-dabbahu rifting event, Afar (Ethiopia): Constraints provided by geodetic data. *Journal of Geophysical Research*, *114*, B08404.

Grandin, R., Socquet, A., Jacques, E., Mazzoni, N., de Chabalier, J.-B., & King, G. C. P. (2010). Sequence of rifting in Afar, Manda-Hararo rift, Ethiopia, 2005–2009: Time-space evolution and interactions between dikes from interferometric synthetic aperture radar and static stress change modeling. *Journal of Geophysical Research*, *115*, B10413.

Grandin, R., Socquet, a., Doin, M. P., Jacques, E., De Chabalier, J. B., & King, G. C. P. (2010). Transient rift opening in response to multiple dike injections in the Manda Hararo rift (Afar, Ethiopia) imaged by time-dependent elastic inversion of interferometric synthetic aperture radar data. *Journal of Geophysical Research: Solid Earth*, *115*(September 2005).

Gray, A. L., Mattar, K. E., & Sofko, G. (2000). Influence of ionospheric electron density fluctuations on satellite radar interferometry. *Geophysical Research Letters*, *27*(10), 1451–1454.

Green, R. G., White, R. S., & Greenfield, T. (2014). Motion in the north Iceland volcanic rift zone accommodated by bookshelf faulting. *Nature Geoscience*, *7*(1), 29–33.

Gudmundsson, M. T., Sigmundsson, F., & Björnsson, H. (1997). Ice–volcano interaction of the 1996

Gjálp subglacial eruption, Vatnajökull, Iceland. *Nature*, *389*(October), 954–957.

Gudmundsson, M. T., Jónsdóttir, K., Hooper, A., Holohan, E. P., Halldórsson, S. A., Ófeigsson, B. G., et al. (2016). Gradual caldera collapse at Bárdarbunga volcano, Iceland, regulated by lateral magma outflow. *Science*, *353*(6296), aaf8988.

Hamling, I. J., Ayele, A., Bennati, L., Calais, E., Ebinger, C. J., Keir, D., et al. (2009). Geodetic observations of the ongoing Dabbahu rifting episode: new dyke intrusions in 2006 and 2007. *Geophysical Journal International*, *178*, 989–1003.

Hamling, I. J., Wright, T. J., Calais, E., Bennati, L., & Lewi, E. (2010). Stress transfer between thirteen successive dyke intrusions in Ethiopia. *Nature Geoscience*, *3*(10), 806–806.

Hamling, I. J., Wright, T. J., Calais, E., Lewi, E., & Fukahata, Y. (2014). InSAR observations of post-rifting deformation around the Dabbahu rift segment, Afar, Ethiopia. *Geophysical Journal International*, *197*(1), 33–49.

Hammond, J. O. S., Kendall, J.-M., Stuart, G. W., Keir, D., Ebinger, C., Ayele, A., & Belachew, M. (2011). The nature of the crust beneath the Afar triple junction: Evidence from receiver functions. *Geochemistry, Geophysics, Geosystems*, *12*(12), n/a-n/a.

Hanssen, R. F., Feijt, A. J., & Klees, R. (2001). Comparison of precipitable water vapor observations by spaceborne radar interferometry and meteosat 6.7-µm radiometry. *Journal of Atmospheric and Oceanic Technology*, *18*(5), 756–764.

Heimisson, E. R., Hooper, A., & Sigmundsson, F. (2015). Forecasting the path of a laterally propagating dike. *Journal of Geophysical Research: Solid Earth*, *120*(12), 8774–8792.

Himematsu, Y., & Furuya, M. (2015). Aseismic strike–slip associated with the 2007 dike intrusion episode in Tanzania. *Tectonophysics*, *656*, 52–60.

Hjartardóttir, Á. R., Einarsson, P., Gudmundsson, M. T., & Högnadóttir, T. (2015). Fracture movements and graben subsidence during the 2014 Bárðarbunga dike intrusion in Iceland. *Journal of Volcanology and Geothermal Research*, *310*, 242–252.

Hooper, A., Zebker, H., Segall, P., & Kampes, B. (2004). A new method for measuring deformation on volcanoes and other natural terrains using InSAR persistent scatterers. *Geophysical Research Letters*, *31*(23), 1–5.

Ikeda, M., Toda, S., Kobayashi, S., Ohno, Y., Nishizaka, N., & Ohno, I. (2009). Tectonic model and fault segmentation of the Median Tectonic Line active fault system on Shikoku, Japan. *Tectonics*, *28*(5), 1–22.

Iken, A., & Bindschadler, R. A. (1986). Combined measurements of subglacial water pressure and surface velocity of Findelengletscher, Switzerland: conclusions about drainage system and sliding mechanism. *Journal of Glaciology*, *32*(110), 101–119.

Intrieri, E., Di Traglia, F., Del Ventisette, C., Gigli, G., Mugnai, F., Luzi, G., & Casagli, N. (2013). Flank instability of Stromboli volcano (Aeolian Islands, Southern Italy): Integration of GB-InSAR and

geomorphological observations. *Geomorphology*, *201*(October 2012), 60–69.

Jonsson, S., Zebker, H., Segall, P., & Amelung, F. (2002). Fault Slip Distribution of the 1999 Mw7.1 Hector Mine, California, Earthquake, Estimated from Satellite Radar and GPS Measurements. *Bulletin of the Seismological Society of America*, *92*, 1377–1389.

Jonsson, S., Segall, P., Pedersen, R., & Björnsson, G. (2003). Post-earthquake ground movements correlated to pore-pressure transients. *Nature*, *424*, 179–183.

Julian, B. R., Miller, A. D., & Foulger, G. R. (1998). Non-double-couple earthquakes 1. Theory. *Reviews of Geophysics*.

Jung, H., Won, J., & Kim, S. (2009). An Improvement of the Performance of Multiple-Aperture SAR Interferometry (MAI). *IEEE Transactions on Geoscience and Remote Sensing*, *47*(8), 2859–2869.

Kato, A., Nakamura, K., & Hiyama, Y. (2016). The 2016 Kumamoto earthquake sequence. *Proceedings of the Japan Academy, Series B*, *92*(8), 358–371.

King, G. C. P., Stein, S., & Lin, J. (1994). Static Stress Changes and the Triggering of Earthquakes. *Bulletin of the Seismological Society of America*, *84*(3), 935–953.

Kinoshita, Y., Shimada, M., & Furuya, M. (2013). InSAR observation and numerical modeling of the water vapor signal during a heavy rain: A case study of the 2008 Seino event, central Japan. *Geophysical Research Letters*, *40*(17), 4740–4744.

Kobayashi, T., Takada, Y., Furuya, M., & Murakami, M. (2009). Locations and types of ruptures involved in the 2008 Sichuan earthquake inferred from SAR image matching. *Geophysical Research Letters*, *36*(7), 1–5.

Koptev, A., Calais, E., Burov, E., Leroy, S., & Gerya, T. (2015). Dual continental rift systems generated by plume–lithosphere interaction. *Nature Geoscience*, *8*, 1–5.

Kreemer, C., Holt, W. E., & Haines, a. J. (2003). An integrated global model of present-day plate motions and plate boundary deformation. *Geophysical Journal International*, *154*(1), 8–34.

Li, F. K., & Goldstein, R. M. (1990). Studies of Multibaseline Spaceborne Interferometric Synthetic Aperture Radars. *IEEE Transactions on Geoscience and Remote Sensing*, *28*(1), 88–97.

Li, Z. W., Xu, W. B., Feng, G. C., Hu, J., Wang, C. C., Ding, X. L., & Zhu, J. J. (2012). Correcting atmospheric effects on InSAR with MERIS water vapour data and elevation-dependent interpolation model. *Geophysical Journal International*, *189*(2), 898–910.

Lohman, R. B., & McGuire, J. J. (2007). Earthquake swarms driven by aseismic creep in the Salton Trough, California. *Journal of Geophysical Research*, *112*(B4), B04405.

Maeda, J., & Heki, K. (2014). Two-dimensional observations of midlatitude sporadic e irregularities with a dense GPS array in Japan. *Radio Science*, *49*(1), 28–35.

Maeda, J., Suzuki, T., Furuya, M., & Heki, K. (2016). Imaging the midlatitude sporadic E plasma patches with a coordinated observation of spaceborne InSAR and GPS total electron content. *Geophysical Research Letters*, *43*(4), 1419–1425.

Maerten, F., Resor, P., Pollard, D., & Maerten, L. (2005). Inverting for Slip on Three-Dimensional Fault Surfaces Using Angular Dislocations. *Bulletin of the Seismological Society of America*, *95*(5), 1654–1665.

Magnússon, E., Björnsson, H., Dall, J., & Pálsson, F. (2005). Volume changes of Vatnajökull ice cap, Iceland, due to surface mass balance, ice flow, and subglacial melting at geothermal areas. *Geophysical Research Letters*, *32*(5), 1–4.

Magnússon, E., Rott, H., Björnsson, H., & Pálsson, F. (2007). The impact of jökulhlaups on basal sliding observed by SAR interferometry on Vatnajökull, Iceland. *Journal of Glaciology*, *53*(181), 232–240.

Mandl, G. (1987). Tectonic deformation by rotating parallel faults: the "bookshelf" mechanism. *Tectonophysics*, *141*, 277–316.

Massonnet, D., & Feigl, K. L. (1998). Radar interferometry and its application to changes in the Earth's surface. *Reviews of Geophysics*, *36*, 441–500.

Matsumoto Y. (1979). Some problems on volcanic activities and depression structures in Kyushu, Japan. The Memoir of the Geological Society of Japan, 16, 127-139 (in Japanese with English abstruct)

McKenzie, D., Davies, D., & Molnar, P. (1970). Plate tectonics of the Red Sea and East Africa. *Nature*, *226*, 243–248.

Meade, B. J. (2007). Algorithms for the calculation of exact displacements, strains, and stresses for triangular dislocation elements in a uniform elastic half space. *Computers & Geosciences*, *33*(8), 1064–1075.

Meyer, F. J. (2011). Performance requirements for ionospheric correction of low-frequency SAR data. *IEEE Transactions on Geoscience and Remote Sensing*, *49*(10 PART 1), 3694–3702.

Michel, R., Avouac, J. P., & Taboury, J. (1999). Measuring ground displacement from SAR amplitude images: application to the Landers earthquake. *Geophysical Research Letters*, *26*(7), 875–878.

Moore, J. D. P., Yu, H., Tang, C. H., Wang, T., Barbot, S., Peng, D., et al. (2017). Imaging the distribution of transient viscosity after the 2016 Mw7.1 Kumamoto earthquake. *Science*, *356*(6334), 163–167.

Moustafa, A. (2002). Controls on the geometry of transfer zones in the Suez rift and northwest Red Sea: Implications for the structural geometry of rift systems. *AAPG Bulletin*, *6*(6), 979–1002.

Nishimura, S., & Hashimoto, M. (2006). A model with rigid rotations and slip deficits for the GPS-derived velocity field in Southwest Japan. *Tectonophysics*, *421*(3–4), 187–207.

Nobile, A., Pagli, C., Keir, D., Wright, T. J., Ayele, A., Ruch, J., & Acocella, V. (2012). Dike-fault interaction during the 2004 Dallol intrusion at the northern edge of the Erta Ale Ridge (Afar, Ethiopia). *Geophysical Research Letters*, *39*(19).

Okada, Y. (1985). Surface deformation due to shear and tensile faults in a half-space. *Bulletin of the Seismological Society of America*, *75*(4), 1135–1154.

Okada, Y. (1992). Internal deformation due to shear and tensile faults in a half-space. *Bulletin of the*

Seismological Society of America, *82*(2), 1018–1040.

Okubo, Y., Shibuya, A. (1993). Thermal and crustal structure of the Aso volcano and surrounding regions constrained by gravity and magnetic data, Japan. Journal of Volcanology and Geothermal Research, 55, 337-350.

Ozawa, S., Murakami, M., Fujiwara, S., & Tobita, M. (1997). Synthetic aperture radar interferogram of the 1995 Kobe earthquake and its geodetic inversion. *Geophysical Research Letters*, *24*(18), 2327–2330.

Pagli, C., Wang, H., Wright, T. J., Calais, E., & Lewi, E. (2014). Current plate boundary deformation of the Afar rift from a 3D velocity field inversion of InSAR and GPS. *Journal of Geophysical Research: Solid Earth*.

Paquet, F., Dauteuil, O., Hallot, E., & Moreau, F. (2007). Tectonics and magma dynamics coupling in a dyke swarm of Iceland. *Journal of Structural Geology*, *29*(9), 1477–1493.

Parks, M. M., Heimisson, E. R., Sigmundsson, F., Hooper, A., Vogfjörd, K. S., Árnadóttir, T., et al. (2017). Evolution of deformation and stress changes during the caldera collapse and dyking at Bárdarbunga, 2014–2015: Implication for triggering of seismicity at nearby Tungnafellsjökull volcano. *Earth and Planetary Science Letters*, *462*, 212–223.

Pedersen, G. B. M., Höskuldsson, A., Dürig, T., Thordarson, T., Jónsdóttir, I., Riishuus, M. S., et al. (2017). Lava field evolution and emplacement dynamics of the 2014–2015 basaltic fissure eruption at Holuhraun, Iceland. *Journal of Volcanology and Geothermal Research*, *340*, 155–169.

Pollitz, F. F., Kobayashi, T., Yarai, H., Shibazaki, B., & Matsumoto, T. (2017). Viscoelastic lower crust and mantle relaxation following the 14–16 April 2016 Kumamoto, Japan, earthquake sequence. *Geophysical Research Letters*, *44*(17), 8795–8803.

Reynolds, H. I., Gudmundsson, M. T., Högnadóttir, T., Magnússon, E., & Pálsson, F. (2017). Subglacial volcanic activity above a lateral dyke path during the 2014–2015 Bárdarbunga-Holuhraun rifting episode, Iceland. *Bulletin of Volcanology*, *79*(6), 1–13.

Riel, B., Milillo, P., Simons, M., Lundgren, P., Kanamori, H., & Samsonov, S. (2015). The collapse of Bárarbunga caldera, Iceland. *Geophysical Journal International*, *202*, 446–453.

Rignot, E., Echelmeyer, K., & Krabill, W. B. (2001). Penetration depth of interferometric synthetic aperture radar signals in snow and ice. *Geophysical Research Letters*, *28*(18), 3501–3504.

Rosen, P. A., Hensley, S., & Chen, C. (2010). Measurement and mitigation of the ionosphere in L-band Interferometric SAR data. *IEEE National Radar Conference - Proceedings*, 1459–1463.

Rossi, C., Minet, C., Fritz, T., Eineder, M., & Bamler, R. (2016). Temporal monitoring of subglacial volcanoes with TanDEM-X - Application to the 2014-2015 eruption within the Bárdarbunga volcanic system, Iceland. *Remote Sensing of Environment*, *181*, 186–197. https://doi.org/10.1016/j.rse.2016.04.003

Ruch, J., Wang, T., Xu, W., Hensch, M., & Jónsson, S. (2016). Oblique rift opening revealed by

reoccurring magma injection in central Iceland. *Nature Communications*, *7*, 12352.

Ruina, A. (1983). Slip instability and state variable friction laws. *Journal of Geophysical Research*, *88*(B12), 10359.

Sandwell, D. T., Myer, D., Mellors, R., Shimada, M., Brooks, B., & Foster, J. (2008). Accuracy and resolution of ALOS interferometry: Vector deformation maps of the father's day intrusion at Kilauea. *IEEE Transactions on Geoscience and Remote Sensing*, *46*(11), 3524–3534.

Sansosti, E., Berardino, P., Manunta, M., Serafino, F., & Fornaro, G. (2006). Geometrical SAR image registration. *IEEE Transactions on Geoscience and Remote Sensing*, *44*(10), 2861–2870.

Saria, E., Calais, E., Stamps, D. S., Delvaux, D., & Hartnady, C. J. H. (2014). Present-day kinematics of the East African Rift. *Journal of Geophysical Research: Solid Earth*, 3584–3600.

Schmidt, D. A., & Bürgmann, R. (2003). Time-dependent land uplift and subsidence in the Santa Clara valley, California, from a large interferometric synthetic aperture radar data set. *Journal of Geophysical Research: Solid Earth*, *108*(B9), 1–13.

Scholz, C. H., & Contreras, J. C. (1998). Mechanics of continental rift architecture. *Geology*, *26*(11), 967–970.

Serafino, F. (2006). SAR Image Coregistration Based on Isolated Point Scatterers. *IEEE Geoscience and Remote Sensing Letters*, *3*(3), 354–358.

Sigmundsson, F., Hooper, A., Hreinsdóttir, S., Vogfjörd, K. S., Ófeigsson, B. G., Heimisson, E. R., et al. (2015). Segmented lateral dyke growth in a rifting event at Bárðarbunga volcanic system, Iceland. *Nature*, *517*.

Simons, M., Fialko, Y., & Rivera, L. (2002). Coseismic deformation from the 1999 Mw 7.1 Hector Mine, California, earthquake as inferred from InSAR and GPS observations. *Bulletin of the Seismological Society of America*, *92*(4), 1390–1402.

Sleep, N. H. (1997). Lateral flow and ponding of starting plume material. *Journal of Geophysical Research-Solid Earth*, *102*(B5), 10001–10012.

Spaans, K., & Hooper, A. (2018). Insights Into the Stress Field Around Bár ðarbunga Volcano From the 2014/2015 Holuhraun Rifting Event. *Journal of Geophysical Research: Solid Earth*.

Stamps, D. S., Calais, E., Saria, E., Hartnady, C., Nocquet, J.-M., Ebinger, C. J., & Fernandes, R. M. (2008). A kinematic model for the East African Rift. *Geophysical Research Letters*, *35*(5), L05304.

Strozzi, T., Luckman, A., Murray, T., Wegmüller, U., & Werner, C. L. (2002). Glacier motion estimation using SAR offset-tracking procedures - White Rose Research Online. *IEEE Transactions on Geoscience and Remote Sensing*, *40*(11), 2384–2391.

Tada, T. (1984). Spreading of the Okinawa trough and its relation to the crustal deformation in Kyushu. Jishin, 37, 407-415. (in Japanese with English abstract)

Tada, T. (1985). Spreading of the Okinawa trough and its relation to the crustal deformation in Kyushu (2). Jishin, 38, 1-15. (in Japanese with English abstract)

Tada, T. (1993). Crustal deformation in central Kyushu, Japan and its tectonic implication—rifting and spreading of Beppu Shimabara Graben. The Memoir of the Geological Society of Japan, 41, 1-12. (in Japanese with English abstract)

Takada, Y., & Fukushima, Y. (2013). Volcanic subsidence triggered by the 2011 Tohoku earthquake in Japan. *Nature Geoscience*, *6*(8), 637–641.

Takada, Y., & Furuya, M. (2010). Aseismic slip during the 1996 earthquake swarm in and around the Onikobe geothermal area, NE Japan. *Earth and Planetary Science Letters*, *290*(3–4), 302–310.

Takada, Y., Kobayashi, T., Furuya, M., & Murakami, M. (2009). Coseismic displacement due to the 2008 Iwate-Miyagi Nairiku earthquake detected by ALOS / PALSAR : preliminary results. *Natural History*, 9–12.

Tapponnier, P., & Courtillot, V. (1990). Bookshelf faulting and horizontal block ratations between overlapping rifts in southern Afar. *Geophysical Research Letters*, *17*(1), 1–4.

Tarchi, D., Rudolf, H., Luzi, G., Chiarantini, L., Coppo, P., & Sieber, A. J. (1999). SAR interferometry for structural changes detection: a demonstration test on a dam. *IEEE 1999 International Geoscience and Remote Sensing Symposium. IGARSS'99 (Cat. No.99CH36293)*, *3*, 1522–1524.

Tesfaye, S., Rowan, M. G., Mueller, K., Trudgill, B. D., & Harding, D. J. (2008). Relay and accommodation zones in the Dobe and Hanle grabens, central Afar, Ethiopia and Djibouti. *Journal of the Geological Society*, *165*(2), 535–547.

Tobita, M., Murakami, M., Nakagawa, H., Yarai, H., Fujiwara, S., & Rosen, P. A. (2001). 3-D surface deformation of the 2000 Usu Eruption measured by matching of SAR images. *Geophysical Research Letters*, *28*(22), 4291–4294.

Toda, S., & Stein, R. (2002). Response of the San Andreas fault to the 1983 Coalinga-Nuñez earthquakes: An application of interaction-based probabilities for Parkfield. *Journal of Geophysical Research: Solid Earth*, *107*.

Toda, S., Stein, R. S., & Sagiya, T. (2002). Evidence from the AD 2000 Izu islands earthquake swarm that stressing rate governs seismicity. *Nature*, *419*(6902), 58–61.

Tsai, V. C., Rice, J. R., & Fahnestock, M. (2008). Possible mechanisms for glacial earthquakes. *Journal of Geophysical Research: Earth Surface*, *113*(3), 1–17.

Tsugawa, T., Saito, A., & Otsuka, Y. (2004). A statistical study of large-scale traveling ionospheric disturbances using the GPS network in Japan. *Journal of Geophysical Research: Space Physics*, *109*(A6), 1–11.

Urbani, S., Acocella, V., Rivalta, E., & Corbi, F. (2017). Propagation and arrest of dikes under topography: Models applied to the 2014 Bardarbunga (Iceland) rifting event. *Geophysical Research Letters*, *44*(13), 6692–6701.

Vidale, J. E., & Shearer, P. M. (2006). A survey of 71 earthquake bursts across southern California: Exploring the role of pore fluid pressure fluctuations and aseismic slip as drivers. *Journal of*

Geophysical Research: Solid Earth, *111*(5), 1–12.

Watanabe, K., Momikura, Y., Tsuruta, K. (1979). Active faults and parasitic eruption centers on the west flank of Aso caldera, Japan. Quaternary Research, 18, 89-101. (in Japanese with English abstract)

Wegmüller, U., & Werner, C. L. (1997). Gamma SAR processor and interferometry software. *Proc. of the 3rd ERS Symposium, European Space Agency Special Publication*, (ESA SP-414), 1687–1692.

Wicks, C., Thelen, W., Weaver, C., Gomberg, J., Rohay, A., & Bodin, P. (2011). InSAR observations of aseismic slip associated with an earthquake swarm in the Columbia River flood basalts. *Journal of Geophysical Research*, *116*, B12304.

Wright, T. J., Lu, Z., & Wicks, C. (2003). Source model for the Mw 6.7, 23 October 2002, Nenana Mountain Earthquake (Alaska) from InSAR. *Geophysical Research Letters*, *30*(18), 30–33.

Wright, T. J., Parsons, B. E., & Lu, Z. (2004). Toward mapping surface deformation in three dimensions using InSAR. *Geophysical Research Letters*, *31*(1). https://doi.org/10.1029/2003GL018827

Wright, T. J., Ebinger, C., Biggs, J., Ayele, A., Yirgu, G., Keir, D., & Stork, A. (2006). Magma-maintained rift segmentation at continental rupture in the 2005 Afar dyking episode. *Nature*, *442*(7100), 291–294.

Wright, T. J., Sigmundsson, F., Pagli, C., Belachew, M., Hamling, I. J., Brandsdóttir, B., et al. (2012). Geophysical constraints on the dynamics of spreading centres from rifting episodes on land. *Nature Geoscience*, *5*(4), 242–250.

Xu, S., Ángel Francisco, N.-S., Susana, A. A.-Á., & Luis, M. C.-M. (2011). Structural analysis of a relay ramp in the Querétaro graben, central Mexico: Implications for relay ramp development. *Revista Mexicana de Ciencias Geológicas*, *28*(2), 275–289.

De Zan, F. (2014). Accuracy of incoherent speckle tracking for circular gaussian signals. *IEEE Geoscience and Remote Sensing Letters*, *11*(1), 264–267.

Zebker, H. A., & Villasenor, J. (1992). Decorrelation in interferometric radar echoes. *IEEE Transactions on Geoscience and Remote Sensing*, *30*(5), 950–959. https://doi.org/10.1109/36.175330

Zebker, H. A., Rosen, P., Hensley, S., & Mouginis-Mark, P. J. (1996). Analysis of active lava flows on Kilauea volcano, Hawaii, using SIR-C radar correlation measurements. *Geology*, *24*(6), 495–498.

Zebker, H. A., Rosen, P. A., & Hensley, S. (1997). Atmospheric effects in interferometric synthetic aperture radar surface deformation and topographic maps. *Journal of Geophysical Research: Solid Earth*, *102*(B4), 7547–7563.

Appendix A. SAR Dataset in Chapter 5

Satellite	Track	Date	Purpose	Spatial resolution [m (Range, Az.)]
COSMO-SkyMed	2631 (A)	28 Jun. 2014	a, b	1.0, 2.3
		30 Jul. 2014	a, b	
		12 Sep. 2014	a, b	
		18 Oct. 2014	b	
		22 Oct. 2014	b	
	2761(A)	11 Aug. 2014	c	1.0, 2.3
		27 Aug. 2014	c	
		28 Aug. 2014	c	
		31 Aug. 2014	c	
		12 Sep. 2014	c	
		13 Sep. 2014	c	
		16 Sep. 2014	c	
		2 Oct. 2014	c	
		6 Oct. 2014	c	
		14 Oct. 2014	c	
		16 Oct. 2014	c	
		18 Oct. 2014	c	
	2632 (D)	26 Jun. 2014	b	1.0, 2.1
		28 Jul. 2014	a, b, d	
		13 Aug. 2014	a, b	
		12 Sep. 2014	a, b	
		23 Sep. 2014	a, b	
		30 Sep. 2014	b	
		6 Mar. 2015	d	
	2762(D)	10 Aug. 2014	c	1.0, 2.1
		26 Aug. 2014	c	
		30 Aug. 2014	c	
		15 Sep. 2014	c	
		5 Oct. 2014	c	

		13 Oct. 2014	c	
		14 Oct. 2014	c	
		17 Oct. 2014	c	
		21 Oct. 2014	c	
TerraSAR-X	147 (A)	26 Jul. 2012	a, b	1.0, 1.7
		4 Sep. 2014	a, b	
		20 Nov. 2014	a, b	
RADARSAT-2	81 (A)	8 Jul. 2014	a	4.7, 5.2
		1 Aug. 2014	a	
		18 Sep. 2014	a	
	181 (A)	21 Jun. 2014	a	4.7, 5.2
		8 Aug. 2014	a	
		1 Sep. 2014	a	
Sentinel-1A	147 (A)	7 Jan. 2015	b	2.3, 13.9
		31 Jan. 2015	b	
		12 Feb. 2015	b	
		20 Mar. 2015	b	
		1 Apr. 2015	b	
		25 Apr. 2015	b	
		7 May 2015	b	
		19 May 2015	b	
		12 Jun. 2015	b	
		24 Jun. 2015	b	
		6 Jul. 2015	b	
		18 Jul. 2015	b	
		30 Jul. 2015	b	
		23 Aug. 2015	b	
		16 Sep. 2015	b	
		28 Sep. 2015	b	
		10 Oct. 2015	b	
		22 Oct. 2015	b	
		3 Nov. 2015	b	

	27 Nov. 2015	b	
	9 Dec. 2015	b	
	21 Dec. 2015	b	
	14 Jan. 2016	b	
	7 Feb. 2016	b	
	2 Mar. 2016	b	
	26 Mar. 2016	b	
	19 Apr. 2016	b	
	1 May 2016	b	
	6 Jun. 2016	b	
	30 Jun. 2016	b	
	12 Jul. 2016	b	
	24 Jul. 2016	b	
	17 Aug. 2016	b	
	5 Aug. 2016	b	
	17 Aug. 2016	b	
	29 Aug. 2016	b	
	4 Oct. 2016	b	
	28 Oct. 2016	b	
	21 Nov. 2016	b	
	15 Dec. 2016	b	
	8 Jan. 2017	b	
	1 Feb. 2017	b	
111(D)	18 Nov. 2014	b	2.3, 13.9
	30 Nov. 2014	b	
	24 Dec. 2014	b	
	5 Jan. 2015	b	
	17 Jan. 2015	b	
	10 Feb. 2015	b	
	22 Feb. 2015	b	
	6 Mar. 2015	b	
	18 Mar. 2015	b	
	30 Mar. 2015	b	
	11 Apr. 2015	b	
	23 Apr. 2015	b	

		5 May 2015	b	
		17 May 2015	b	
		29 May 2015	b	
		10 Jun. 2015	b	
		22 Jun. 2015	b	
		4 Jul. 2015	b	
		16 Jul. 2015	b	
		9 Aug. 2015	b	
		21 Aug. 2015	b	
		14 Sep. 2015	b	
		26 Sep. 2015	b	
		8 Oct. 2015	b	
		1 Nov. 2015	b	
		13 Nov. 2015	b	
		31 Dec. 2015	b	
		24 Jan. 2016	b	
		5 Feb. 2016	b	
		29 Feb. 2016	b	
		24 Mar. 2016	b	
		5 Apr. 2016	b	
		23 May 2016	b	
		4 Jun. 2016	b	
		28 Jun. 2016	b	
		22 Jul. 2016	b	
		3 Aug. 2016	b	
		27 Aug. 2016	b	
		20 Sep. 2016	b	
		2 Oct. 2016	b	
		26 Oct. 2016	b	
		1 Dec. 2016	b	
		13 Dec. 2016	b	
		25 Dec. 2016	b	
		18 Jan. 2017	b	
PALSAR-2	4_1290	28 Aug. 2014	a	4.3, 3.2
		11 Sep. 2014	a	

2_1300	24 Nov. 2014	e	4.3, 3.2
	2 Feb. 2015	e	
	6 Jul. 2015	e	
	14 Sep. 2015	e	
	23 Nov. 2015	e	
	1 Feb. 2016	e	
	4 Jul. 2016	e	
	21 Nov. 2016	e	
	3 Jul. 2017	e	
	11 Sep. 2017	e	
113_2300	8 Apr. 2015	e	19.0, 25.9
	29 Jul. 2015	e	
	2 Dec. 2015	e	
	24 Feb. 2016	e	
	18 May 2016	e	
	29 Jun. 2016	e	
	13 Jul. 2016	e	
	21 Sep. 2016	e	
	11 Jan. 2017	e	
	17 May 2017	e	
	23 Aug. 2017	e	

[a] Name of SAR satellite

[b] Identification of track number. A: Ascending flight from SSE to NNW, D: Descending flight from NNW to SSE

[c] Date of data observation.

[d] Purpose of dataset. a) Crustal and icecap surface movement, b) Time-series of icecap surface change, c) Icecap deformation in Figures 5-14 and 5-15 and d) Tracing outline of lava field

[e] Spatial resolution of the dataset